



# Récupérateur d'énergie pour les systèmes TPMS : modélisation et validation expérimentale

Emine Zaouali

## ► To cite this version:

Emine Zaouali. Récupérateur d'énergie pour les systèmes TPMS : modélisation et validation expérimentale. Mechanical engineering [physics.class-ph]. Université Bourgogne Franche-Comté, 2018. English. NNT : 2018UBFCD072 . tel-03439261

HAL Id: tel-03439261

<https://tel.archives-ouvertes.fr/tel-03439261>

Submitted on 22 Nov 2021

**HAL** is a multi-disciplinary open access archive for the deposit and dissemination of scientific research documents, whether they are published or not. The documents may come from teaching and research institutions in France or abroad, or from public or private research centers.

L'archive ouverte pluridisciplinaire **HAL**, est destinée au dépôt et à la diffusion de documents scientifiques de niveau recherche, publiés ou non, émanant des établissements d'enseignement et de recherche français ou étrangers, des laboratoires publics ou privés.

# SPIM

## Thèse de Doctorat



école doctorale sciences pour l'ingénieur et microtechniques  
UNIVERSITÉ DE FRANCHE-COMTÉ

# Kinetic Energy Harvesters for TPMS Applications

## Design, Modeling and Experimental Validation

■ EMINE ZAOUALI



•UFC

école doctorale sciences pour l'ingénieur et microtechniques  
UNIVERSITÉ DE FRANCHE-COMTÉ

*Thèse de doctorat de l'Université de Bourgogne Franche-Comté*

*par* Emine ZAOUALI

discipline: Sciences pour l'ingénieur

# **Kinetic Energy Harvesters for TPMS Applications Design, Modeling and Experimental Validation**

# Récupérateur d’Energie pour les Systèmes TPMS : Conception, Modélisation et Validation Expérimentale

soutenue le 18 décembre 2018 à Besançon devant le jury composé de:

<b>Reporters</b>	Sergio BELLIZZI Mohamed ICHCHOUE	Directeur de Recherche, CNRS, LMA, Marseille, France Professeur des Universités, ECL, LTDS, Lyon, France
<b>Jury President</b>	Claude-Henri LAMARQUE	Directeur de Recherche, ENTPE, LTDS, Lyon, France
<b>Examiner</b>	Fehmi NAJAR	Professeur, EPT, LASMAP, La Marsa, Tunisie
<b>Supervisor</b>	Emmanuel FOLTETE	Professeur des Universités, UBFC, Besançon, France
<b>Co-Supervisor</b>	Najib KACEM	Maître de Conférences, UBFC, Besançon, France

# SPIN

# Thèse de Doctorat



école doctorale sciences pour l'ingénieur et microtechniques  
UNIVERSITÉ DE FRANCHE-COMTÉ

*Thesis Presented by*

Emine ZAOUALI

Thesis submitted for the degree of Doctor  
of the University of Bourgogne Franche-Comté (UBFC)

## Speciality: Engineering Sciences

# Kinetic Energy Harvesters for TPMS Applications Design, Modeling and Experimental Validation

Thesis defended on 18<sup>th</sup> December 2018 in front of the jury composed of

<b>Reporters</b>	Sergio BELLIZZI Mohamed ICHCHOU	Directeur de Recherche, CNRS, LMA, Marseille, France Professeur des Universités, ECL, LTDS, Lyon, France
<b>Jury President</b>	Claude-Henri LAMARQUE	Directeur de Recherche, ENTPE, LTDS, Lyon, France
<b>Examiner</b>	Fehmi NAJAR	Professeur, EPT, LASMAP, La Marsa, Tunisie
<b>Supervisor</b>	Emmanuel FOLTETE	Professeur des Universités, UBFC, Besançon, France
<b>Co-Supervisor</b>	Najib KACEM	Maître de Conférences, UBFC, Besançon, France

## DEDICATION

*To my family ...*



# CONTENTS

<b>Abstract</b>	<b>9</b>
<b>Résumé</b>	<b>11</b>
<b>Introduction</b>	<b>13</b>
<b>1 State of the Art</b>	<b>17</b>
1.1 Tire Pressure Monitoring System . . . . .	17
1.1.1 Measurement approaches in TPMS . . . . .	18
1.1.2 TPMS Legislative Framework . . . . .	20
1.1.3 Limits & Possible improvements of TPMS . . . . .	20
1.2 Energy Harvesting Technology . . . . .	21
1.2.1 Wireless sensor networks . . . . .	22
1.2.2 Transduction mechanism for kinetic energy harvesters . . . . .	23
1.3 Energy harvesting in TPMS . . . . .	25
1.3.1 Energy harvester fixed to the tire . . . . .	25
1.3.2 EH Fixed on the Rim . . . . .	29
1.4 Energy harvesting in rotating systems . . . . .	33
1.4.1 EH for rotating shafts . . . . .	33
1.4.2 Pendulum in energy harvesting devices . . . . .	35
1.5 Pendulum Theory . . . . .	37
1.5.1 Simple Pendulum . . . . .	37
1.5.2 Double Pendulum . . . . .	40
1.5.3 Rotating Pendulums . . . . .	42
1.6 Methodology and general framework . . . . .	43
<b>2 On the Use of pendulum-based energy harvester for rotating wheels</b>	<b>45</b>
2.1 Introduction . . . . .	45

## CONTENTS

---

2.2	Different pendulum designs . . . . .	45
2.2.1	Simple pendulum design with parallel axis . . . . .	47
2.2.2	Double pendulum design with parallel axes . . . . .	49
2.2.3	Simple pendulum design with non-parallel axis . . . . .	50
2.2.4	Rott's pendulum with parallel axis . . . . .	51
2.3	Comparison of different designs in the time domain . . . . .	53
2.3.1	Time response of the simple pendulum with parallel axis . . . . .	53
2.3.2	Time response of the double pendulum with parallel axis . . . . .	56
2.3.3	Time response of the simple pendulum with non-parallel axis . . . . .	60
2.3.4	Time response of the Rott's pendulum with parallel axis . . . . .	64
2.4	Results discussion . . . . .	68
2.5	Conclusion . . . . .	68
<b>3</b>	<b>Experimental Setup and results</b>	<b>71</b>
3.1	Introduction . . . . .	71
3.2	Characterization of the Electromagnetic Generator . . . . .	71
3.2.1	Presentation of the Generator . . . . .	71
3.2.2	Characterization assembly . . . . .	73
3.2.3	Experimental Characterization Results . . . . .	76
3.3	Characterization of Pendulums . . . . .	79
3.3.1	Presentation of Pendulums . . . . .	79
3.3.2	Setup of the studied pendulums . . . . .	79
3.4	Test Bench . . . . .	84
3.5	Experimental Results and Validation . . . . .	86
3.5.1	Test at constant angular rotation of the rim . . . . .	87
3.5.2	Test under periodic variation of the angular rotation of the disk . . . . .	96
3.6	Conclusion . . . . .	100
<b>4</b>	<b>Nonlinear steady state behavior of the Rott's pendulum</b>	<b>103</b>
4.1	Problem Statement . . . . .	103
4.2	Equations of motion of the rotating Rott's pendulum . . . . .	105
4.3	Nonlinear solution using a perturbation analysis . . . . .	107
4.4	Principal parametric resonance of the second mode with 2:1 internal resonance . . . . .	110
4.4.1	Modulation equations . . . . .	110
4.4.2	Periodic solutions and their stability . . . . .	111

## CONTENTS

---

4.5 Principal parametric resonance of the first mode with 2:1 internal resonance	114
4.5.1 Modulation equations	114
4.5.2 Periodic solutions and their stability	115
4.6 Results and discussion	115
4.6.1 Influence of the rotation speed: Force response of the device	116
4.6.2 Frequency response of the device	120
<b>General Conclusion and Future Works</b>	<b>125</b>
<b>Appendices</b>	<b>128</b>
A Layouts of the Test Bench	131
Bibliographie	148
list of figures	153
list of tables	155

## CONTENTS

---

## ABSTRACT

Energy Harvesters (EH) became one of the most attractive technologies in science and engineering thanks to its significant role in saving energy. One famous application of this system is its use to power Tire Pressure Monitoring Systems (TPMS). Despite there is a huge quantity of kinetic energy in rotating car's wheels, the fact that rotations of the wheel induce a high level of centrifugal forces presents a major drawback that deprive the harvesting of this type of energy.

In this thesis, a kinetic energy harvester is designed, modeled and fabricated. Different designs of multi-pendulum system which are known to be easily unstable are modeled and put under experiment. The harvested energy is also compared between different designs for the steady-state and the transient responses.

Mainly, two new research challenges are present in this case of study comparing to existing studies. First, the fact that the pendulum is implemented into the car's wheel induce a rotative excitation which is composition of a horizontal and a vertical excitations at the same time. Second, as we look for maximizing the harvested energy, our interest is presented not only to steady-state response but also to transient response.

The proof of concept on the use of pendulum-based energy harvester rotating wheels is tackled, considering a simple concentrated mass designs to analyze the motion and the possibility to harvest energy from rotating wheels with variable speeds. The equations of motion of four designs considered in transient behavior, are presented and derived. The time response of the angular position and angular velocity were calculated for different damping coefficients and initial conditions. The RMS value of the angular velocity used to estimate the harvested energy depends on the initial conditions.

A test bench is also set up to reproduce the behavior of the pendulum mounted into a rotating disk. The solution for the steady-state behavior of three pendulum designs, generated at angular velocity for different rotation speeds, is experimentally tested. Three different regimes exist: oscillations around the vertical axis, aperiodic oscillations and oscillations around the radial axis. The aperiodic regime gives better output voltage for

## ABSTRACT

---

each pendulum. Then, a half-sine input function is used to record the transient output voltage generated for different initial positions of the disk for each pendulum.

An analytical analysis is proposed to analyze the steady-state response under constant rotation speeds, because it represents a non negligible part of the regime of motion of the wheels. The method of multiple scales is applied for the equations of motion governing the motion of the Rott's pendulum when small oscillations are assumed around the radial positions. For the two proposed sets of geometrical dimensions, parametric resonance of the first and second modes while two to one internal resonance is satisfied can be achieved. In both cases, the analytically derived resonance conditions, shows that large amplitude of motions can be achieved if a critical value of the rotation speed is reached. However, if the speed is further increase the amplitude is again highly reduced. In fact, the treated case is specific to the TPMS case because the rotation speed in this case is at the same time the frequency excitation force and the amplitude of the stabilizing force represented here by the centrifugal force.

**Keywords:** energy harvesting, tire pressure monitoring system (TPMS), Rott's pendulum, multiple scales, perturbation technique, nonlinear dynamic.

## RÉSUMÉ

Les systèmes de récolte d'énergie sont devenus l'une des technologies les plus attrayantes grâce à leurs rôles de plus en plus importants dans la sauvegarde de l'énergie et de l'environnement. Une application souhaitée de ces systèmes est leur utilisation pour alimenter les systèmes de surveillance de la pression des pneus (TPMS). En effet, une grande quantité d'énergie cinétique due à la rotation des roues de voitures peut être exploitée par les récupérateurs d'énergie. Néanmoins, les forces centrifuges induites présentent un inconvénient majeur qui limite la récupération d'énergie.

Dans cette thèse, un récupérateur d'énergie cinétique est conçu, modélisé et fabriqué. Différents designs de systèmes à pendules multiples, connus pour être facilement instables, sont modélisés et mis à l'essai. L'énergie récoltée est également comparée entre différentes conceptions pour les réponses stables et transitoires.

Principalement, deux nouveaux défis sont traités dans le cadre de cette thèse. Premièrement, le fait que le pendule soit lié à la roue induit une excitation rotative particulièrement complexe. Deuxièmement, lorsque nous cherchons à maximiser l'énergie récoltée, notre intérêt se porte non seulement sur la réponse en régime permanent, mais également sur la réponse transitoire.

Un banc d'essai est également installé pour reproduire le comportement du pendule monté sur un disque rotatif. La solution pour le comportement en régime permanent de trois conceptions de pendules, générées à une vitesse angulaire pour différentes vitesses de rotation, est testée expérimentalement. Trois régimes différents existent: oscillations autour de l'axe vertical, oscillations apériodiques et oscillations autour de l'axe radial. Le régime apériodique donne une meilleure quantité d'énergie pour chaque pendule. Ensuite, une fonction d'entrée demi-sinusoidale est utilisée pour enregistrer l'énergie en régime transitoire générée pour différentes positions initiales du disque pour chaque pendule.

Une analyse analytique est proposée pour analyser la réponse en régime permanent à des vitesses de rotation constantes, car elle représente une partie non négligeable du régime de mouvement des roues. La méthode des échelles multiples est appliquée aux

## RESUME

---

équations de mouvement pour le pendule de Rott. Ainsi les conditions de résonance sont retrouvée pour maximiser l'énergie générée par le récolteur en mode permanent.

**Mots clés:** Récolte d'énergie, TPMS, Pendule de Rott, Méthode des échelles multiples, Analyse expérimentale, dynamique non linéaire.

# INTRODUCTION

## BACKGROUND AND MOTIVATIONS

Saving energy is with no doubt, one of the most important interests of researchers in this century. Indeed, many types of energy are present in the environment, all over the world, but the most important issue stills to be *how to convert ambient energy into electrical power?* A question which is in the origin of all research areas known as *renewable energy* and *energy harvesting*. The first one depends on large-scale power generation, for example, solar or wind power, and is concerned with megawatts of power generation. While the energy harvesting typically refers to power in the order of milli to micro-watts.

Now-days, to monitor different systems, more and more complex and networked, sensors become omnipresent, powered generally by button-batteries. This conduct researches to look for developed energy harvesters that can scavenge energy from the surrounding environment. A famous application of such system is the energy harvester for Tire Pressure Monitoring Systems (TPMS). Different energy harvesters were designed acting as transducers from sources of energy, such as vibrations, pressure, tire deformation, gravity... using piezoelectric, electrostatic, or electromagnetic transducers.

Nevertheless, the kinetic energy, which is present with high level in rotating car's wheels, has been roughly investigated. The fact that rotations of the wheel induce a high level of centrifugal forces, acting as a uni-direction static force is a major drawback for this particular energy harvesting design.

In this thesis, we aim to design, model and fabricate a kinetic energy harvester that can be efficient even in the previously mentioned conditions. The idea is to model and put under experiment different designs of multi-pendulum system which are known to be easily unstable, then, to compare the harvested energy, between different designs for the steady-state and the transient responses.

Many research works are presents in the literature for different kind of pendulums. However, in our case of study the pendulum will be implemented into the car's wheel,

therefore it presents new research challenges. Indeed, the excitation in our case is a rotative excitation which can be considered as a composition of a horizontal and a vertical excitations at the same time. In the other hand, the interest that has been presented by researchers in the literature, was in the study of the steady-state response of excited pendulums. In our case, even the transient response could be an interesting track of study as long as the harvested energy is maximized.

## THESIS ORGANIZATION

The dissertation is organized as follows. In Chapter 1, we present a general overview of the energy harvesting technology and in particular its application for TPMS. The technology used to harvest energy from rotating wheel to feed the TPMS device depends on the way in which the energy harvester is mounted; on the rim or on the tire. The energy harvesting was also investigated in different rotating systems using different technologies such as simple pendulums in self-winding watches. The pendulum theories for simple, double and rotating pendulums is also presented in order to link with the general methodology and framework in this thesis work.

Chapter 2 tackle the proof of concept on the use of pendulum-based energy harvester rotating wheels. Considering a simple concentrated mass designs to analyze the motion and the possibility to harvest energy from rotating wheels with variable speeds. The number of degree of freedom to be considered in these designs can vary. However, except the first degree which is restricted to the rotation of the wheel, for convenience the second one should carry the transducer. We start by presenting and deriving equations of motion of four designs that are taken into consideration in the transient behavior : Simple pendulum with parallel axis, double pendulum with parallel axes, simple pendulum with non-parallel axis and Rott's pendulum. In the second part of this chapter we compare different designs in the time domain. Starting by calculating the time response and the RMS value of the angular velocity for each design.

Chapter 3 puts into experiment three pendulum designs: simple pendulum, double pendulum and Rott's pendulum. Starting by characterizing the electromagnetic generator in which the pendulums will be linked. As a first step, we derive the governing equation of the generator to get the torque developed at the generator's shaft and the generated power. Then we look at the optimum load resistance by measuring the higher power from generated voltage and current. Then, we will proceed to the setup and characterization of each pendulum. We use a test bench setup to reproduce the behavior of the pendulum

---

mounted into a rotating disk. Steady-state and transient behaviors will be tested and the output voltage will be measured at each case.

In Chapter 4, an analytical approach is proposed to analyze the behavior of a specific pendulum, namely the Rott's design linked to a rotating wheel, in the steady-state regime. The perturbation technique is used in order to clarify the contribution of the different geometrical and physical parameters on the steady-state response of the Rott's pendulum under constant rotation speed.

The thesis is terminated by a general conclusion and an insight for future works.

## RESUME

---

# 1

## STATE OF THE ART

### 1.1 TIRE PRESSURE MONITORING SYSTEM

Tire Pressure Monitoring System (TPMS) refers to a device that monitors the internal pressure of tires for wheeled vehicles, and offers this information to the driver instantaneously in the dashboard of the vehicle [1]. Since the wheels are rotating with respect to the body of the vehicle, the TPMS is a wireless device that communicates the pressure information wirelessly after being measured inside the tire.

Using TPMS has several advantages:

- A reduction in fuel consumption : in fact for a percentage equivalent to 10% under-inflation on each tire of a given vehicle, results in a 1% reduction in fuel economy [2].
- Extend the life of tires: under-inflation is the main cause of tire wear failure. Indeed, under-inflation destroys the structure of the tire and increases the number of turns due to the decrease in its diameter. This reduces tire recycling possibilities such as retreading [3].
- Reduced downtime and maintenance: due to failures due to under-inflation, valuable downtime is required for maintenance. Indeed, tires naturally lose about 10% of their initial pressure.
- Improved safety: a well-inflated tire offers greater stability and maneuverability for the vehicle and allows better braking. In France, the road safety organization estimates that 9% of fatal road accidents are due to under-inflation. In Germany

DEKRA, a product safety organization, estimated that 41% of accidents with physical injuries are related to tire problems. In numbers, under-inflated tires causes 40,000 accidents, 33,000 injuries and over 650 deaths per year.

- Reduced Emissions: according to US Department of Transportation estimates, under-inflation of tires causes more than 26 million tonnes of carbon monoxide to be released into the atmosphere each year in the United States alone. EU reports indicate that an average under-inflation of 40 kPa produces a 2% increase in fuel consumption and a 25% reduction in tire life. The EU concludes that under-inflation of tires is now responsible for more than 20 million liters of fuel burnt unnecessarily, more than 2 million tonnes of CO<sub>2</sub> released into the atmosphere, and 200 million tires prematurely wasted in the world.

### 1.1.1 MEASUREMENT APPROACHES IN TPMS

The first TPMS is reported in a patent by McDonell [4]. The author of the patent used a complex wired system to monitor the pressure inside the tire. Several other systems were proposed in the following years either by particular inventor or tire manufacturing companies. Mainly, there are two types of technologies for TPMS: direct and indirect approaches.

Indirect approach operates in relation to the anti-lock braking system (ABS) [5]. In fact, measurement of small changes in wheel speed due to the reduction in its radius following a loss of pressure can be used to detect inflated tires. This approach can only detect variation of the pressure and cannot give an information about its specific value [6]. However, this technology does not require any additional installation on the wheel [7]. Other indirect approaches are based on analyzing the natural frequencies of the tire, which is strongly related to its internal pressure [5].

On the other hand, direct technology, measures directly the pressure on the wheel and can provides additional information, such as temperature and accelerations. However, it requires the installation of an energy source on each wheel such as batteries. The device is generally linked to the tire's valve, so that the pressure sensor can measure the differential pressure. An example of a direct approach TPMS is shown in Figure 1.1.

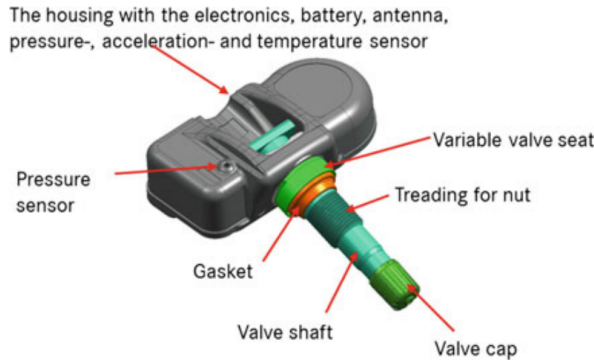


Figure 1.1: Tire Pressure Monitoring System using a direct approach measurement [5].

The direct approach is therefore the one which is more widespread for TPMS systems thanks to its measurement accuracy and its ability to adapt to future technologies of intelligent tires. However, energy requirement limit the lifespan of the device to only 7 to 10 years because of the use of battery [5]. Also, in case of battery replacement, the whole device should be replaced to avoid calibration problems. This fact highly increase maintenance costs. The TPMS device is composed of following main components that are mounted to the valve stem inside the tire:

- pressure sensor;
- analog-digital converter;
- microcontroller;
- system controller;
- oscillator;
- radio frequency transmitter;
- low frequency receiver, and
- voltage regulator (battery management).

There are two possible types of installations for direct approach TPMS device: internal or external. In the case of an internal installation the system is attached to the rim . For external installation it usually replaces the plug of the inflation valve.

### 1.1.2 TPMS LEGISLATIVE FRAMEWORK

In 2000, the US Congress passed the Transportation Recall Enhancement, Accountability and Documentation (or TREAD) Act, a federal law that intends to increase consumer safety through mandates assigned to the National Highway Traffic Safety Administration (NHTSA) [8]. TREAD requires that starting from year 2007, all vehicles sold in the United States (15 million each year) should include a TPMS.

In Europe, Regulation No 661/2009 of the European Parliament requires the adaptation of a TPMS module on all passenger vehicles over the period 2012-2014 [9]. The level of detection required by this law is 20%. In a second phase, after 2014, this level will be postponed to 15%.

### 1.1.3 LIMITS & POSSIBLE IMPROVEMENTS OF TPMS

All TPMS require an internal source of energy for their operation. Energy is mainly required for pressure and temperature measurements and for data transmission to the driver's display unit. This source is currently provided by batteries whose lifetime does not exceed 7 years [5], which requires additional maintenance. Even when using sampling measurement and transmission method, allowing tire pressure to be read every few seconds [6]. In addition, these systems allow data to be updated only when the vehicle exceeds 30 km/h.

Existing TPMS solutions present two major drawbacks today:

- The non-integration of the different technologies used: this presents a risk of high failure and a considerable additional cost at the manufacturing level. Integration also ensures the durability and reliability of the system.
- The presence of a battery for the operation of the system: it presents a not negligible safety risk in the event of simultaneously depletion and loss of pressure. In addition, car manufacturers recommend only between 7 and 10 years of battery life. It should be noted that the replacement of these millions of batteries presents a considerable danger to the environment, which is also not negligible.

Therefore, there is significant interest in replacing the battery in TPMS modules with an autonomous energy source such as energy harvesting systems. Figure 1.2 shows the TPMS block diagram which consists of a set of components: a system of measurement of pressure, temperature, motion ... which sends data to an analog-to-digital converter. Then a controller collects and processes them. Then, these data are transmitted by RF waves

to the control screen. The system can be powered by the energy harvesting and storage module. It allows the conversion of the mechanical energy, due to the vibration and/or rotation of the wheel, into electrical energy which will be temporarily stored to feed the other modules.

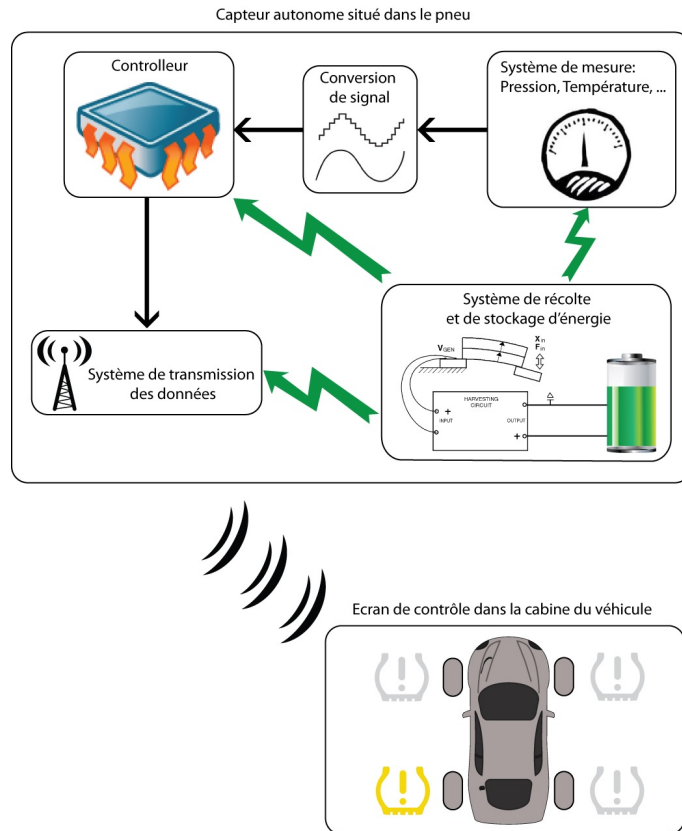


Figure 1.2: Schematic diagram of autonomous TPMS powered by an EH.

## 1.2 ENERGY HARVESTING TECHNOLOGY

Energy harvesting technology has been developed after the proliferation of "autonomous wireless electronic systems". Wireless sensor networks (WSN), a combination of wireless sensor nodes, with data processing and communication capabilities, are the classical example of such systems [10]. Recently, the use Internet of Things (IoT) [11] concept, which is also a WSN with internet communication capabilities, attracted the attentions of the IT (Information Technology) community because of its high integration potential. As the number of nodes tend to increase especially for IoT application, the integration of energy harvesters from the environment is an attractive solution to replace or increase life

time of batteries [12].

### 1.2.1 WIRELESS SENSOR NETWORKS

First WSN were used in military applications for battlefield surveillance [13]. After that they were used for monitoring and control in different fields [14] such as health care monitoring, industry (machine and structural health monitoring, data logging ...), environment and earth sensing (air pollution monitoring, natural disaster prevention...), pipeline monitoring ...

A WSN is composed of autonomous wireless sensors distributed in a specific area to monitor physical or environmental conditions, such as sound, pressure, temperature, etc., then they transfer their data through the network to a centralized processing station.

A sensor node has not only the task to collect data, but also to locally analyze, correlate, and fuse its own sensor data and data from other sensor nodes. Sensor nodes communicate not only with each other but also with a base station using their wireless radios, allowing them to disseminate their sensor data to remote processing, visualization, analysis, and storage systems. For example, Figure 1.3, presented by Dargie and Poellabauer [15], shows two sensor fields monitoring two different geographic regions and connecting to the Internet using their base stations.

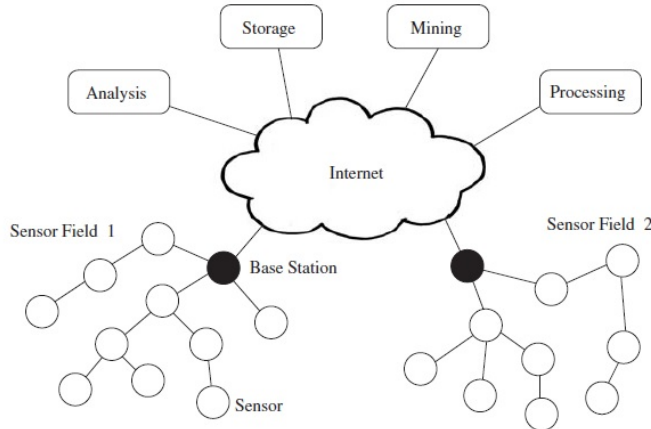


Figure 1.3: Wireless Sensor Networks [15]

Therefore, in a WSN, hundreds or even thousands of sensor nodes are connected between them to monitor a large physical environment. Each sensor node comprises a sensor, processing electronics, wireless communications, and power supply.

Internet of Things is foreseen to be a world-wide network of interconnected objects

uniquely addressable, based on standard communication protocols. In IoT any object, such as computers, sensors, RFID tags or mobile phones, is identified by a unique address, and will be able to dynamically join the Internet, collaborate and cooperate efficiently to achieve different tasks [16].

Since sensor nodes of a WSN are by definition wireless and cannot be plugged into a main supply, power has to be provided locally. Thus, typically such a local power supply is provided a battery. However, batteries contain a finite supply of energy and require periodic replacement or recharging. This may be fine in individual deployments but across a wireless network containing a multitude of nodes batteries are clearly not attractive. Furthermore, the need to replace batteries means the wireless system has to be accessible which may not be possible or may compromise performance. Finally, there are environmental concerns about disposing of batteries. Energy harvesting was developed, therefore, as a method for replacing or augmenting batteries.

In many cases, it is not possible to supply a sensor network, containing hundreds or thousands of sensors, by means of batteries. Indeed, the short life of batteries compared to the life of the sensor, requires a periodic replacement. Furthermore, the wireless system is not always accessible. Thus, the replacement of batteries may be not advisable, dangerous, too expensive or impossible. In addition, there are environmental concerns about disposing of batteries. In these situations, one possible solution is the use of an energy harvester, a device designed to collect energy from a source available in the environment, to provide the required electrical power during the lifetime of the wireless system, letting it free to be placed wherever. Energy Harvesting seems to be a very good alternative since energy is present everywhere in the environment. So we can scavenge energy from the nature (wind, water, sun) or from smart materials (piezoelectric, Electro active polymers... ) or even from active systems (kinetic, vibrations, thermal, electromagnetic radiation...)

### 1.2.2 TRANSDUCTION MECHANISM FOR KINETIC ENERGY HARVESTERS

Nowadays, energy harvesting is a research area by itself, composed of different fields, depending on the source of energy and the transduction technology.

In Table 1.1 we give a comparison of extracted power density using these technologies. Except for solar energy generation, which requires permanent outdoor solar panels, the approach based on harvesting ambient vibration energy exhibits the most promising technology for universal use. Thus, in this work, we will focus on one specific energy harvester which is the Kinetic energy harvester.

Table 1.1: Power density generation for available energy technologies [17].

Technology	Power Density ( $\mu\text{W}/\text{cm}^2$ )
Vibrations – electromagnetic	4.0
Vibrations – piezoelectric	500
Vibration – electrostatic	3.8
Thermoelectric (10°C gradient)	60
Solar energy (outdoor)	3700
Solar energy (indoor)	700
RF Signal	0.1

Kinetic energy harvester transduces movements or vibrations into electrical energy. The first kinetic energy harvester was developed by [18]. It is typically composed of a spring-mass system. When the generator vibrates, a relative movement is created between the mass and the housing. The sinusoidal displacement drives a transducer to generate electrical energy.

Many challenges face designers of kinetic energy harvesters. First, to choose the most suitable transducer that can give better power density and very low power electronics. Energy harvesting faces technological challenges for overcoming difficulties related to size dependency of the produced power. Furthermore, most of ambient vibration-energy harvesters are efficient only within a limited range of vibration frequencies. Depending on these characteristics, three basic vibration-to-electric energy conversion mechanisms are mainly utilized: electromagnetic, electrostatic and piezoelectric transductions.

**Piezoelectric Energy Harvesting** Energy harvesting using piezoelectric transduction relies on the vibration of structures. A piezoelectric material has the ability to convert mechanical strain to electrical polarization, and vice versa. Piezoelectric phenomena are found in crystal materials which do not have a symmetry center regarding the positive and negative charges. Therefore, creating an electrical polarization within the crystal material. Several configurations have been used in the literature with monomorph [19] and bimorph [20] configurations into cantilever beams. To increase the inertia of the oscillator and reduce its fundamental natural frequency, a tip mass is sometimes added.

**Electrostatic Energy Harvesting** Electrostatic energy harvesters are micro-machined devices including variable capacitance by moving one of the electrodes with respect to the other one, using mechanical vibration from the environment. The system converts

mechanical energy into electrical one by using two basic mechanisms: voltage-constrained and charge-constrained approaches. In both cases a suitable electric conditioning circuit should be addressed in addition to a voltage source that charges the variable capacitor at its lower position [21]. Also, electret based material could be used to eliminate the voltage or charge source [22]. The same concept was used by [23] to convert kinetic energy using a dielectric elastomer material. The material is disposed into membranes where the faces are covered by compliant electrodes. The small variation of the thickness is used as a variable capacitor [24]. Variable capacitor are particularly suitable for miniaturization especially using MEMS (MicroElectroMechanical Systems) technology.

**Electromagnetic Energy Harvesting** Electromagnetic Energy Harvesting depends on the Faraday's law of electromagnetic induction : when an electric conductor is moved through a magnetic field, a potential difference is induced between the ends of the conductor. The circuit consists of a coil of wire of multiple turns and the magnetic field is created by permanent magnets [25, 26]. These transducers generates high power densities, however they are difficult to miniaturize because of the presence of the coil.

## 1.3 ENERGY HARVESTING IN TPMS

In the literature, the fact that these systems are installed in the wheels, led the researchers to use different sources of motion and deformations to be converted into electrical energy. For example, tire deformations, variation of the radial acceleration due to wheel contact with the ground, vibrations due to unbalanced masses, pressure variations, rotation ... These different excitations define the way in which the energy harvester is mounted. Therefore, two kinds of mountings exists: to the tire or to the rim.

### 1.3.1 ENERGY HARVESTER FIXED TO THE TIRE

The contact of the tire with the ground generates displacements that are periodic due to the rotation of the wheel. In fact, the contact area can be represented as a plat surface that change locally the radius of the tire. Two effects can be extracted from this radius variation: (i) The local deformation of the tire at the contact surface, and (ii) The variation of the radial acceleration for a material point located at the tire, at the beginning and the end of the contact zone. In Figure 1.4, Bowen and Arafa [27] shows the variation of circumferential strain and radial acceleration in a tire rolling on a hard surface. Bowen

and Arafa [27] reported that a peak acceleration of 100g can be measured at 60km/h and that the corresponding deformation can reach  $4000\mu\varepsilon$ . Also Tornincasa et al. [28] showed that 180g can be measured for a tire with 60km/h speed, the time response of the radial acceleration for different speeds of the vehicle are shown in Figure 1.5.

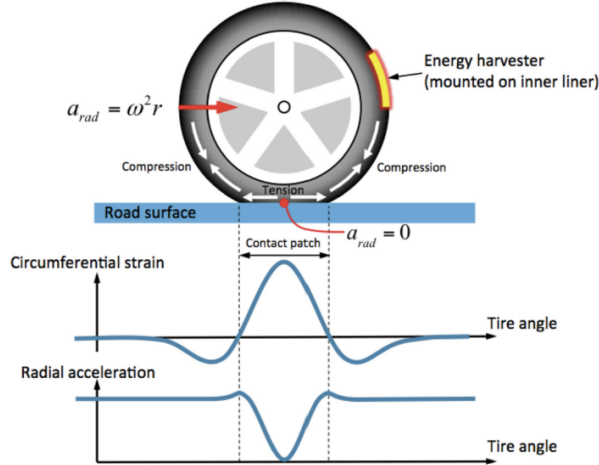


Figure 1.4: The qualitative variation of circumferential strain and radial acceleration in a typical tire rolling over a hard surface [27]

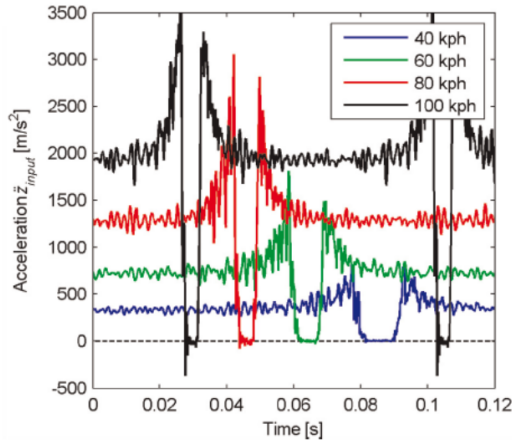


Figure 1.5: Typical radial acceleration profile at different speeds of a point in the inner tire liner [28].

**Concepts based on tire deformation** : The deformation of the tire can be of the bending or stretching type, both can be converted into electrical energy using active material such as piezoelectric patches that are directly attached to the tire [29]. Several solutions were proposed in the literature using this concept. In general the harvester is attached to the

internal side of the tire and deforms when the tire comes into contact with the ground. The idea have been the subject of several patents. For example, Mancosu et al. [30] proposed a device in form of a piezoelectric wire fixed into the circumferential internal side the tire (Figure 1.6). Adamson and O'brien [31] and Lee et al. [32] designed an energy harvester with a AFC patch, i.e. piezoelectric fiber material embedded into an epoxy matrix and using interdigitated electrodes as shown in Figure 1.7 for to the device proposed in [31]. The AFC patch is mounted on a support substrate that helps distribute mechanical strain to which the piezoelectric fibers are subjected in a substantially uniform way. The AFC structure is mounted within the tire structure such that electric charge is generated when the wheel assembly moves along a ground surface. Electrodes are coupled to a power conditioning module that rectifies the resultant electric current and stores it in an energy storage device, such as electrolytic capacitors [31].

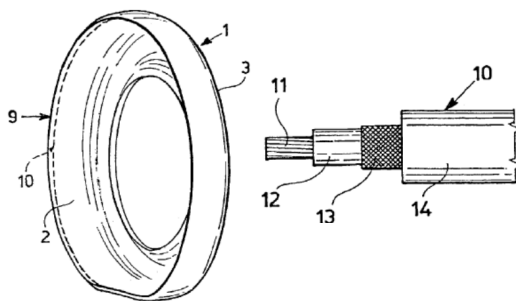


Figure 1.6: Energy Harvester as a piezoelectric wire fixed inside the tire [30].

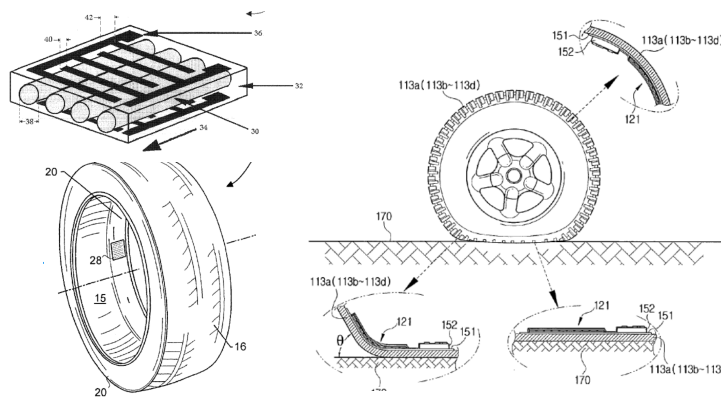


Figure 1.7: Piezo-composite patches EH [31].

Van den Ende et al. [33] used the same idea but with a PVDF material, they estimated that the polymer patch can generate  $30\mu\text{W}/\text{cm}^2$  at 50km/h. Also with a PVDF patch [34] showed that much higher energy can be extracted (around  $53\mu\text{W}/\text{cm}^2$ ) if the patch is

mounted on a ribbon bonded to the bead of the tire. In the same paper Makki and Pop-Iliev [34] used a piezoelectric PZT material patch that was directly bonded to the tire. A special high temperature adhesive was used to allow the patch to deform with the tire without damaging the PZT ceramic layer from high strain. Makki and Pop-Iliev [34] showed that  $936\mu\text{W}/\text{cm}^2$  of power density can be achieved. The PZT based design was shown to be the most efficient thanks to the high piezoelectric coupling coefficient of the PZT compared to PVDF. Since the deformation of the tire is directly proportional to the voltage generated by the piezoelectric patch, some researchers thought of using this information to monitor the tire conditions. The concept is known as *intelligent or smart tire* [35].

**Concepts based on the variation of the radial acceleration of the tire** : The variation of the radial acceleration of tire due to several causes can generate vibrations of the tire. These vibration can be harvested and converted into electrical energy. A large broadband frequencies are concerned with vibration, however they are centered around 100 Hz [36, 37].

In order to convert vibration into electrical energy, piezoelectric materials are also used here. However, an inertial mass attached to an elastic component should be added in order to activate the piezoelectric patch. A two-layer piezoelectric bender (bimorph) mounted as a cantilever beam is used by [38, 39, 40]. Others used a monomorph piezoelectric material as a cantilever beam and a mass attached to its free end [41]. Both designs were attached to the tire. In addition to the cantilever design, [42] added limit stoppers to increase the bandwidth frequency response of the harvester (Figure 1.8).

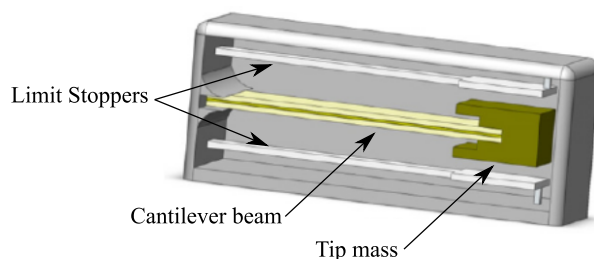


Figure 1.8: Mass-spring system EH with limit stoppers [42].

The same cantilever-based design was used at the microscale using MEMS technology by several authors including [43, 44, 45]. The used harmonic or shock excitation to actuate the inertial mass located at the tip. The Aluminum Nitride (AlN) is used as piezoelectric material in the MEMS energy harvesters. However, the output power was lower than the macroscale version, it was reported that a peak of  $489\mu\text{W}$  can be reached and that the at

70 km/h a mean value of  $42\mu\text{W}$  was observed [43]. Renaud et al. [46] reported improved reliability of similar MEMS energy harvester subject to high shock (1700 g) using stoppers to limit the cantilever beam displacement.

Electromagnetic transducers were also used for energy harvesters attached to the tire. Tornincasa et al. [28] designed a device (Figure 1.9) consisting of a floating permanent magnet which slides in a guide around which, two coils connected in series are wrapped in the opposite direction so that their electromotive force is added. A permanent magnet is placed in the lower part to push the floating magnet to the upper part. The displacement of the floating magnet in the guide caused by the variation of the radial acceleration of the tire, changes the coupling of flux of the coils and produces an electromotive force.

Vibration induced in the tire are highly depending on the quality of the road and the driving style, as a result the energy harvester can be hardly tuned to cover the entire bandwidth of the frequency spectrum where energy can be extracted [29]. Therefore, researcher tried to design their device according to the more abundant frequency in the spectrum.

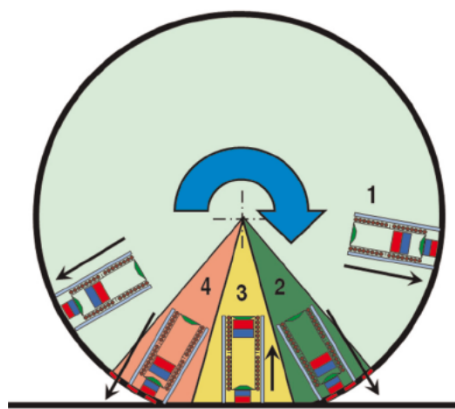


Figure 1.9: Schematic response of the EH during the rotation of the wheel [28].

### 1.3.2 EH FIXED ON THE RIM

Fixing the EH on the rim seems to be a more practical solution. Indeed, it shows a better stability, a less rolling noise, and a simple process for tire exchange. According to Chicone and Feng [47], with a constant angular velocity of the rotating wheel, it's very difficult to extract energy from rotating rim.

**Concepts based on pressure variation :** In a patent, Roundy et al. [48] proposed a device that uses the pressure variation generated by wheel rotation to activate a

piezoelectric membrane. This system presents some limits since the efficiency of the device strongly depends on many environmental parameters such as temperature inside tire and vehicle speed.

**Concepts based on the vibration of the rim** : The principle of piezoelectric cantilever-mass system have been also used as a solution for vibration energy harvesters fixed on the rim. The idea was presented in several contribution and patents with different configurations. Huang et al. [49] designed a vibration energy harvester fixed on the rim, made of a cantilever beam with a single monomorph piezoelectric patch and a mass placed on its free end. With a similar design Mak et al. [50] considered a bimorph configuration using a PZT material. A tip mass was used to reduce the natural frequency of the harvester. Also limit stoppers were used to restrict the maximum displacement, and avoid damage of the piezoceramic. Zheng et al. [51] and Kubba and Jiang [52] designed an asymmetric air-spaced cantilever beam. The idea is to increase the output voltage by increasing the distance between the piezoelectric layer and the neutral axis. The mechanical-to-electrical energy conversion efficiency is improved because air-spaced cantilevers enable the majority of the strain energy to stretch that activates the piezoelectric layer. The design of Zheng and Xu [51] is shown in Figure 1.10.

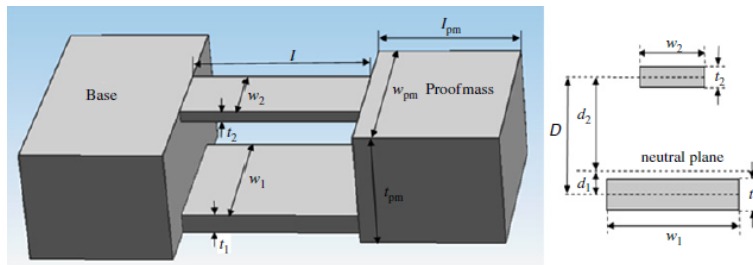


Figure 1.10: EH with asymmetric air-spaced cantilever [51].

**Concepts based on the rotation of the wheel and the gravitational forces** : To overcome the limitation deduced by Chicone and Feng [47] for the difficulty to harvest energy when a constant speed of the vehicle is imposed. In fact, at constant speed all forces on the rim are constants if we neglect the effect of external vibration. Therefore classical design cannot be used to extract energy. Some researchers thought about including the effect of the gravity that can be regarded as a periodic force from the rim point of view.

[53] designed an energy harvester made of two beams, a piezoelectric generating beam and a flexible driving beam with a mass mounted at the free end (Figure 1.11). As the

system is rotating the variable applied force due to gravity on the flexible beam is used to actuate the piezoelectric beam by periodic shocks each rotation of the system. Gu and Livermore [53] also took advantage of the centrifugal force to tune the natural frequency of the flexible beam so that it follows the rotation frequency when a specific mounting radium is imposed.

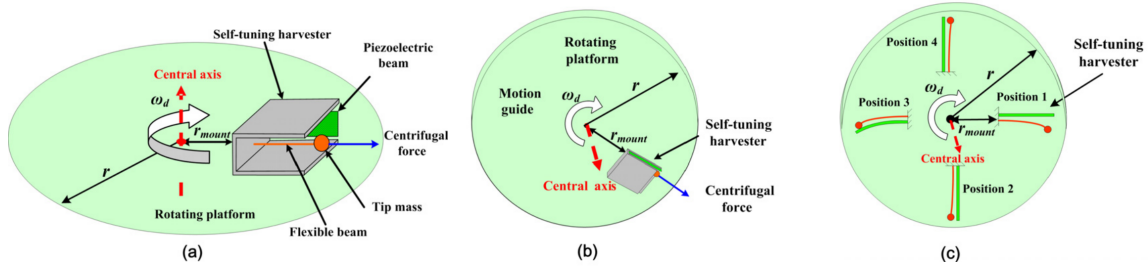


Figure 1.11: Rigid/flexible beams EH system [53].

The same concept can be used with rotating harvesters such as pendulums and take advantage of the periodicity of the gravity to generate electrical power. But, the centrifugal acceleration can largely reduce the effect of the gravity because it imposes a large radial force which tends to cancel the periodic effect of the gravity. In addition, since the centrifugal force is proportional to the square of the rotation speed it can quickly cancel the gravity and force the pendulum to keep a radial quasistatic position that is not suitable to generate energy.

To get around this issue Wang et al. [54] in 2010, proposed a single degree of freedom pendulum where three magnets have been attached to the rotating part of the pendulum at different angular positions. Two coils are attached to the rotating disk supporting the pendulum. As the rotation speed is increased, the magnets activate the coils by inducing an electrical current. The design has been tested analytically, using a point mass system, and experimentally. They proved that the design can harvest several mW of power from the rotation of the wheel [54]. In 2012, the same authors improved their design by replacing the three magnet system by a Halbach array magnetic disk shown in Figure 1.12 [55]. They showed that the electromechanical coupling coefficient is higher for the Halbach array when compared to a multipolar magnetic disk. However, the output power was only around  $550 \mu\text{W}$  for a rotation speed of the disk at 500 rpm (60 km/h). The new design was also tested experimentally both in an experimental setup [56] and mounted into a real car's wheel [57].

Lee et al. [58] proposed also simple pendulum which can directly rotate an electric generator. A single magnet is placed toward the equilibrium position of the swinging mass

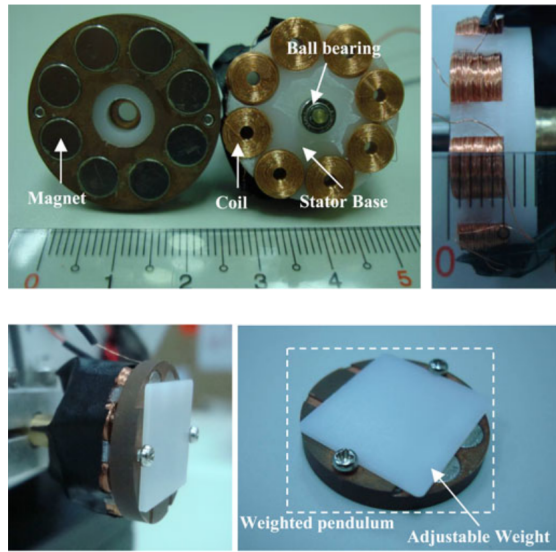


Figure 1.12: Halbach array magnetic disk proposed by Wang et al. [55].

in order to increase the rotation speed of the pendulum that is directly proportional to the harvested power. If the rotation speed is increased, and due to the  $-s$ , the pendulum's arm is released from the magnetic force which also generates high speed motions. If the rotation continues to increase, the magnet is no longer useful.

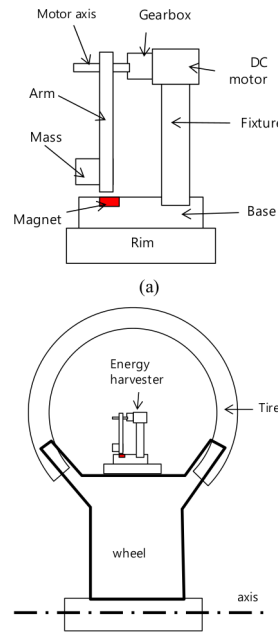


Figure 1.13: Simple pendulum energy harvester with a disturbed static position [58].

Roundy et al. [59] presented a pendulum based energy harvested, where a free ball

is placed in a rotating wheel (Figure 1.14). The ball moves into a curved predisposed track with limit stoppers. Two cantilever piezoelectric beams are placed tangentially to the motion of the ball so that they are deflected each time the ball passes by the center of the track. The design was tested experimentally with a TPMS system mounted into the rim of a vehicle for road test. The output power of  $10 \mu\text{W}$  was enough to feed the TPMS and transmit data each 78 s at 10 km/h.

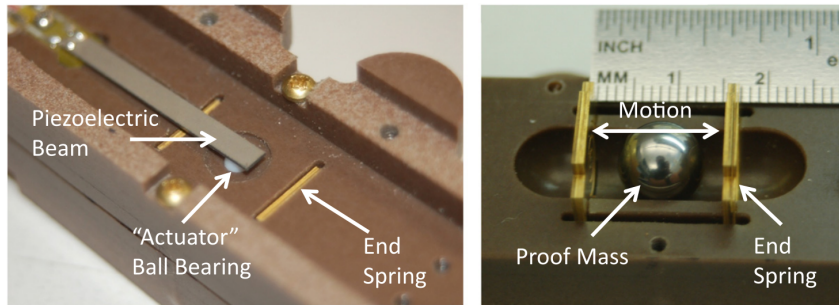


Figure 1.14: Simple pendulum energy harvester with a disturbed static position [58].

## 1.4 ENERGY HARVESTING IN ROTATING SYSTEMS

Rotating systems are one of the most used systems in industrial environment due to the use of rotating motors such as electric motors and combustion and thermal engines. The rotating parts develop high kinetic energy thanks to their large inertia and rotating speed. On the other hand, they are generally balanced so that the rotating masses do not generate large vibrations to avoid premature failure due to fatigue problems. Therefore, classical designs that use mechanical oscillation to harvest the kinetic energy, are not suitable in this case especially because they are optimized for a single frequency while the rotating systems have a large bandwidth frequencies correlated to the rotation speed. Several research groups proposed specific designs to harvest kinetic energy from rotating systems.

### 1.4.1 EH FOR ROTATING SHAFTS

In 2008 Chicone et al. [47] proposed a design consisting on a flexible piezoelectric beam with tip mass mounted into a rotating disk. They analyzed the harvested power through transient behavior of the beam while the rotation speed is varied. They stated that their system cannot harvest energy if the speed is constant and the steady state behavior of the beam is reached.

In a series of papers Toh et al. designed what they presented as a gravitational torque generator [60, 61, 62, 63, 64]. A DC motor was used as generator, its rotor was assembled to a rotating shaft and the stator unbalanced by a large inertial mass. They showed that the effect of gravity can be used to keep the stator's generator fixed with respect to the gravity (Figure 1.15). They showed they a very high power output can be reached (around 1 W at 8000 rpm) if the generator is mounted at the axis of rotation. The power output drops to 10 mW at 500 rpm if the generator is mounted off-axis.

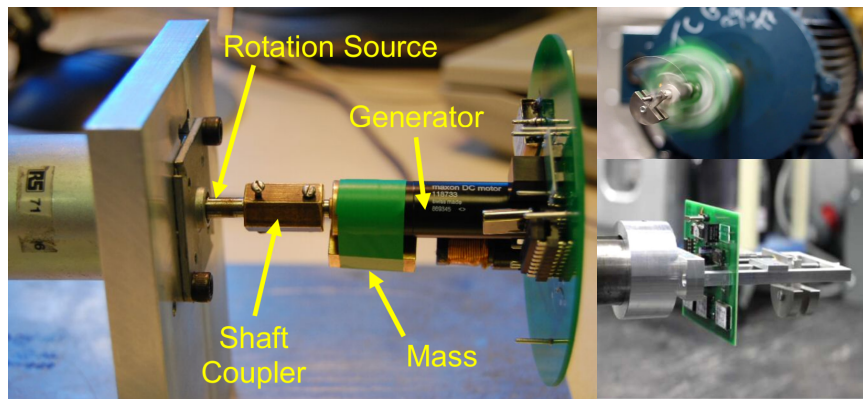


Figure 1.15: Two different version of the system proposed by Toh et al. to harvest energy from a rotating shaft [62, 64].

Karami and Inman [65] also designed a hybrid rotary-translational energy harvester composed of a permanent magnet placed at the tip of the pendulum which passes over a circular array of coils to produce energy. In an other work, Karami and Inman [66] replaced the the array of coils by a DC generator. They proposed a mathematical model for the design and proved analytically that the system can produce up to 10 mW for a translational excitation.

Moss et al. [67] proposed also a hybrid rotary-translational vibration energy harvester using a free magnetic ball motion to generate electrical energy while passing in front of a coil. The system can be used to harvest energy while mounted into a rotating disk, however, the author preferred to test it under harmonic excitation using a shaker. The reported power density was around  $3\mu\text{W}/\text{cm}^3$ .

Flankl et al. [68] proposed a device composed of a wheel with radially magnetized sector magnets which is free to rotate. A stationary extraction coil surrounds the magnetic wheel. The magnet wheel itself interacts over an air gap with a moving conductive body, whose kinetic energy is the source of energy extracted electromagnetically over the air gap. The system was analyzed analytically and a harvested power density of  $2\text{W}/\text{cm}^3$  is

calculated for a contact surface speed of 10m/s.

More recently, Febbo et al. [69] used a clamped-clamped beam with a piezoelectric layer. At the center of the beam an inertial mass is elastically linked to second Clamped-clamped beam. The whole system is mounted into a rotating disk. Experimental setup, shown in Figure 1.16, generated up to 8 V as harvested voltage but its only measured for a small range of rotating speeds.

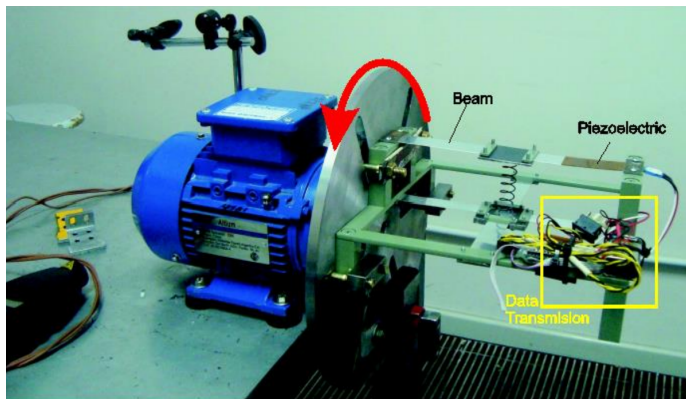


Figure 1.16: Two beams energy harvester for rotating disk [69].

## 1.4.2 PENDULUM IN ENERGY HARVESTING DEVICES

### 1.4.2.1 SELF WINDING WATCHES

Historically pendulums have been used as a main component for self-winding watches since 1773 [70]. The main idea is to place an unbalanced mass (part of a rigid disk) in order to replace the rotation of the knob each time the user wants to wind the spiral mainspring of a portable watch (Figure 1.17). The motion of the unbalanced mass is generated by the motion of the wearer's hand (wrist watches or pocket watches). At the beginning the concept was purely mechanical, however, several other systems proposed the use of the initial rotation of the mass to generate electrical energy so that it can be used to feed classical watch mechanisms such as those using a quartz tuning fork system. The energy is generated by linking the generated inertial motion to a gear train in order to increase the mechanical couple applied to a microgenerator (Figure 1.18 [71]). The output voltage is rectified and stored into a capacitor. Other more complex mechanism have been proposed such as the one using gyroscopic forces with a rotating disk having two perpendicular rotation axis proposed by Yeatman et al. [72].

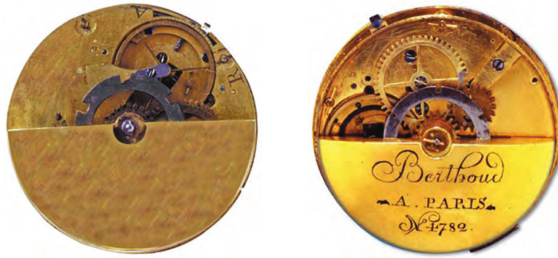
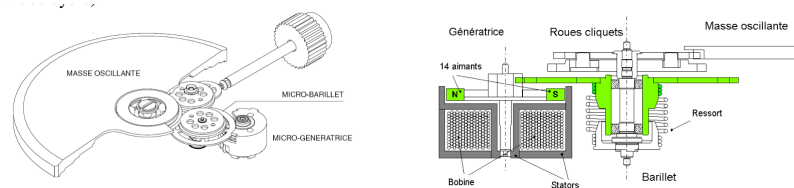
Figure 1.17: 18<sup>th</sup> century pocket watch by Berthoud [70].

Figure 1.18: Modern self-winding mechanism, Lossec et al. [71].

#### 1.4.2.2 PENDULUM IN EH SYSTEMS

Design using the concept of pendulum has been widely used in the literature either as a free rotating mass or when the inertial mass is elastically attached to other components like springs or beams. Lu et al. [73] proposed the use of a semicircular disk as a single degree of freedom pendulum. The pendulum is attached to an elastic component and the total system is subject to base excitation. As a result, the pendulum is parametrically excited so that the generated motion of the mass can rotate a generator. Chao et al [74] continue this analysis by linking the motion of the mass to a previously designed electromagnetic microgenerator by Liao et al. [75]. The experiments conducted by Chao et al [74] showed that, using a specially designed conditioning circuit, the system successfully converted the mechanical energy into DC voltage directly usable in microelectronic environment.

Najdecka [76] proposed a similar system with two springs connected to the inertial mass in two different directions. The developed system was intended to be used in sea wave energy harvesting. Different excitation conditions have been tested with the design including stochastic signals. For a large pendulum carrying a 0.7 kg inertial mass and at 2.5 Hz harmonic excitation, the system was able to harvest 50 W. Similarly, with a rigidly connected rod forming a large single pendulum, Yurchenko et al. [77] increased the moment of inertia of the pendulum and fixed the system into an inclined ramp excited by the waves.

Ma et al. [78] proposed the use of a single pendulum energy harvester directly

connected to a electromagnetic generator, the device showed that up to 10 mW can harvested for low frequency harmonic excitations (2.5 to 4 Hz). Jia et al. [79] improved the design of Ma et al. by linking the pendulum suspension to a lever beam that is connected the a large magnet moving in front of a coil. The lever beam amplifies the motion of the pendulum and induces more harvested power.

A single pendulum with a quarter of disk shape and carrying several magnets is oscillating in front of a electromagnetic coil is proposed by Dai [80]. The authors proved that with harmonic base excitation, rotating solution of the pendulum can be observed experimentally.

## 1.5 PENDULUM THEORY

### 1.5.1 SIMPLE PENDULUM

It is difficult to imagine simpler than a pendulum as single degree of freedom oscillator. And yet, in spite of this simplicity, the pendulum has played a great role in the development of science. In the seventeenth century, he was used by Galileo to confirm the law of falling bodies and Newton to illustrate his laws of dynamics [81]. In the nineteenth century it was used by Leon Foucault to provide the first experimental evidence of the rotation of the Earth on itself [82].

The simpler version of a pendulum is a point mass suspended from a pivot so that it can swing freely. It is an oscillating system which, moved away from its resting equilibrium position, returns there by describing oscillations, under the effect of a restoring force, for example the weight of the mass.

We present here the general equation of motion of a simple pendulum represented by a point mass suspended by a rigid massless rod, shown in Figure 1.19. For small amplitudes of motion, the approximation  $\sin\theta \approx \theta$  [83] can be taken into account, we end up

$$\frac{d^2\theta}{dt^2} + \frac{g}{l}\theta = F(t) \quad (1.1)$$

where  $\theta$  is the angular position of the pendulum,  $g$  the gravity and  $F(t)$  an external applied force.

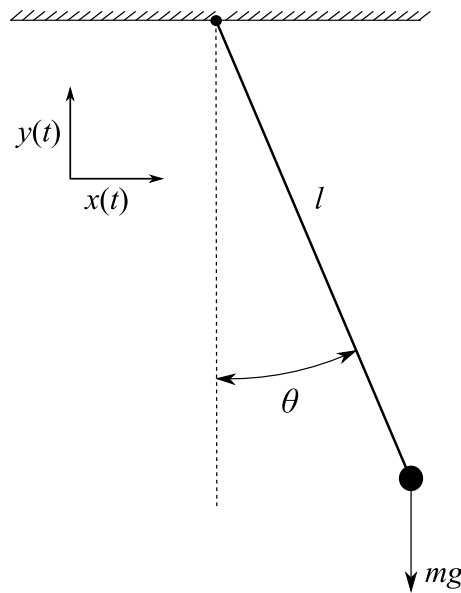


Figure 1.19: Simple pendulum with a moving support.

The time for one complete cycle, is called the period  $T$ . For small amplitudes,  $T$  depends on the length of the string of the pendulum  $L$  and the acceleration of gravity  $g$ . It can be approximated by the following equation :

$$T = 2\pi\sqrt{l/g} \quad (1.2)$$

As shown in Equation (1.2), the period, and therefore the natural frequency, does not depend on the inertia of the suspended mass.

If damping is taken into account the periodic amplitude gradually diminishes, the pendulum will come to rest. Different causes can induce the loss of energy in a mechanical system, such as friction between solid surfaces and drag on the system from fluids and gases. At high speeds, objects moving through the atmosphere experience a drag force that is proportional to the square of the velocity. For slower objects, the drag force may be considered as proportional to the first power of the velocity.

To let a pendulum oscillate continuously, some kind of forcing must be applied to provide an energy infusion that compensates for the energy loss caused by the damping, such as sinusoidal forcing, pulsed forcing, and parametric forcing.

Let us take the case of a pendulum of a particle of mass  $m$  attached to one end of a massless rod of length  $l$ , whose support is under the influence of prescribed acceleration as shown in Figure 1.19.

We apply the Newton's second law of motion in the direction of motion of the rod. We

obtain [84]

$$ml\ddot{\theta} = -c\dot{\theta} - mgsin\theta + m\ddot{Y}(t)sin\theta + m\ddot{X}(t)cos\theta \quad (1.3)$$

where the over dot are derivative with respect to time  $t$ ,  $X(t)$  and  $Y(t)$  are base excitation in the  $x$  and  $y$  directions, respectively, and  $c$  is the viscous damping coefficient. The equation can be transformed to

$$\ddot{\theta} + \frac{c}{ml}\dot{\theta} + \left[\frac{g}{l} - \frac{\ddot{Y}(t)}{l}\right]sin\theta - \frac{\ddot{X}(t)}{l}cos\theta = 0. \quad (1.4)$$

For small amplitudes, Equation 1.4 can be linearized ( $sin\theta \approx \theta$ ) to yield

$$\ddot{\theta} + \frac{c}{ml}\dot{\theta} + \left[\frac{g}{l} - \frac{\ddot{Y}(t)}{l}\right]\theta = \frac{\ddot{X}(t)}{l}. \quad (1.5)$$

Using a time scaling  $t = \hat{t}\tau$ , and assuming that  $X(\hat{t})=0$  and  $Y(\hat{t}) = Y_0 \cos \omega \hat{t}$ , Equation 1.5 becomes

$$\ddot{\theta} + \bar{c}\dot{\theta} + (1 + P \cos \omega \hat{t})\theta = 0 \quad (1.6)$$

where now over dots are derivative with respect to  $\hat{t}$ ,  $P = \frac{Y_0 \omega^2}{g}$  and  $\tau^2 = \frac{l}{g}$ .

Equation 1.6 is a Mathieu equation [85] which defines the response as a parametric oscillator. Indeed, the main concern to use Mathieu equation is whether all solutions are bounded for given values of the parameters  $\delta$  and  $\epsilon$ . If all solutions are bounded then the corresponding point in the  $\delta - \epsilon$  parameter plane is said to be stable. A point is called unstable if an unbounded solution exists.

Garira and Bishop [86] analyzed Equation 1.6 for a parametrically excited single pendulum. They found that the stability of the solution depends on the values of  $\omega$  and  $P$ . The authors showed in Figure 1.20, that a large region of stability exists when  $\omega$  is close to 2. The increase of the parameter  $P$  around  $\omega \approx 2$  (region I) generates limit cycle solutions (gray region) and even chaotic solution if  $P$  is high enough.

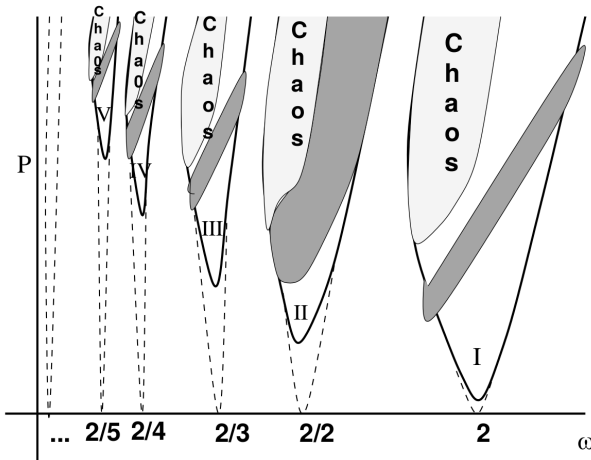


Figure 1.20: Schematic stability diagram of the a system described by Equation 1.6 [86].

Xu and Wiercigroch [87] analyzed the same pendulum as Garira and Bishop [86], however they considered the second order approximation in the sine term, bringing a new cubic nonlinearity term. They found that the limit-cycle solution region is smaller around  $\omega \approx 2$ , if the cubic nonlinearity is taken into account.

### 1.5.2 DOUBLE PENDULUM

A double pendulum is a two degrees of freedom system, which can be consisted as a simple pendulum attached to another simple pendulum (Figure 1.21). A double pendulum presents rich dynamic behavior with a strong sensitivity to initial conditions and possible chaotic motions [88].

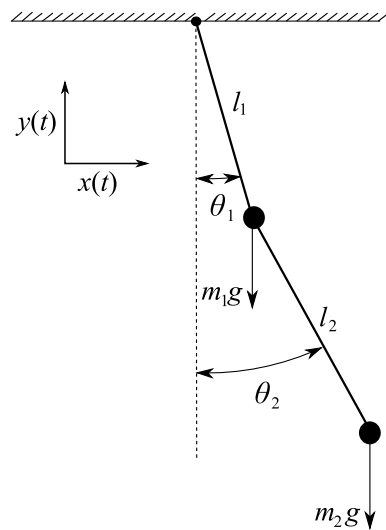


Figure 1.21: Double pendulum with a moving support.

Rafat et al. [89] used a square plates double pendulum as an example of distributed mass pendulum. They showed that chaotic solution can appear at lower energy solutions compared to a classical concentrated mass double pendulum. The parametric resonance of a double pendulum is treated by Sartorelli and Lacarbonara [90]. They constructed the transition curves for the stability and the frequency-response curves using the method of multiple scales and the results are validated using experimental data.

Calvao and Penna [91] analyzed numerically the equations of motion of a double pendulum. They used different integration techniques and compared the results. They also found that the Lyapunov exponent method can be used to predict chaos easily. The method is also useful to predict periodic to quasiperiodic and quasiperiodic to chaos transitions. The quasiperiodic periodic solution of double pendulums is deeply investigated in [92].

Classical double pendulums, such as those presented in Figure 1.21, have their two degrees of freedom generally weakly coupled, each pendulum maintains essentially its own amplitude. If one needs a strong coupling, the ratio of the two fundamental frequencies should be one to two.

Considering that the basic mode is related to the space-fixed pivot (SFP) pendulum, where the attached body performs a pure translation (or two translations). The frequency of the fixed pivot pendulum should be one half or double of that the body-fixed pivot (BFP) pendulum. In fact, when a pendulum is excited by a periodic force, the excitation frequency should match it is own natural frequency to have resonance. If the force is directed exactly to the pivot, in this case the resonant frequency is twice that of the pendulum.

Nikolaus Rott [93] was the first to investigate a double pendulum where the SFP and BPF are horizontally aligned (Figure 1.22). In this case, one can check that for horizontally aligned pivots there two possible cases, as mentioned before, and only one pendulum is oscillating (again two possible cases), the moving pendulum always excites the one at rest at its resonant frequency, although by a second order force, and this holds for all possible combinations of cases. Thus, in every case it is to be expected that the pendulum originally at rest will draw energy from the other, and the possibility exists that finally the process will reverse itself.

For the mathematical point of view, to let the leading coupling effects become quadratic, the two pivots of the pendulum should be aligned in a horizontal line. In this case Rott [93] considered free oscillations of a double pendulum when the frequency of a pivot is the double of the other. He studied the nonlinear interaction between the two pendulum modes, neglecting friction, and also built models of double pendulums in which

he observed energy exchange between the two modes.

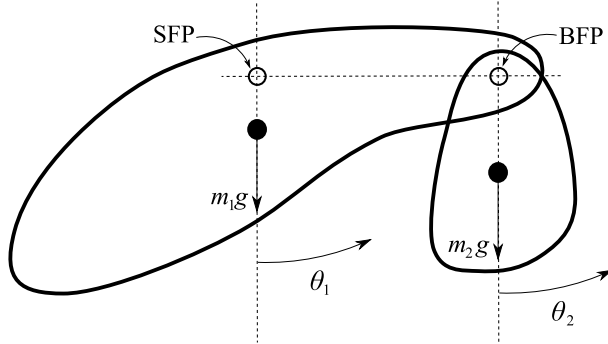


Figure 1.22: Rott's pendulum.

Miles [94] considered parametrically forced and damped oscillations of damped oscillations of the Rott's pendulum when  $\omega_2=\omega_1$  (perfect tuning). He used the method of time-averaged Lagrangian to derive the equations governing the amplitudes and phases of the two modes and found these equations admit only fixed-point solutions corresponding to periodic motions of the double pendulum. There are two types of periodic motions, namely, linear and nonlinear periodic motions. The spectrum of each type of motion consists of one basic frequency. However, linear periodic motions correspond to two-mode vibrations. Becker and Miles [95] considered parametric excitations of a perfectly tuned Rott's pendulum when  $\Omega \approx 2\omega_2$ . They found nonlinear periodic, quasiperiodic, and chaotic motions for certain excitation-parameter values.

Nayfeh [96] considered the same problem when the two-to-one internal resonance is not perfectly tuned ( $\omega_2 \approx 2\omega_1$ ). He found that the modulations equations, derived by using the method of multiple scales, admit periodic solutions besides fixed-point solutions. As a consequence, he found that the system could exhibit periodically and chaotically modulated motions besides periodic motions.

### 1.5.3 ROTATING PENDULUMS

Rotating motion for pendulums are particular solutions of the inertial mass where the position is no longer periodic in time but continues to increase as the system is excited. In 1995, Clifford and Bishop [97] analyzed the rotating solutions of a parametrically excited pendulum. They found that these solutions only exist for forcing amplitude  $P$  higher than a critical value. Garira and Bishop [86] confirmed this results and showed that other rotating solution can occur where oscillation and rotations are alternated. The direction of rotation can be constant with an oscillation phase in this case they are known as *oscillating*

*rotating solution* (for  $\omega=0.25$ ), or *straddling rotating solution* if the direction of rotation is alternated each cycle [86]. Xu et al. [98] confirmed these results using a numerical approach. They found that the rotating and oscillating rotating solution are present in two different region of the phase space. Horton et al. [99] introduced coulomb damping to the same model treated by the previous authors. The model's parameters are identified using an experimental approach. Later Horton et al. [100] proposed to replace the pure parametric excitation with a vertical displacement by an elliptical motion of the pendulum. They showed that the same solutions exist in the case. Vaziri et al. [101] experimentally tested the design with wave excitation, they found that it is still possible to obtain rotating solutions for energy harvesting purposes. Najdecka et al . [102] replaced the single pendulum by two pendulums having the same rotating axis but with independent angular positions. They deduced that synchronization of pendulums rotating in antiphase is more beneficial for energy harvesting applications.

## 1.6 METHODOLOGY AND GENERAL FRAMEWORK

In this work, we propose to exploit the kinetic energy produced by the rotation of a wheel and convert it through electromagnetic transduction to electrical energy. In fact, as shown in the previous state of the art, the electromagnetic transduction is the one that produces the highest energy density for macroscale applications. The pendulum design is the more suitable in this case to self generate motions due to inertial forces. Even if this kind of design has been treated previously as energy harvester, we believe that, thanks to its rich dynamics, it is still worth investigating especially for multibody pendulum, such as the double pendulum and the Rott's pendulum.

The reminder of this thesis will be organized as follows. In Chapter 2, we tackle directly the design problem using simple concentrated mass approach so that the equation of motion are easily derived and solved. Based on these results, In Chapter 3, some design will be tested in a laboratory workbench that emulate the conditions for the rim of a wheel. In Chapter 4, a deeper analytical and numerical dynamic analysis will be proposed for a deep understanding of the dynamics of pendulums in rotating wheels. Finally, conclusions and recommendation for future works will be proposed.



# 2

## ON THE USE OF PENDULUM-BASED ENERGY HARVESTER FOR ROTATING WHEELS

### 2.1 INTRODUCTION

The proof of concept on the use of Pendulum-based energy harvester rotating wheels is tackled in this chapter. Using simple concentrated mass designs to analyze the motion and the possibility to harvest energy from rotating wheels with variable speeds.

The number of degree of freedom to be considered in these designs can vary. However, except the first degree which is restricted to the rotation of the wheel, for convenience the second one should carry the transducer.

We start by presenting and deriving equations of motion of four designs that are taken into study in the transient behavior : Simple pendulum with parallel axis, double pendulum with parallel axes, simple pendulum with non-parallel axis and Rott's pendulum.

In the second part of this chapter we compare different designs in the time domain. Starting by calculating the time response and the RMS value of the angular velocity for each design.

### 2.2 DIFFERENT PENDULUM DESIGNS

In this section several designs are proposed to convert the motion of the wheel into a suitable rotation for the transducer using one or several pendulums. The transducer is supposed to be a purely resistive electric generator easily modeled by viscous damping term [55] in the equation of motion of the energy harvester. The proposed designs are

based on simple or double pendulum and can have parallel or non-parallel axes. A special case of double pendulum with parallel axes, the Rott's pendulum, is also taken as a case of study.

The designs to be considered have in common the first degree of freedom to models the rotating wheel. It is composed of a disk representing the wheel of center  $O$ , mass  $m_0$ , rotating about an axis  $(O, \vec{z}_0)$  of an inertial frame  $(O_0, \vec{x}_0, \vec{y}_0, \vec{z}_0)$  and a local coordinate  $(O, \vec{x}_0, \vec{y}_0, \vec{z}_0)$  with a translation relatively to the Galilean reference  $(O_0, \vec{x}_0, \vec{y}_0, \vec{z}_0)$ . A rod is attached to the perimeter of the disk according to its radial direction along the axis  $(O, \vec{x}_1)$ . In this chapter we consider the case of a standard car wheel with dimensions 195/65 R15.

The vehicle is supposed to be initially at rest and accelerating until reaching a cruising speed in few seconds. Assuming  $\overrightarrow{OO_0} = x_0(t)\vec{x}_0$  giving the position of center of the wheel with respect to the inertial frame.

We suppose that the variation of the speed of the vehicle is following the relation

$$\dot{x}_0(t) = V_0 (1 - e^{-kt}) \quad (2.1)$$

where  $k$  is a parameter representing the acceleration of the vehicle and  $V_0$  is cruising speed. In Figure 2.1, we show an example of the variation of the speed and acceleration of the vehicle as function of time for a cruising speed  $V_0 = 50\text{km/h}$ . The results from Equation 2.1 are compared with experimental data taken from a real car. The speed velocity shown are measured using GPS data from a smart phone.

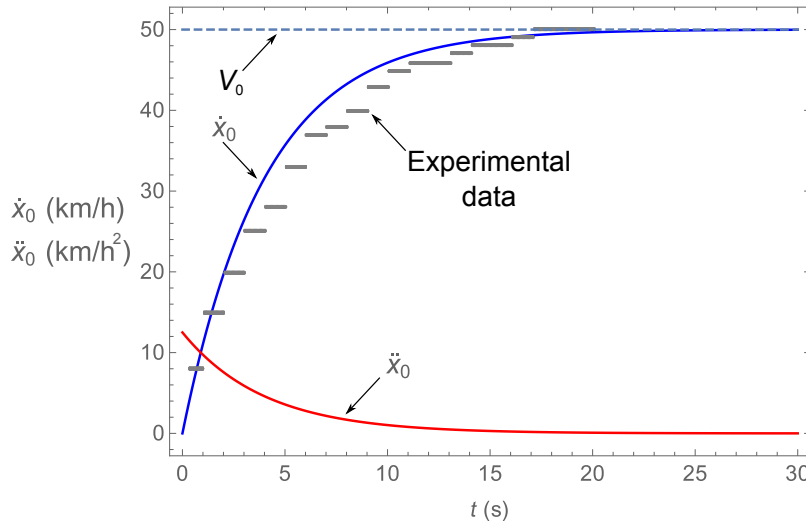


Figure 2.1: Variation of the speed of the vehicle as function of time for a cruising speed  $V_0 = 25\text{km/h}$

We suppose that  $\theta$  is the angle that gives the angular position of the wheel with respect to the inertial frame. For wheels with dimensions 195/65 R15, we obtain that the rim radius is  $R = 0.1905\text{m}$  and that the wheels radius is  $R_0 = 0.31725$ . We supposed that the wheel rolls without slipping, therefore,  $x_0(t) = -R_0\theta(t)$  and the angular position of the wheel is obtained by integrating Equation 2.1, that is

$$x_0(t) = \frac{V_0}{k} (e^{-kt} + kt - 1) \quad (2.2)$$

$$\theta(t) = -\frac{V_0}{R_0 k} (e^{-kt} + kt - 1) \quad (2.3)$$

### 2.2.1 SIMPLE PENDULUM DESIGN WITH PARALLEL AXIS

The first design to be considered is a simple pendulum whose axis is parallel to the axis of the wheel. That is, we add to the rod attached to the wheel a pendulum consisting of a rigid massless rod and a mass  $m$  concentrated at point  $M$ , free to rotate about a revolute joint with axis  $(A, \vec{z}_0)$ . The angle  $\alpha$  locate the mass position with respect to the first rod (see Figure 2.2).

We define a local frame  $(A, \vec{x}_2, \vec{y}_2, \vec{z}_0)$ , attached to the pendulum. Assuming that  $OA = R$  and  $AM = r$ , gives the following position vector of the mass  $m$ :

$$\overrightarrow{O_0M}(t) = x_0(t)\vec{x}_0 + R\vec{x}_1 + r\vec{x}_2 \quad (2.4)$$

The kinetic energy of the mass is:

$$\begin{aligned} K &= \frac{1}{2}m\vec{V}_M^2 = \frac{1}{2}m \left( \frac{d\overrightarrow{O_0M}}{dt} \right)^2 \\ &= \frac{1}{2}m \left[ \left( \dot{x}_0 - R\dot{\theta} \sin \theta - r(\dot{\alpha} + \dot{\theta}) \sin(\alpha + \theta) \right)^2 \right. \\ &\quad \left. + \left( R\dot{\theta} \cos \theta + r(\dot{\alpha} + \dot{\theta}) \cos(\alpha + \theta) \right)^2 \right] \end{aligned} \quad (2.5)$$

For  $\vec{g} = -g\vec{y}_0$ , the potential energy of the mass is given by:

$$\Pi = -mg\cdot\overrightarrow{OM} = -g(R \sin \theta + r \sin(\alpha + \theta)) \quad (2.6)$$

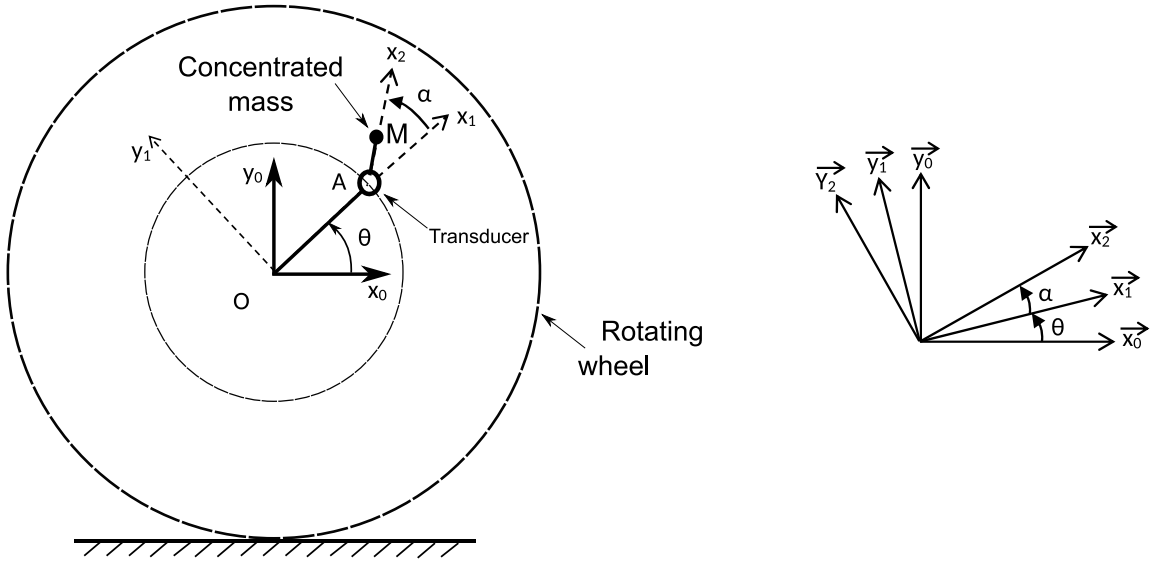


Figure 2.2: Simple pendulum design with parallel axis.

Considering the Lagrangian  $\mathcal{L} = K - \Pi$ , the equation of motion of the mass is obtained by the following Lagrange equation:

$$\frac{d}{dt} \frac{\partial \mathcal{L}}{\partial \dot{\alpha}} - \frac{\partial \mathcal{L}}{\partial \alpha} = -c\dot{\alpha} \quad (2.7)$$

where  $c$  is the damping coefficient which will represent both the structural damping and the electromagnetic damping due to the electrical impedance of the harvesting circuit. Solving Equation 2.7, we end up with

$$m r^2 \ddot{\alpha} + c\dot{\alpha} - (mrR^2 \ddot{x}_0 + mr\ddot{x}_0 \sin(Rx_0) - gmr \cos(Rx_0)) \cos \alpha \quad (2.8)$$

$$+ (mrR^3 \dot{x}_0^2 - mr\ddot{x}_0 \cos(Rx_0) - gmr \sin(Rx_0)) \sin \alpha = mr^2 R \ddot{x}_0$$

In equation 2.8, the unknown of the motion is only the  $\alpha$  angle. The position  $x_0$  and wheel angular position  $\theta$  are given, respectively, by Equations 2.1 and 2.2.

At the steady state the vehicle reaches its cruising speed and the acceleration is supposed to be zero. The position angle of the mass is very small. Equation 2.8 can be reduced to the following form:

$$m r^2 \ddot{\alpha} + c\dot{\alpha} + (mrR^3 V_0^2 - gmr \sin(RV_0 t)) \alpha - \frac{gmr \cos(RV_0 t)}{2} \alpha^2 \quad (2.9)$$

$$- (mrR^3 V_0^2 - gmr \sin(RV_0 t)) \frac{1}{6} \alpha^3 = -gmr \cos(RV_0 t)$$

### 2.2.2 DOUBLE PENDULUM DESIGN WITH PARALLEL AXES

The proposed double pendulum design is obtained by adding an additional revolute joint to the previous design so that the position of the mass  $m$  is parameterized using two angles  $\alpha$  and  $\beta$ . The design is shown in Figure 2.3. All axes of rotation are parallel and the transducer is still located at the first revolute joint in point  $A$ .

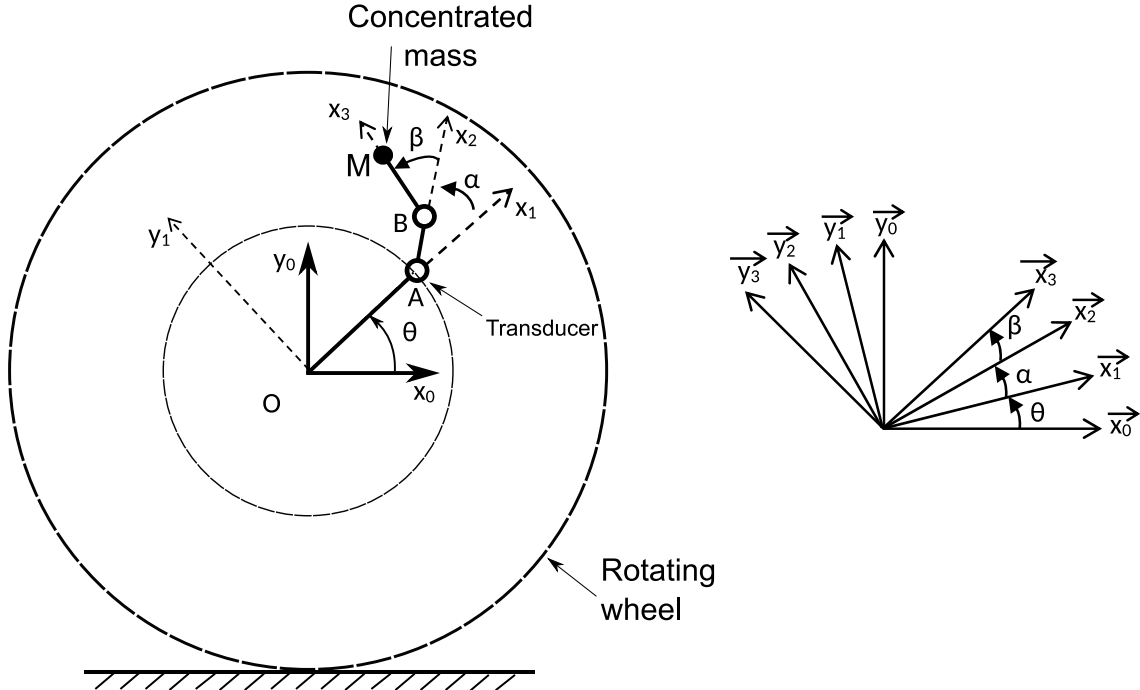


Figure 2.3: Double pendulum system with parallel axes.

We define an additional frame  $(B, \vec{x}_3, \vec{y}_3, \vec{z}_0)$ , attached to the mass and parameterized by the angle  $\beta$ . Assuming that  $OA = R$  and  $AB = BM = \frac{r}{2}$ , gives the following position vector of the mass  $m$ :

$$\overrightarrow{O_0M}(t) = x_0(t)\vec{x}_0 + R\vec{x}_1 + \frac{r}{2}\vec{x}_2 + \frac{r}{2}\vec{x}_3 \quad (2.10)$$

Calculating the associated Lagrangian, and using Equation 2.7, we end up with the equations of motion related to the two degree of freedom.

$$\begin{aligned} & \frac{1}{2}mr^2\ddot{\alpha} + c_1\dot{\alpha} + \frac{1}{4}mr^2\ddot{\beta} - \frac{1}{2}mr^2\dot{\alpha}\dot{\beta}\sin\beta - \frac{1}{4}mr^2\dot{\beta}^2\sin\beta + \frac{1}{4}mr^2\ddot{\beta}\cos\beta \\ & + \frac{1}{2}mr^2\ddot{\alpha}\cos\beta - \frac{1}{2}gmr\cos\left(\alpha + \beta - \frac{x_0}{R}\right) - \frac{1}{2}gmr\cos\left(\alpha - \frac{x_0}{R}\right) + \frac{1}{2R}mr^2\dot{\beta}\dot{x}_0\sin\beta \\ & - \frac{1}{2R}mr^2\ddot{x}_0\cos\beta + \frac{1}{2R}mr\dot{x}_0^2\sin(\alpha + \beta) + \frac{1}{2R}mr\dot{x}_0^2\sin\alpha - \frac{1}{2}mr\ddot{x}_0\sin\left(\alpha + \beta - \frac{x_0}{R}\right) \\ & - \frac{1}{2}mr\ddot{x}_0\sin\left(\alpha - \frac{x_0}{R}\right) - \frac{1}{2}mr\ddot{x}_0\cos(\alpha + \beta) - \frac{1}{2}mr\ddot{x}_0\cos\alpha = \frac{1}{2R}mr^2\ddot{x}_0 \end{aligned} \quad (2.11)$$

$$\begin{aligned} & \frac{1}{4}mr^2\ddot{\beta} + c_2\dot{\beta} + \frac{1}{4}mr^2\ddot{\alpha}\cos\beta + \frac{1}{4}mr^2\ddot{\alpha} + \frac{1}{4}mr^2\dot{\alpha}^2\sin\beta - \frac{1}{4R}mr^2\ddot{x}_0\cos\beta \\ & - \frac{1}{2}gmr\cos\left(\alpha + \beta - \frac{x_0}{R}\right) + \frac{1}{4R^2}mr^2\dot{x}_0^2\sin\beta - \frac{1}{2R}mr^2\dot{\alpha}\dot{x}_0\sin\beta - \frac{1}{2}mr\ddot{x}_0\cos(\alpha + \beta) \\ & + \frac{1}{2R}mr\dot{x}_0^2\sin(\alpha + \beta) - \frac{1}{2}mr\ddot{x}_0\sin\left(-\frac{x_0}{R} + \alpha + \beta\right) = \frac{1}{4R}mr^2\ddot{x}_0 \end{aligned} \quad (2.12)$$

### 2.2.3 SIMPLE PENDULUM DESIGN WITH NON-PARALLEL AXIS

For this design we consider a single pendulum with a rotation axis non-parallel to the wheel axis. It is shown in Figure 2.4 where in this case the angle  $\alpha$  is fixed and can be used as a design parameter.

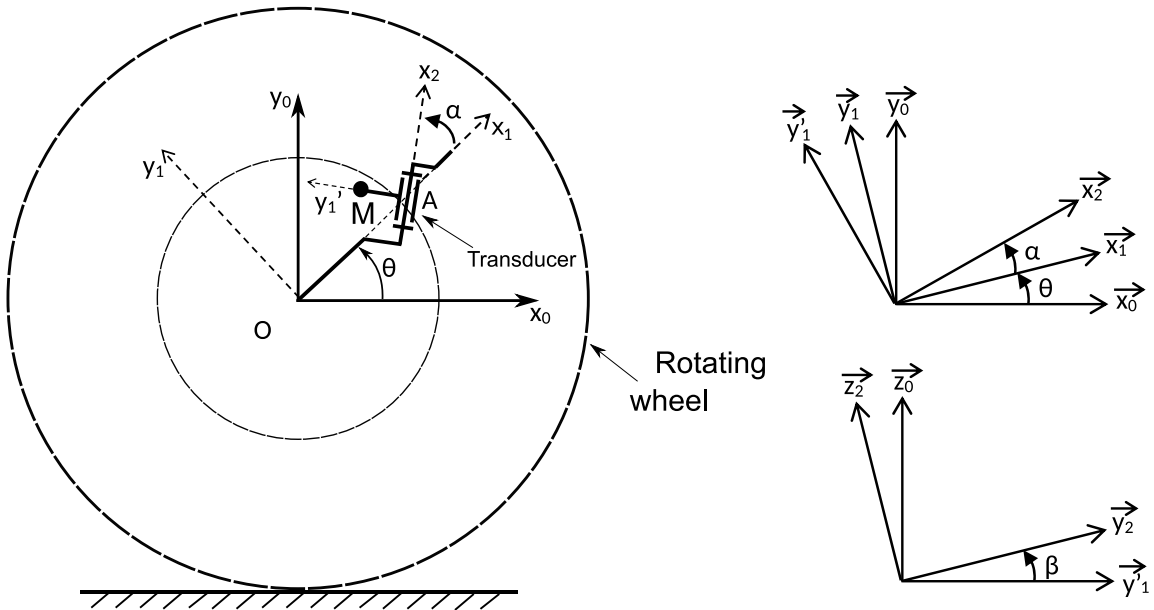


Figure 2.4: Simple pendulum design with non-parallel axis.

The position vector of the concentrated mass is given by considering that  $OA = R$  and  $AM = r$ , by the following relation:

$$\overrightarrow{O_0M}(t) = x_0(t)\vec{x}_0 + R\vec{x}_1 + r\vec{y}_2 \quad (2.13)$$

Expressing the Lagrangian associated to the position vector given by Equation 2.13, we end up with the following equation of motion.

$$\begin{aligned} & mr^2\ddot{\beta} + c\dot{\beta} + mgr\cos\left(\alpha - \frac{x_0}{R}\right)\sin\beta + \frac{mr}{R^2}\dot{x}_0^2\left(\frac{1}{2}r\sin(2\beta) - R\sin\alpha\sin\beta\right) \\ & + mr\sin\beta\ddot{x}_0\left(\cos\alpha + \sin\left(\alpha - \frac{x_0}{R}\right)\right) = 0 \end{aligned} \quad (2.14)$$

### 2.2.4 ROTT'S PENDULUM WITH PARALLEL AXIS

Another interesting design can be included here is the well known Rott pendulum [93]. The pendulum is known to be an autoparametric system with two DOF in which one of the frequencies is exactly the double of the other one. For simplification we model the pendulum by two concentrated masses attached to two rods as shown in Figure 2.5.

Rott pendulum should have some specific properties: first, the pivots of the two pendulums are horizontal when the system is in stable equilibrium. Also, the first pendulum has exactly a period equal to twice that of the second pendulum. This makes it very easy to transfer energy from one pendulum to another, since their oscillations coincide in both periods.

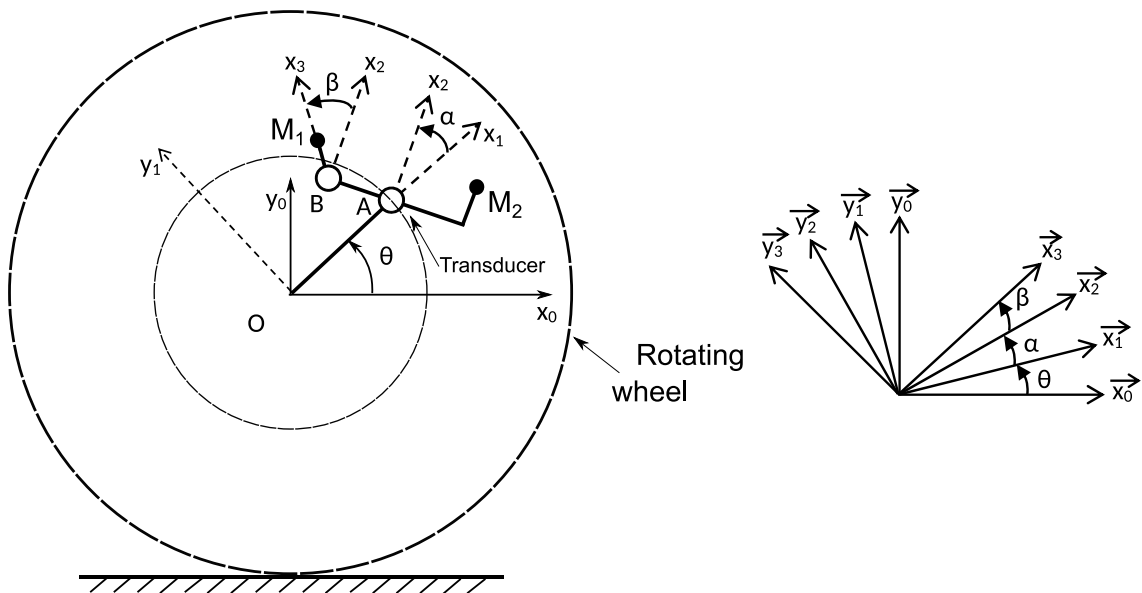


Figure 2.5: Rott's pendulum with parallel axis.

Assuming that  $OA = R$ ,  $AB = r_1$  and  $BM_1 = r_2$ , and that the two masses are equal and symmetric, the position vectors of the two masses in  $M_1$  and  $M_2$  are described as follows:

$$\overrightarrow{O_0M_1} = x_0(t)\vec{x}_0 + R\vec{x}_1 + r_1\vec{y}_2 + r_2\vec{x}_3 \quad (2.15)$$

$$\overrightarrow{O_0M_2} = x_0(t)\vec{x}_0 + R\vec{x}_1 - r_1\vec{y}_2 + r_2\vec{x}_3 \quad (2.16)$$

The kinetic energy of the Rott's pendulum is given by

$$K = \frac{1}{2}m\vec{V}_{M_1}^2 + \frac{1}{2}m\vec{V}_{M_2}^2 = \frac{1}{2}m\left(\frac{d\overrightarrow{O_0M_1}}{dt}\right)^2 + \frac{1}{2}m\left(\frac{d\overrightarrow{O_0M_2}}{dt}\right)^2 \quad (2.17)$$

Also the potential energy of the Rott's pendulum is given by:

$$\Pi = -m\vec{g} \cdot \overrightarrow{OM_1} - m\vec{g} \cdot \overrightarrow{OM_2} \quad (2.18)$$

Expressing the Lagrangian associated to the kinetic and potential energies given by Equations 2.17 and 2.18, we end up with the following equations of motion.

$$\begin{aligned} & 2m(r_1^2 + r_2^2)\ddot{\alpha} + mr_2^2\ddot{\beta} + c_1\dot{\alpha} - gmr_2 \cos\left(\alpha + \beta - \frac{x_0}{R}\right) - gmr_2 \cos\left(\alpha - \frac{x_0}{R}\right) \\ & + mr_1r_2\left(2\ddot{\alpha} + \ddot{\beta} - \frac{2}{R}\ddot{x}_0\right)\sin\beta + mr_1r_2\left(2\dot{\alpha} + \dot{\beta} - \frac{2}{R}\dot{x}_0\right)\dot{\beta}\cos\beta \\ & - mr_2\ddot{x}_0\left(\sin\left(-\frac{x_0}{R} + \alpha + \beta\right) - \sin\left(\alpha - \frac{x_0}{R}\right) - \cos(\alpha + \beta) - \cos\alpha\right) \\ & + \frac{1}{R}mr_2\dot{x}_0^2(\sin(\alpha + \beta) + \sin\alpha) = \frac{2}{R}m(r_1^2 + r_2^2)\ddot{x}_0 \end{aligned} \quad (2.19)$$

$$\begin{aligned} & mr_2^2\ddot{\alpha} + mr_2^2\ddot{\beta} + c_2\dot{\beta} - gmr_2 \cos\left(\alpha + \beta - \frac{x_0}{R}\right) + mr_1r_2\ddot{\alpha}\sin\beta \\ & - mr_1r_2\dot{\alpha}^2\cos\beta + \frac{1}{R}mr_1r_2\dot{x}_0\left(2\dot{\alpha} - \frac{\dot{x}_0}{R}\right)\cos\beta + \frac{1}{R}mr_2\dot{x}_0^2\sin(\alpha + \beta) \\ & - \frac{1}{R}mr_1r_2\ddot{x}_0\sin\beta - mr_2\ddot{x}_0\left(\sin\left(\alpha + \beta - \frac{x_0}{R}\right) + \cos(\alpha + \beta)\right) = \frac{1}{R}mr_2^2\ddot{x}_0 \end{aligned} \quad (2.20)$$

To satisfy the Rott's pendulum conditions for the natural frequencies, we linearize Equations 2.19 and 2.20 around  $\alpha = 0$  and  $\beta = 0$  when  $\theta = -\frac{\pi}{2}$ . As a result we can calculate the natural frequencies of the two pendulums given by:

$$\omega_{R1} = \sqrt{\frac{g}{r_2}} \quad (2.21)$$

$$\omega_{R2} = \sqrt{\frac{gr_2}{r_1^2 + r_2^2}} \quad (2.22)$$

where  $\omega_{R1}$  is the circular natural frequency of the small pendulum and  $\omega_{R2}$  is the circular natural frequency of the large one.

The Rott condition is given by  $\frac{\omega_{R1}}{\omega_{R2}} = 2$ . Therefore, the relation between the two characteristic lengths of the Rott pendulum is given by

$$r_1 = \sqrt{3}r_2 \quad (2.23)$$

In order to keep the same order of dimensions compared to the previous pendulums, we choose  $r_1 = \frac{r}{2}$ . As a result  $r_2 = \frac{r}{2\sqrt{3}}$ .

## 2.3 COMPARISON OF DIFFERENT DESIGNS IN THE TIME DOMAIN

For the external dimensions of the test wheel is codified by 195/65 R15, which means that the rim diameter is 15inches (381mm), the tire thickness equals to 126.75mm which gives a total radius of 317.25mm and a circumference of 1993mm. The parameters of the proposed system are summarized in Table 2.1.

$R$ (mm)	$r$ (mm)	$m$ (kg)	$g$ ( $\text{m/s}^2$ )
190.5	20	0.01	9.81

Table 2.1: Specifications of the pendulum EH

To convert the kinetic energy into electrical energy, it is proposed to use an electromagnetic transduction element. So that the harvested energy is proportional to the angular velocity at the first DOF of the pendulum, i.e.  $\dot{\alpha}$ .

In the following sections, we propose to solve the derived nonlinear equations of motions for the proposed pendulums with a time domain analysis using a Runge-Kutta discretization technique. The time response of the different design will be analyzed along with the variation of the angular velocity  $\dot{\alpha}$  when the vehicle is accelerated from rest position to the cruising speed according to the curve presented in Figure 2.1 and Equation 2.2.

### 2.3.1 TIME RESPONSE OF THE SIMPLE PENDULUM WITH PARALLEL AXIS

The pendulum described in Figure 2.2 and described by Equation 2.8 is treated by numerically solving its equation of motion in time using angular position corresponding to the initial configuration where  $\theta(0) = 0$  and  $\alpha(0) = -\frac{\pi}{2}$  and  $\dot{\alpha}(0) = 0$ . The results are presented in Figure 2.6 for the angular position  $\alpha$  of the transducer axis when its is subject to different damping coefficients ( $c = 0.01$ ,  $c = 0.05$ ,  $c = 0.2$  and  $c = 0.5$ ) and  $V_0 = 50\text{km/h}$ . Since electromagnetic transducer are sought we are also interested in the time response of the angular velocity  $\dot{\alpha}$ . It is shown in Figure 2.7. In both figures, the time is represented by the number of rotations of the wheel. As expected, the lower the damping coefficient the higher oscillations are. For the angular velocity it is anticipated that the blue curve for  $c = 0.01$  will gives the highest harvested energy.

Also, since the transient response is of paramount importance in this case, the initial condition of the angle  $\alpha$  is also very important. To quantify the performance of the design,

we propose to calculate the RMS value of the angular velocity  $\dot{\alpha}$  for the several periods of motion. The RMS value is defined by

$$\dot{\alpha}_{RMS} = \sqrt{\frac{1}{t_s} \int_0^{t_s} \dot{\alpha}^2(t) dt} \quad (2.24)$$

where  $t_s$  is the time of the simulation. For the case shown in Figures 2.6 and 2.7 it is fixed to  $t_s = 20s$  corresponding to 111.67 rotations of the wheel.

The trajectory of the mass point  $M$  in the frame  $(A, \vec{x}_1, \vec{y}_1, \vec{z}_0)$  for a damping coefficient  $c = 0.01$  and  $\alpha(0) = -\frac{\pi}{2}$  is shown in Figure 2.8. The trajectory is a fourth circle because it starts from the position  $\alpha(0) = -\frac{\pi}{2}$  and ends with small oscillations around the equilibrium position generated because of the centrifugal forces at  $\alpha(0) = 0$ .

Using Equation 2.24 we calculate the RMS values of the angular velocity for different damping coefficients whose time response is given by 2.7 for  $\alpha(0) = 0$ . The results are shown in Table 2.2

Table 2.2: RMS values of the angular velocity for different damping coefficients and  $\alpha(0) = 0$

$c$	0.01	0.05	0.2	0.5
$\dot{\alpha}_{RMS}$ (rd/s)	0.2671	0.1683	0.1170	0.0878

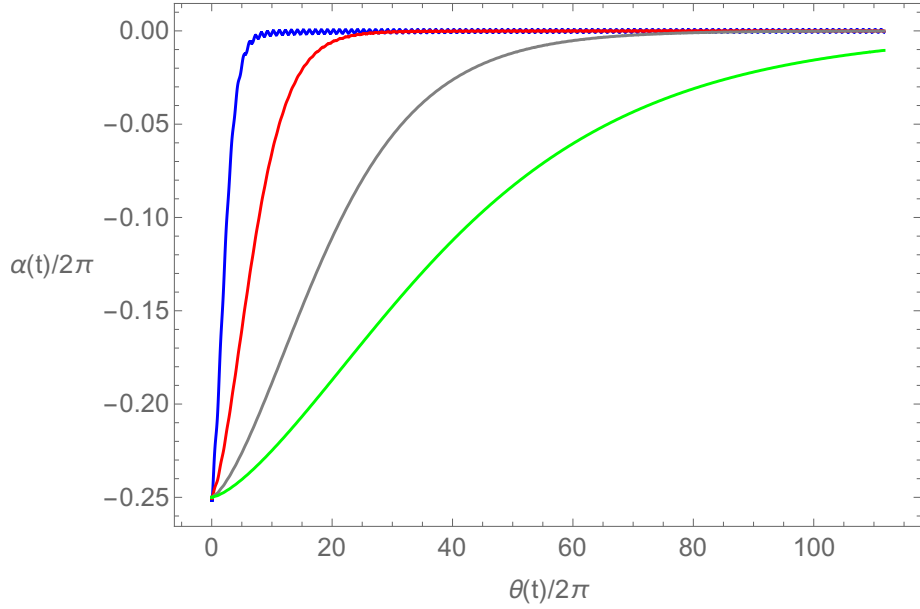


Figure 2.6: Time response of the angular position  $\alpha$  for a simple pendulum with parallel axis for different damping coefficients (Blue curve  $c = 0.01$ , Red curve  $c = 0.05$ , Grey curve  $c = 0.2$  and Green curve  $c = 0.5$ ).

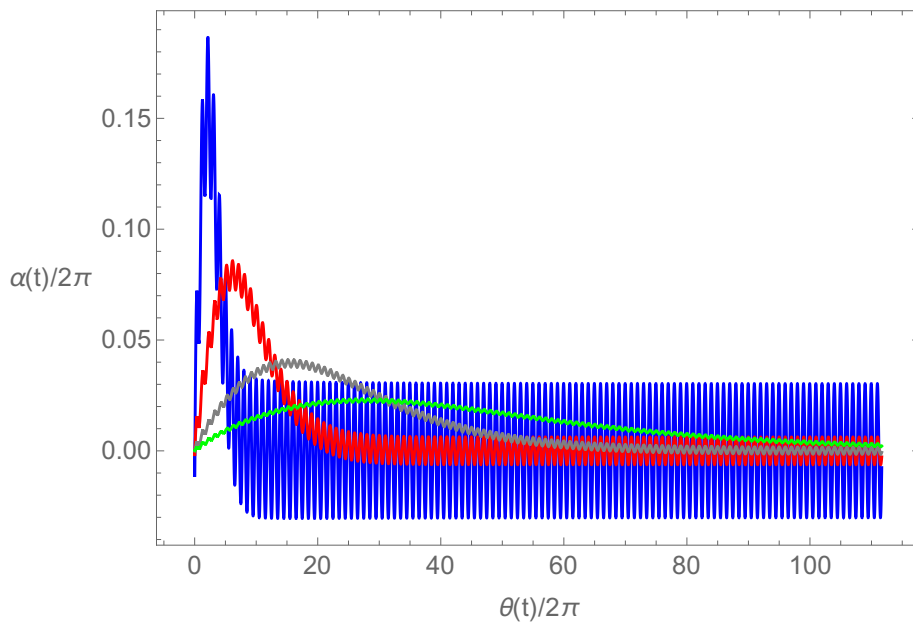


Figure 2.7: Time response of the angular velocity  $\dot{\alpha}$  for a simple pendulum with parallel axis for different damping coefficients (Blue curve  $c = 0.01$ , Red curve  $c = 0.05$ , Grey curve  $c = 0.2$  and Green curve  $c = 0.5$ ).

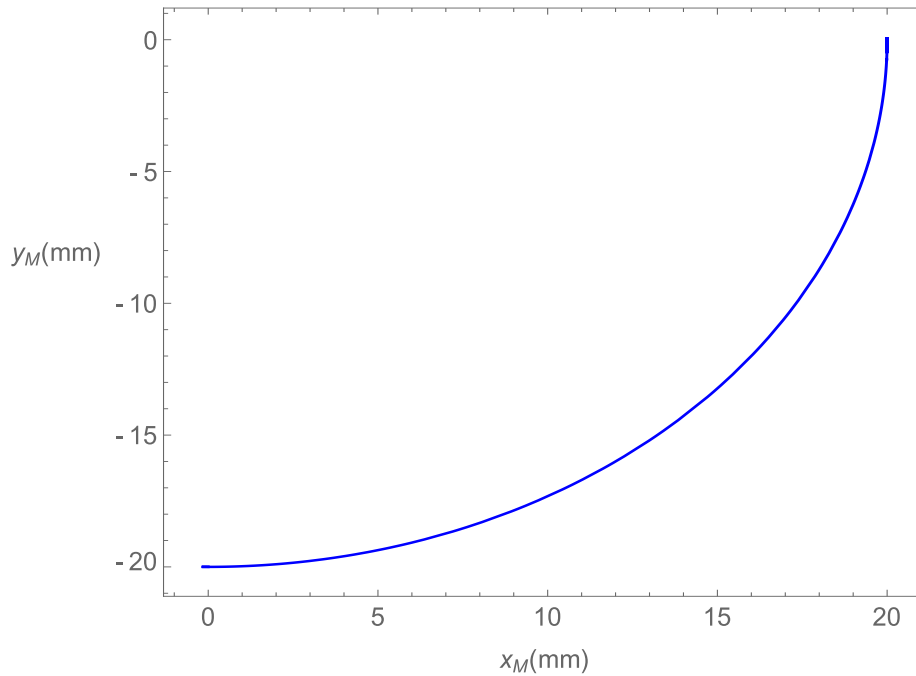


Figure 2.8: Trajectory of the mass point  $M$  in the frame  $(O, \vec{x}_1, \vec{y}_1, \vec{z}_0)$  for a damping coefficient  $c = 0.01$  and  $\alpha(0) = -\frac{\pi}{2}$  for a simple pendulum with parallel axis.

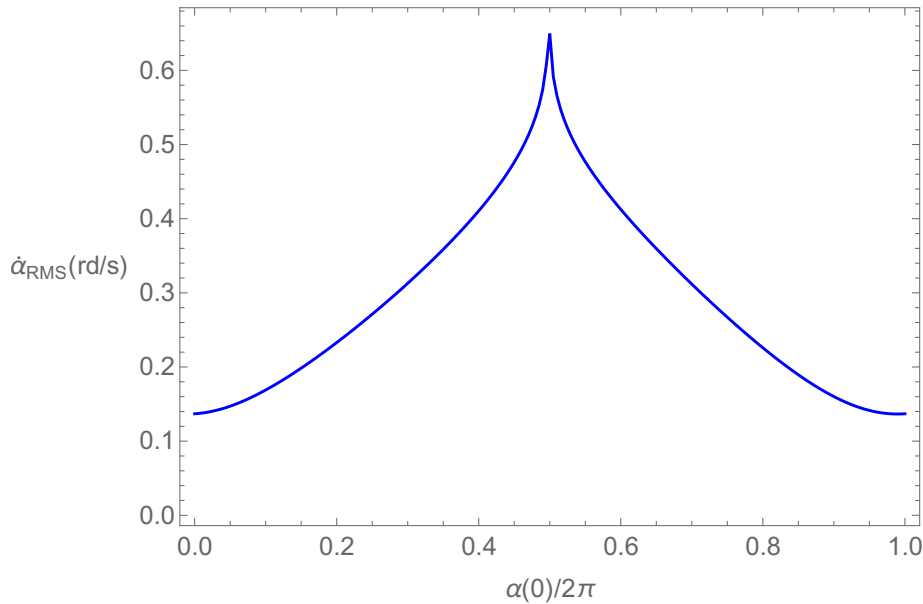


Figure 2.9: RMS values of the angular velocity  $\dot{\alpha}_{RMS}$  for a damping coefficient  $c = 0.01$  and different initial conditions  $\alpha(0)$  for a simple pendulum with parallel axis.

In Figure 2.9 we calculate the RMS values of the angular velocity  $\dot{\alpha}_{RMS}$  for a damping coefficient  $c = 0.01$  and different initial conditions  $\alpha(0)$ . As shown, the maximum value of the  $\dot{\alpha}_{RMS}$  is obtained for  $\alpha(0) = \pi$  at 0.65, which is the value giving the largest amplitude. However, since the initial angle is arbitrary it cannot be treated as a design parameter.

### 2.3.2 TIME RESPONSE OF THE DOUBLE PENDULUM WITH PARALLEL AXIS

For the double pendulum, a additional DOF is added, as shown in Figure 2.3, the transducer is still mounted at the first DOF, therefore we are still interested in this case to the variation of  $\alpha(t)$  with respect to the wheel position  $\theta(t)$ .

The time response of  $\alpha(t)$  is presented in Figure 2.10 when  $\alpha(0) = -\frac{\pi}{2}$  and  $\beta(0) = 0$ . It is shown that the response is qualitatively very similar to the first design with a single pendulum. Also the variation of the angular velocity  $\dot{\alpha}(t)$  with respect to the wheel position is shown in Figure 2.11. Here, even if the response is similar to the first case, the observed peak amplitudes are lower in this case.

The trajectory of the point mass  $M$  is, in this case, more sophisticated because of the additional DOF. The trajectory shown in Figure 2.12 first circular around the point  $B$ , then, as the solution tend to reach the steady state, the double beam design with its two DOF stretches out and behaves as it is only with one DOF, under the strong effect of the centrifugal force.

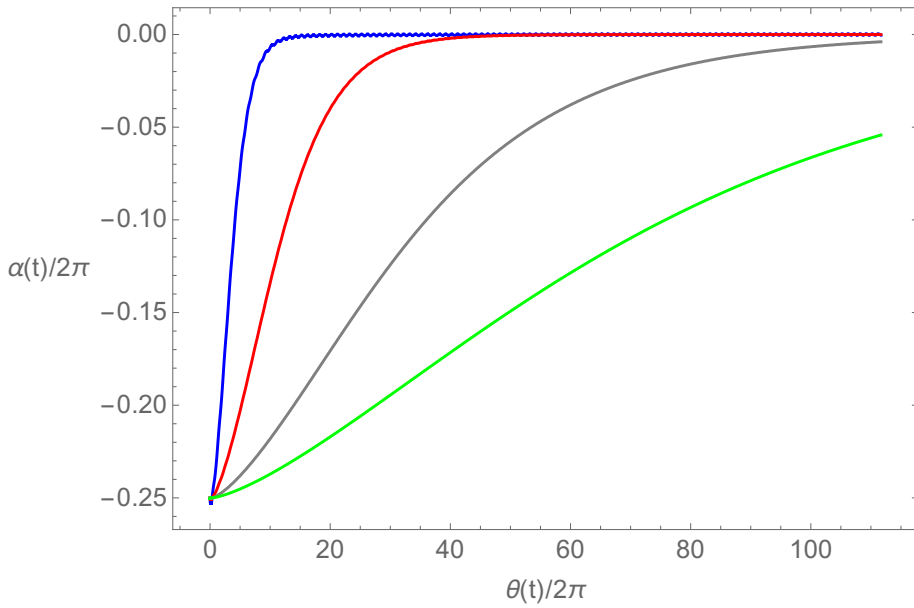


Figure 2.10: Time response of the angular position  $\alpha$  for a double pendulum with parallel axis with different damping coefficients (Blue curve  $c_1 = 0.01$ , Red curve  $c_1 = 0.05$ , Grey curve  $c_1 = 0.2$  and Green curve  $c_1 = 0.5$ ,  $c_2 = 0.0001$ ).  $\alpha(0) = -\frac{\pi}{2}$  and  $\beta(0) = 0$

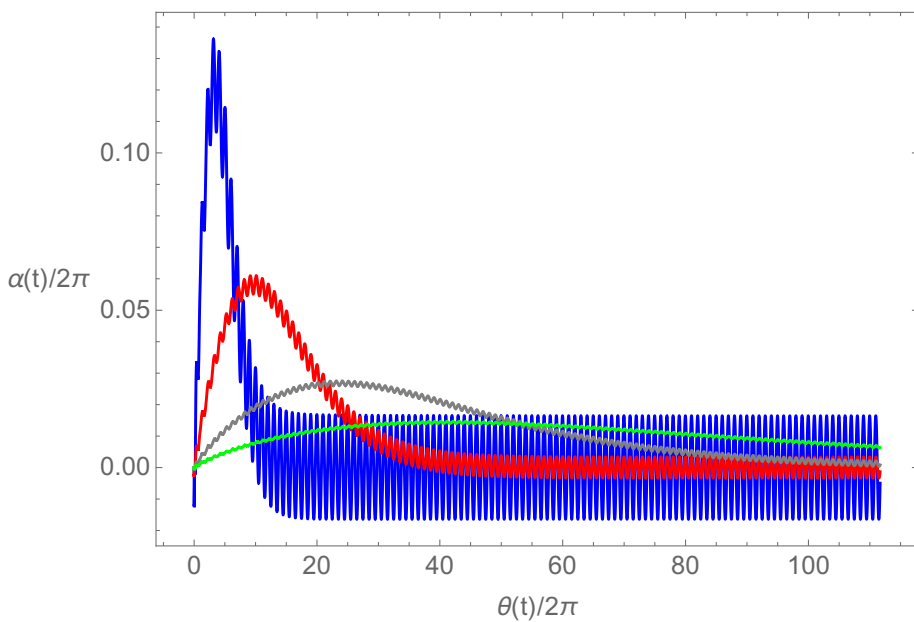


Figure 2.11: Time response of the angular velocity  $\dot{\alpha}$  for a double pendulum with parallel axis with different damping coefficients (Blue curve  $c_1 = 0.01$ , Red curve  $c_1 = 0.05$ , Grey curve  $c_1 = 0.2$  and Green curve  $c_1 = 0.5$ ,  $c_2 = 0.0001$ ).  $\alpha(0) = -\frac{\pi}{2}$  and  $\beta(0) = 0$

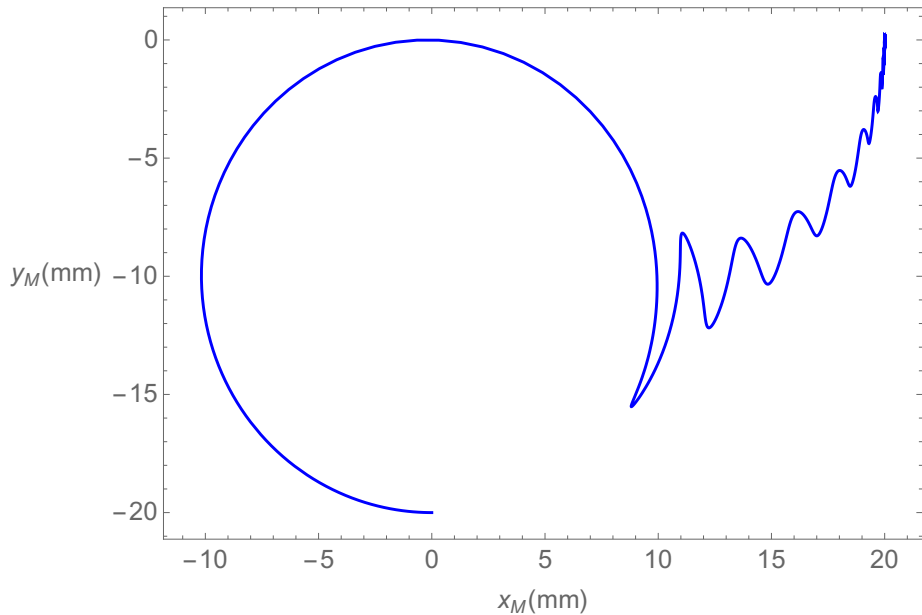


Figure 2.12: Trajectory of the point mass  $M$  when  $\alpha(0) = -\frac{\pi}{2}$  and  $\beta(0) = 0$  for a double pendulum with parallel axes.

Similarly to the previous design we use Equation 2.24 to calculate the RMS values of the angular velocity. The results are shown in Table 2.3. Comparing the values in Tables 2.2 and 2.3, we deduce that the first design is more likely to produce energy than the second one with double pendulum.

Table 2.3: RMS values of the angular velocity for different damping coefficients,  $c_2 = 0.0001$  and  $\alpha(0) = -\frac{\pi}{2}$

$c_1$	0.01	0.05	0.2	0.5
$\dot{\alpha}_{RMS}$ (rd/s)	0.2206	0.1432	0.0957	0.0665

In Figure 2.13 we show the RMS values of the angular velocity  $\dot{\alpha}_{RMS}$  for a damping coefficient  $c = 0.01$  and different initial conditions  $\alpha(0)$ . The maximum value of the  $\dot{\alpha}_{RMS}$  is still located around  $\alpha(0) = \pi$ . The values depicted by 2.13 confirm the conclusion issued from Table 2.3, that the single pendulum design is more efficient than the double pendulum in terms of RMS value of the angular velocity. In Figure 2.13 the maximum RMS value is 0.524 at  $\alpha(0) = \pi$

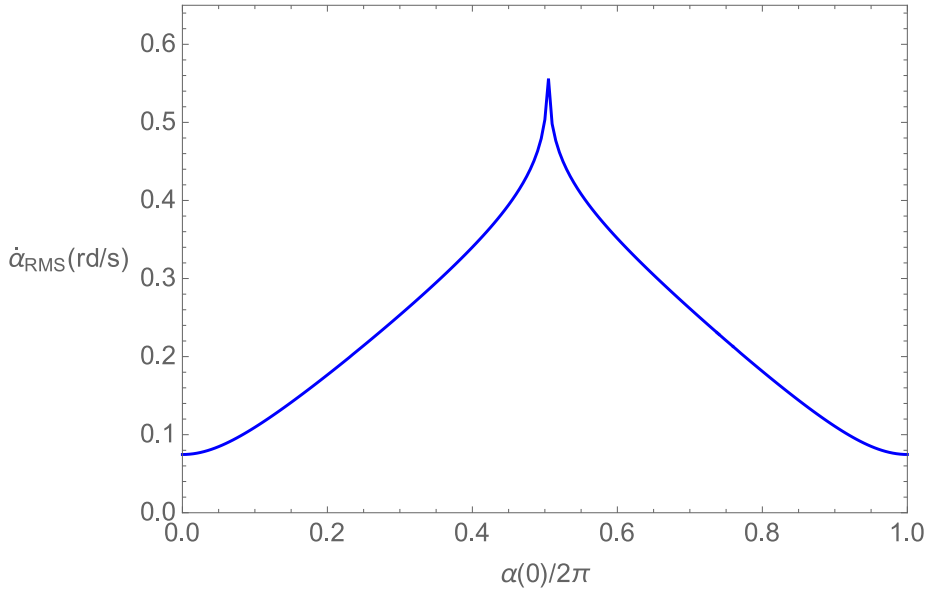


Figure 2.13: RMS values of the angular velocity  $\dot{\alpha}_{RMS}$  for a damping coefficient  $c = 0.01$  and different initial conditions  $\alpha(0)$  for a double pendulum with parallel axis when  $\beta(0) = 0$ .

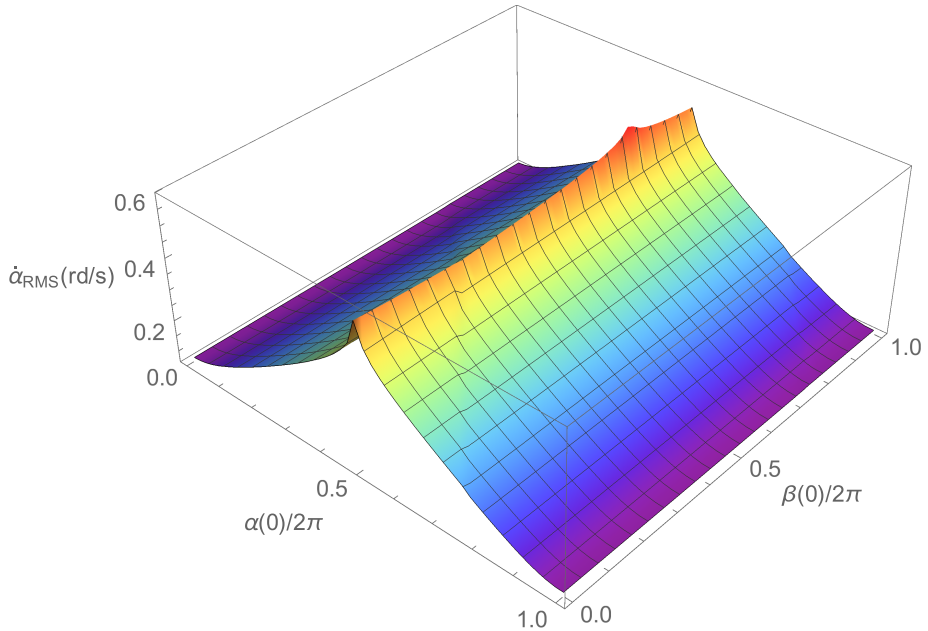


Figure 2.14: RMS values of the angular velocity  $\dot{\alpha}_{RMS}$  for a damping coefficient  $c = 0.01$  and different initial conditions  $\alpha(0)$  for a double pendulum with parallel axis when  $\beta(0) = 0$ .

As we vary the initial condition  $\beta(0)$  the RMS value can also be changed. In order to look at the maximum value of  $\dot{\alpha}_{RMS}$  for all initial conditions, we propose in Figure 2.14 to vary all initial condition, namely  $\alpha(0)$  and  $\beta(0)$ . As observed the maximum value is

obtained at  $\beta(0) = 0.8 \times 2\pi$  and it is  $\dot{\alpha}_{RMS} = 0.615$ .

### 2.3.3 TIME RESPONSE OF THE SIMPLE PENDULUM WITH NON-PARALLEL AXIS

For the pendulum with non-parallel axis described by Figure 2.4, we analyze the time response of the system by fixing the value of the geometric angle  $\alpha$  to a predefined value and solve for the time response of  $\beta$  where the transducer is located.

For the case where the initial conditions are  $\alpha = 0$  and  $\beta(0) = -\frac{\pi}{2}$ , we plot the results shown in Figures 2.15 and 2.16 for, respectively, the angular position  $\beta(t)$  and angular velocity  $\dot{\beta}(t)$ . The figures demonstrate that the angle  $\beta(t)$  tend to converge toward the value  $-\pi$  at the steady state. For the duration of the simulation, fixed for all cases at 20s, only the response for  $c = 0.01$  reaches this value. As a result the angular velocities depict high oscillations for the case where  $c = 0.01$ . For the other cases only small variations are observed. For all cases, the angular velocity tends to stabilize to a periodic solution due to the effect of the gravity on the mass.

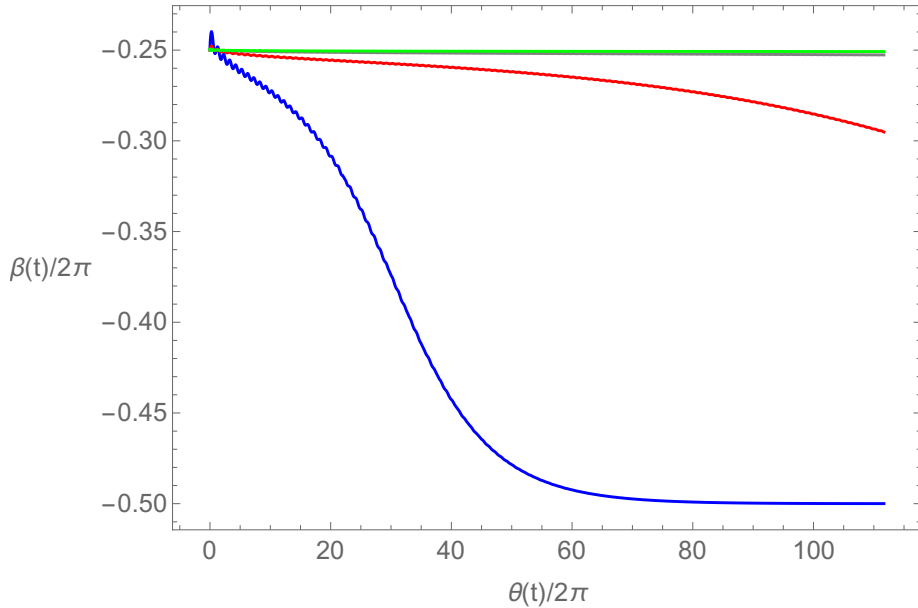


Figure 2.15: Time response of the angular position  $\alpha$  for a simple pendulum with non-parallel axis with different damping coefficients (Blue curve  $c = 0.01$ , Red curve  $c = 0.05$ , Grey curve  $c = 0.2$  and Green curve  $c = 0.5$ ).

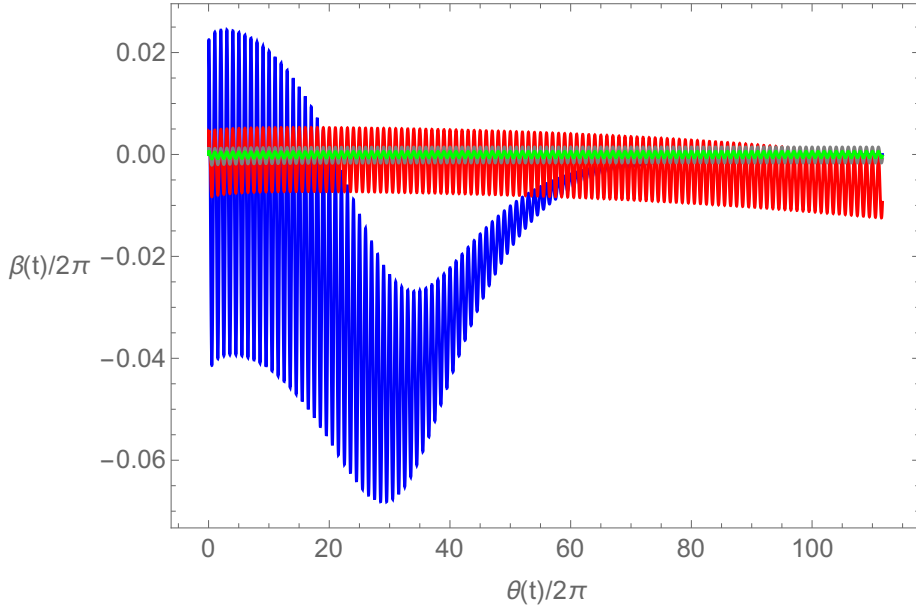


Figure 2.16: Time response of the angular velocity  $\dot{\alpha}$  for a simple pendulum with non-parallel axis with different damping coefficients (Blue curve  $c = 0.01$ , Red curve  $c = 0.05$ , Grey curve  $c = 0.2$  and Green curve  $c = 0.5$ ).

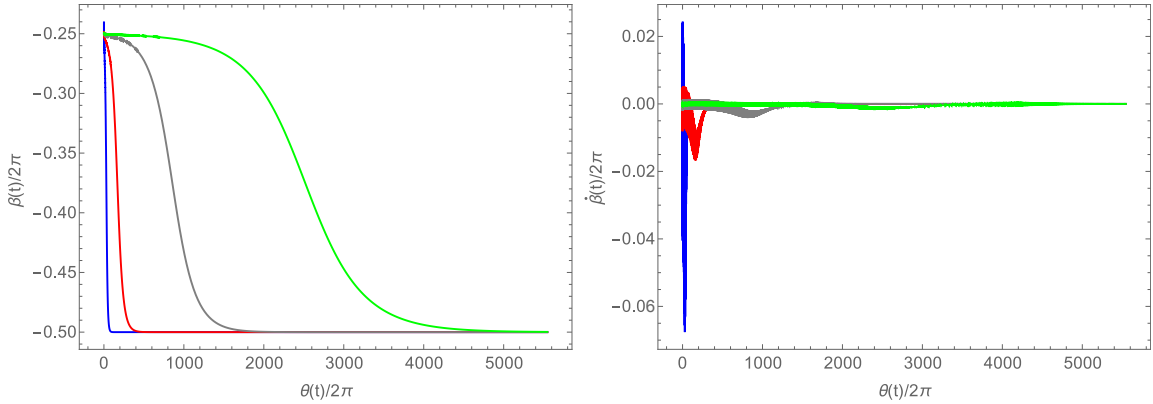


Figure 2.17: Time response of the angular position and velocity for a simple pendulum with non-parallel axis with different damping coefficients (Blue curve  $c = 0.01$ , Red curve  $c = 0.05$ , Grey curve  $c = 0.2$  and Green curve  $c = 0.5$ ).

If the simulation time is increased to 800s, we show in Figure 2.17 that the convergence toward the value  $\beta = -\pi$  is influenced by the value of the damping coefficient. It is delayed as the damping is increased. According to the same figure, the angular velocity is very large when the damping coefficient is small.

The trajectory of the point mass  $M$  is shown in Figure 2.18 plotted in the frame

$(A, \vec{x}_1, \vec{y}_1, \vec{z}_0)$ . As shown the fourth circular since the initial condition is fixed at  $\beta(0) = -\frac{\pi}{2}$ . The response is very similar to the first proposed design.

We compute the RMS value of the angular velocity  $\dot{\beta}_{RMS}$  for a 20s simulation when  $\alpha = 0$ . In Table 2.4 we give the results for different damping coefficients. It is shown that the values are lower than the previous design.

Table 2.4: RMS values of the angular velocity for different damping coefficients,  $\alpha = 0$

$c$	0.01	0.05	0.2	0.5
$\dot{\beta}_{RMS}$ (rd/s)	0.1485	0.0328	0.0070	0.0028

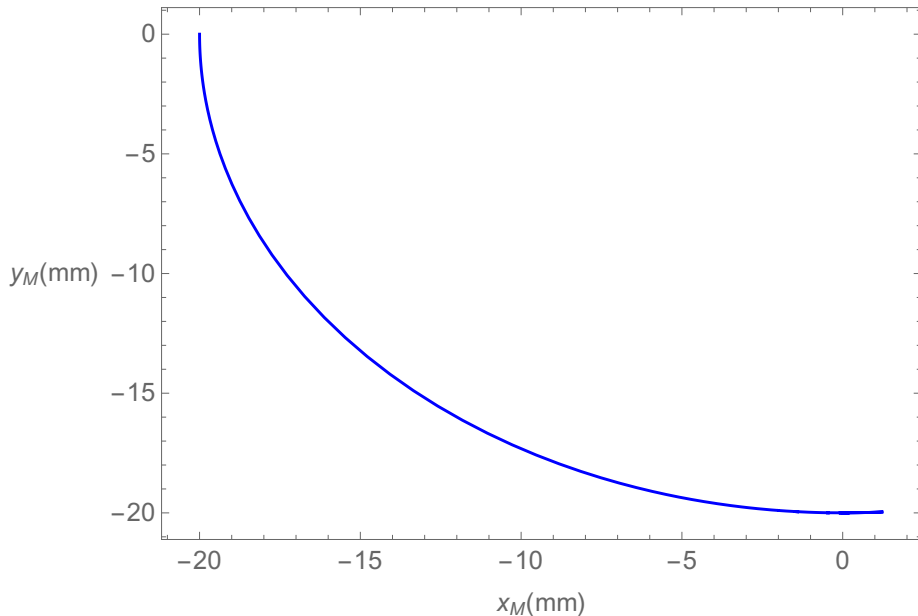


Figure 2.18: Trajectory of the point mass  $M$  when  $\alpha = 0$  and  $\beta(0) = -\frac{\pi}{2}$  for a simple pendulum with non-parallel axes.

The results shown in Figure 2.19 depict the variation of  $\dot{\beta}_{RMS}$  as we vary the initial condition  $\beta(0)$ . Two peaks are observed corresponding to the values of initial condition  $\beta(0) = 0.23 \times 2\pi$  and  $\beta(0) = 0.77 \times 2\pi$ . On the other hand, the maximum reached value is very low when compared to the RMS value obtained for the single pendulum design.

Is also interesting to vary the design parameter  $\alpha$ , and look at the maximization of the RMS value  $\dot{\beta}_{RMS}$ . We compute this variation and plot the results in Figure 2.20. It is shown that a maximum RMS value is obtained for  $\alpha = 0.23 \times 2\pi$ .

Next, we vary both angular position  $\alpha$  and  $\beta(0)$  in order to detect the positions that maximize the value of  $\dot{\beta}_{RMS}$ . This is shown in Figure 2.21. We remark that the maximum

value is 0.6175 obtained for example for  $\alpha = 0.25 \times 2\pi$  and  $\beta(0) = 0$ .

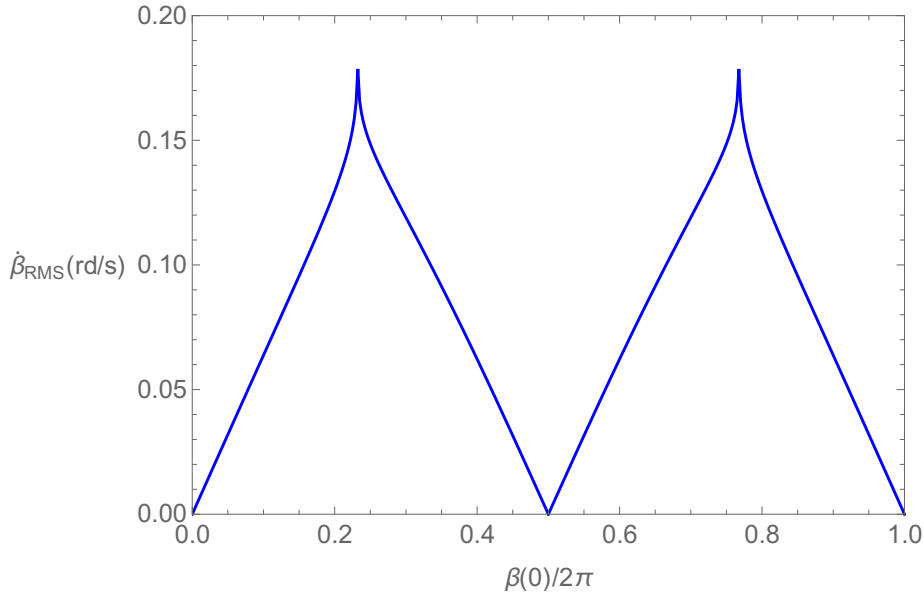


Figure 2.19: RMS values of the angular velocity  $\dot{\beta}_{RMS}$  for a damping coefficient  $c = 0.01$  and different initial conditions  $\beta(0)$  for a simple pendulum with non-parallel axis when  $\alpha = 0$ .

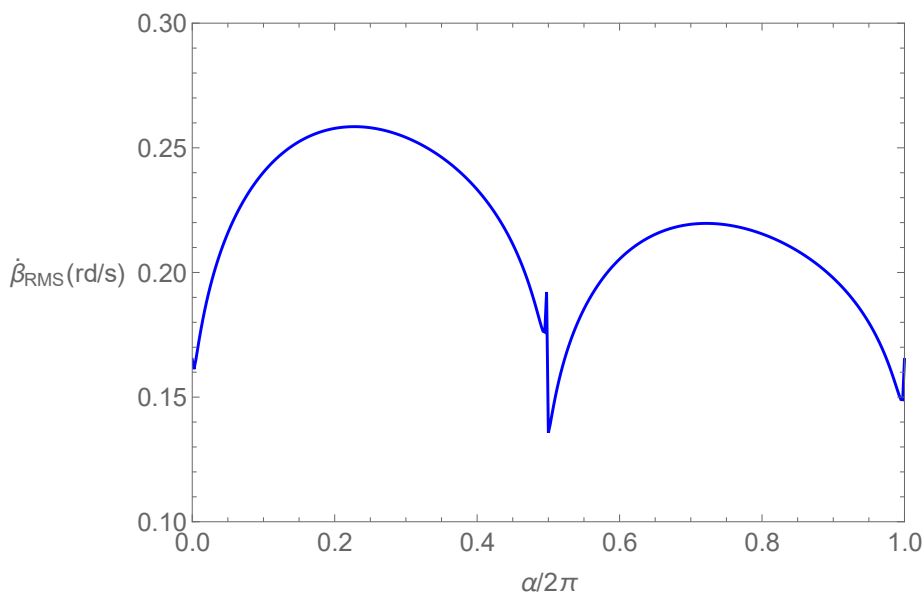


Figure 2.20: RMS values of the angular velocity  $\dot{\beta}_{RMS}$  for a damping coefficient  $c = 0.01$  and different initial conditions  $\alpha$  for a simple pendulum with non-parallel axis when  $\beta(0) = \pi/2$ .

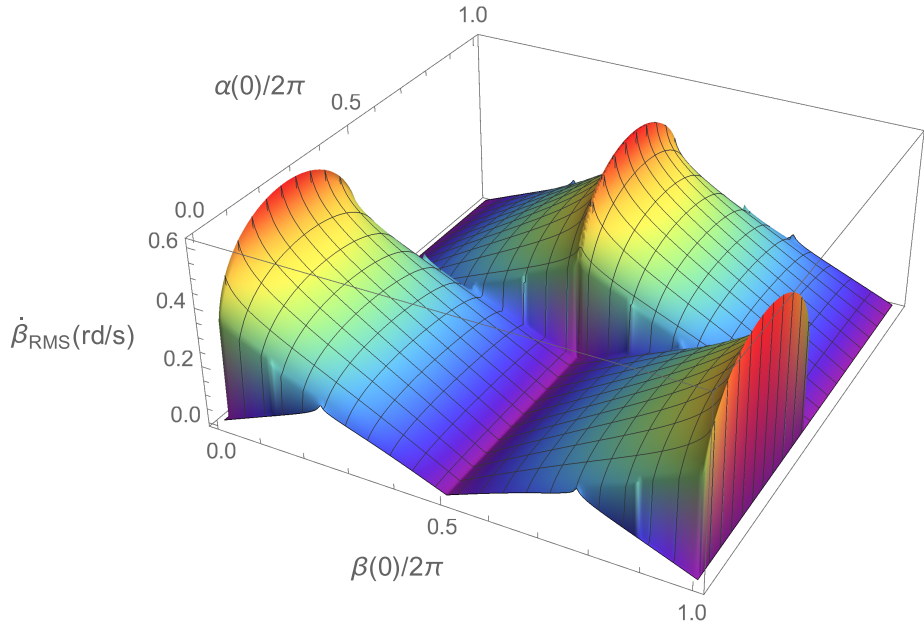


Figure 2.21: 3D view of the RMS values of the angular velocity  $\dot{\beta}_{RMS}$  for a damping coefficient  $c = 0.01$  and different initial conditions  $\beta(0)$  and  $\alpha$  for a simple pendulum with non-parallel axis.

### 2.3.4 TIME RESPONSE OF THE ROTT'S PENDULUM WITH PARALLEL AXIS

The last proposed design is the Rott's pendulum, where two degree of freedom should be solved. It is described by Figure 2.5. We analyze the time response of the system where we suppose that the transducer is located at the axis  $(A, \vec{z}_0)$ . Therefore the damping coefficient  $c_2 = 0.0001$  is fixed for all simulations. The initial conditions are  $\alpha = -\frac{\pi}{2}$  and  $\beta(0) = 0$ .

In Figure 2.22, the time response of the angular position  $\alpha(t)$  is shown for a duration of 20s simulation and by keeping the cruising speed to 50km/h. The behavior is similar to the previous cases where the influence of the damping coefficient is clearly restricting the rotations. This is confirmed in Figure 2.23 where the angular velocity  $\dot{\beta}(t)$  variation with respect to the wheel angular position is showed for the several damping coefficients  $c_1$ .

Also, the trajectory of the mass point  $M$  in the frame  $(A, \vec{x}_1, \vec{y}_1, \vec{z}_0)$ , for a damping coefficient  $c = 0.01$ ,  $\alpha(0) = -\frac{\pi}{2}$  and  $\beta(0) = 0$ , is shown in Figure 2.24. The trajectory is oscillating during the transient response due to the presence of the additional degree of freedom.

The RMS value of the angular velocity  $\dot{\alpha}_{RMS}$  is estimated for initial conditions  $\beta(0) = 0$  and by varying  $\alpha(0)$ , when the damping coefficient is fixed to  $c_1 = 0.01$ . The results, shown in Figure 2.25 depicts a maximum value of  $\dot{\alpha}_{RMS}$  at  $\alpha(0) = \pi$ .

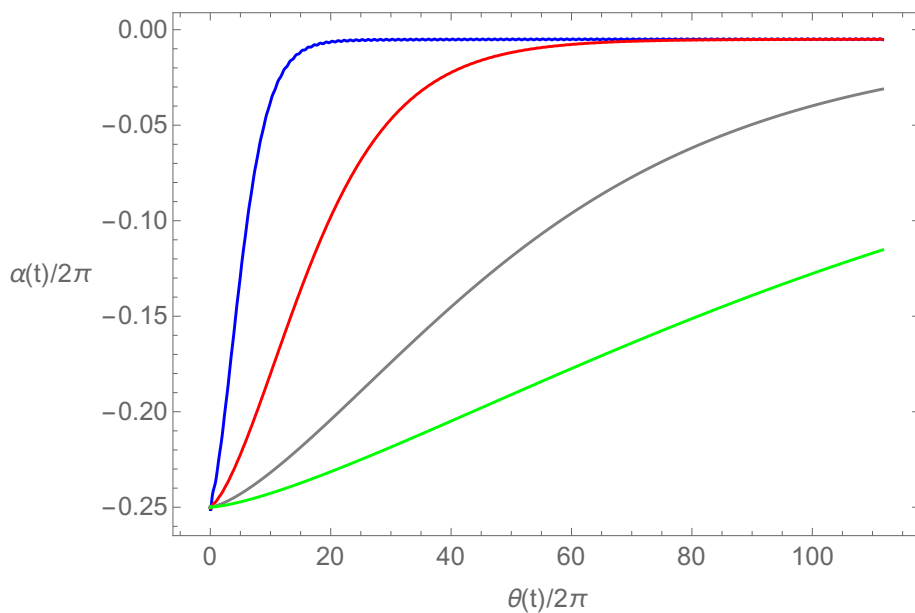


Figure 2.22: Time response of the angular position  $\alpha$  for Rott's pendulum with parallel axis with different damping coefficients (Blue curve  $c_1 = 0.01$ , Red curve  $c_1 = 0.05$ , Grey curve  $c_1 = 0.2$  and Green curve  $c_1 = 0.5$ ,  $c_2 = 0.0001$ ).

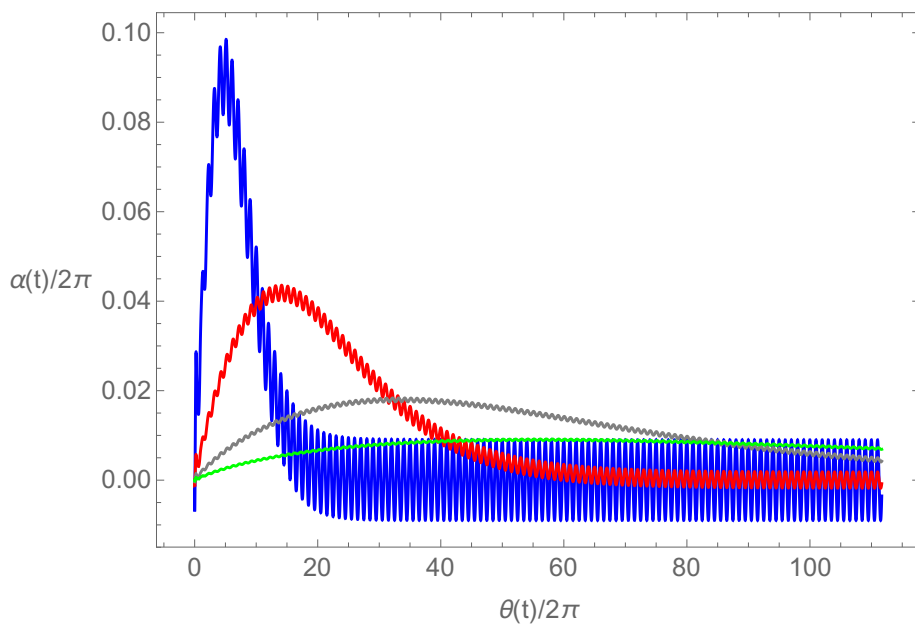


Figure 2.23: Time response of the angular velocity  $\dot{\alpha}$  for Rott's pendulum with parallel axis with different damping coefficients (Blue curve  $c_1 = 0.01$ , Red curve  $c_1 = 0.05$ , Grey curve  $c_1 = 0.2$  and Green curve  $c_1 = 0.5$ ,  $c_2 = 0.0001$ ).

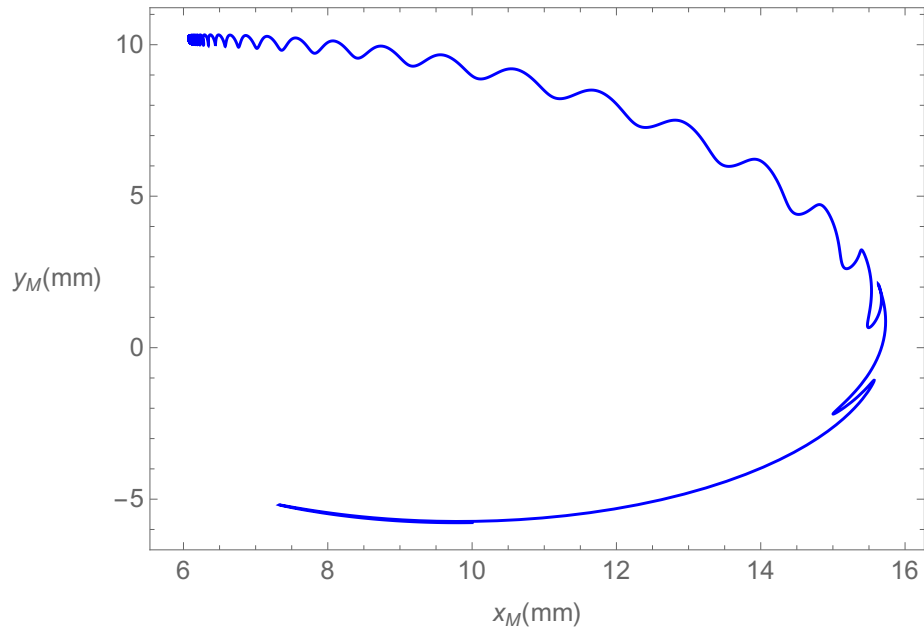


Figure 2.24: Trajectory of the point mass  $M$  when  $\alpha(0) = -\frac{\pi}{2}$  and  $\beta(0) = 0$  for a Rott's pendulum.

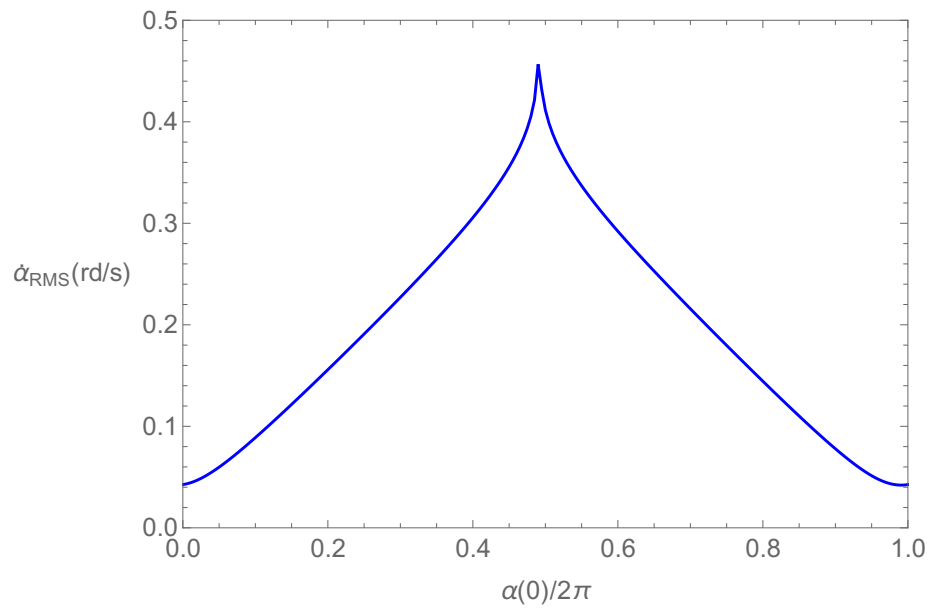


Figure 2.25: RMS values of the angular velocity  $\dot{\alpha}_{RMS}$  for a damping coefficient  $c_1 = 0.01$  and different initial conditions  $\alpha(0)$  for a Rott's pendulum with parallel axis when  $\beta(0) = 0$ .

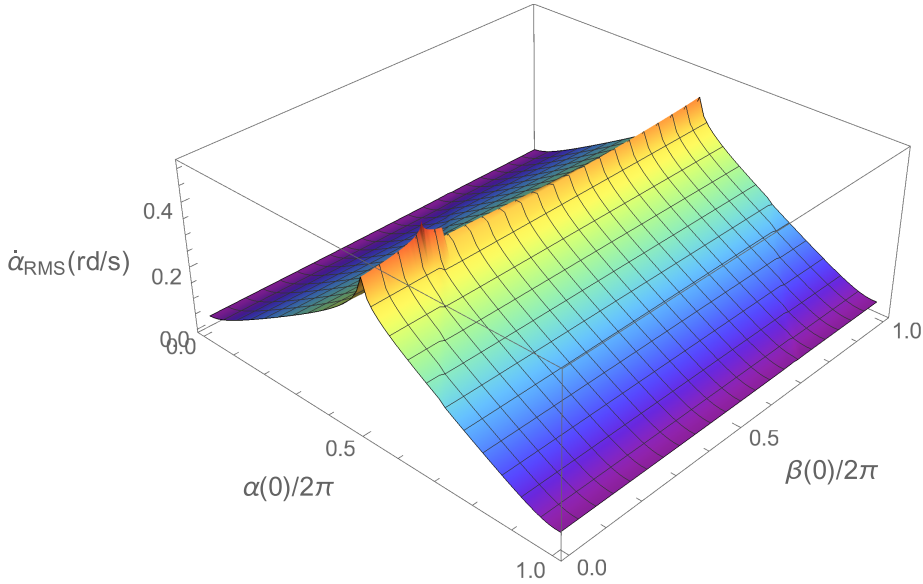


Figure 2.26: 3D view of the RMS values of the angular velocity  $\dot{\alpha}_{RMS}$  for a damping coefficient  $c_1 = 0.01$  and different initial conditions  $\alpha(0)$  and  $\beta(0)$  for a Rott's pendulum with parallel axis.

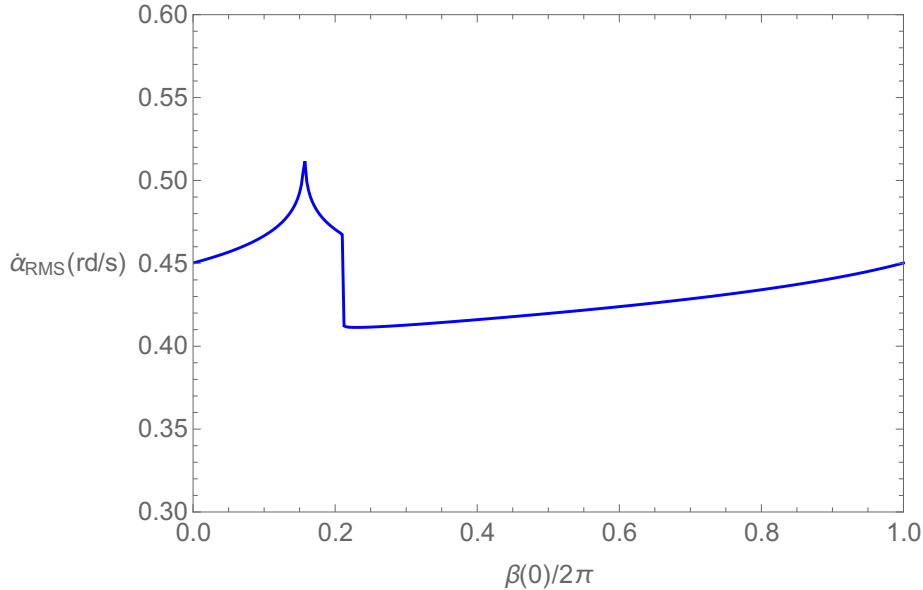


Figure 2.27: RMS values of the angular velocity  $\dot{\alpha}_{RMS}$  for a damping coefficient  $c_1 = 0.01$  and different initial conditions  $\beta(0)$  for a Rott's pendulum with parallel axis when  $\alpha(0) = \pi$ .

Since two degree of freedom are treated in this design, we plot the RMS value of the angular velocity  $\dot{\alpha}_{RMS}$  again when both initial conditions are varied. The 3D plot in Figure 2.26 is showing a maximum RMS value for  $\alpha(0) = \pi$  but for a specific value of  $\beta(0)$ . Fixing the first initial conditions  $\alpha(0) = \pi$  and varying only  $\beta(0)$  gives the exact

variation of the maximum value of  $\dot{\alpha}_{RMS}$ . The values given by Figure 2.27 are showing a maximum value of  $\dot{\alpha}_{RMS} = 0.5159$  at  $\beta(0) = 0.1575 \times 2\pi$ .

## 2.4 RESULTS DISCUSSION

The results simulated in the previous section gives a clear idea about the performances of the different proposed design for a transient behavior. In fact, the transduction mechanism, proposed here is an rotating electromagnetic generator, that produces electrical energy proportionally to the angular speed of its axis. Therefore, the method proposed to compare between the performances of the different proposed designs is to calculate an RMS value of the angular velocity of the concerned degree of freedom and compare the outcomes. The RMS depends on the initial conditions  $\alpha(0)$  and  $\beta(0)$ . In Table 2.5 we summarize the RMS values obtained for different designs and their corresponding initial conditions.

The simple pendulum with parallel axes presents the maximum RMS value. This can be explicated by the fact that we consider a damping coefficient in each degree of freedom. The simple pendulum, as a single degree of freedom system gives best results. Results show also that the double pendulum gave a better RMS value than the Rott's pendulum.

Table 2.5: RMS maximum achievable values of the transducer's angular speed for the different proposed designs.

Design Axes	Single with //	Double with //	Single with non //	Rott with //
$\dot{\alpha}_{RMS}$	0.6495	0.6149	0.6175	0.5159
Initial conditions	$\alpha(0) = \pi$ -	$\alpha(0) = \pi$ $\beta(0) = 0.8 \times 2\pi$	$\alpha = 0.25 \times 2\pi$ $\beta(0) = 0$	$\alpha(0) = \pi$ $\beta(0) = 0.16 \times 2\pi$

## 2.5 CONCLUSION

In this chapter, we presented four pendulum designs considered as mounted in a rotating wheel. The equation of motion of each design in transient behavior were derived. Next, the time response of the angular position and angular velocity were calculated for different damping coefficients.

The trajectory of the point mass of each pendulum were also calculated in addition of the RMS value of the angular velocity for different initial conditions.

We notice that the RMS value depends on the initial conditions and it reaches its highest value for a simple pendulum with parallel axis when  $\alpha(0) = \pi$ .



# 3

## EXPERIMENTAL SETUP AND RESULTS

### 3.1 INTRODUCTION

In this chapter, we will put into experiment three pendulum designs: simple pendulum, double pendulum and Rott's pendulum. We start by characterizing the electromagnetic generator in which the pendulums will be linked.

As a first step, we derive the governing equation of the generator to get the torque developed at the generator's shaft and the generated power. Then we look at the optimum load resistance by measuring the higher power from generated voltage and current.

Then, we will proceed to the setup and characterization of each pendulum. We use a test bench setup to reproduce the behavior of the pendulum mounted into a rotating disk. Steady-state and transient behaviors will be tested and the output voltage will be measured at each case.

### 3.2 CHARACTERIZATION OF THE ELECTROMAGNETIC GENERATOR

#### 3.2.1 PRESENTATION OF THE GENERATOR

As a first step to present the proposed experimental setup, we introduce the chosen electromagnetic generator. It is a high performance brushed DC motor with high torque output "Portescap 16N78 Athlonix" with precious metal commutation with a coreless structure. The proposed generator can reach up to 80% efficiency. The ironless construction of the motor reduces significantly its weight, while the used neodymium

magnet increase its performance [103]. In motor mode, it can deliver a torque up to 6 mNm continuously. In Table 3.1 we present the characteristics of the Portescap DC motor given by the supplier. In the next part we will verify some of these characteristics that will be useful in our experimental analysis.

Table 3.1: Characteristics of 16N78 Athlonix DC motor as given by Portescap [103].

Parameter	Value	Unit
Nominal Voltage	24	Volt
No-Load Speed	8,200	rpm
No-Load Current	4.0	mA
Internal Resistance	60.5	$\Omega$
Output Power	4.9	W
Stall Torque	11	mNm
Efficiency	81	%
Max continuous speed	10,000	rpm
Max continuous torque	6.3	mNm
Max continuous current	0.23	A
Back-EMF Constant	2.90	mV/rpm
Torque Constant	27.70	mNm/A
Motor Regulation	78.85	103/Nms
Friction Torque	0.08	mNm
Rotor Inductance	2.40	mH
Mechanical Time Constant	9.3	ms
Rotor Inertia	1.18	$\text{g} \times \text{cm}^2$
Thermal Resistance (rotor/body)	6/25	$^{\circ}\text{C}/\text{W}$
Thermal Time Constant (rotor/stator)	12/250	$^{\circ}\text{C}/\text{W}$
Operating Temperature Range:	-30 to 85	$^{\circ}\text{C}$
Shaft Load max.: (5mm from bearing)	With sleeve bearings 1.5 (radial) 100 (axial)	N N
Shaft play:	<0.03 (radial) 0.15 (axial)	mm mm
Weight	24	g

### 3.2.2 CHARACTERIZATION ASSEMBLY

To characterize the Portescap DC motor in generator mode, we couple two motors by connecting the shafts through an elastic link (see Figure 3.1). The first DC motor will be used as the drive motor and it will rotate the second motor which will be considered as the generator.

The characterization assembly is wired as follows: first the drive motor is linked to voltage generator to control its rotation speed  $\omega_m$ . The input voltage  $U_i$  and current  $I_i$  are measured at the drive motor connectors (Figure 3.2). The output connectors of the generator are first linked to a variable resistance decade box that will allow the variation of the resistance load, then, the output voltage  $U_o$  is measured across this resistance load and the output current  $I_o$  is the one crossing it (Figure 3.2). The output speed of the drive motor is measured by an optical tachometer. A reflective tape is used to mark each rotation of the shaft. The setup of the characterization assembly is presented in Figure 3.3.

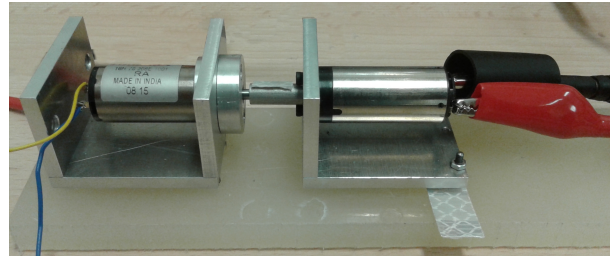


Figure 3.1: Coupled Motors

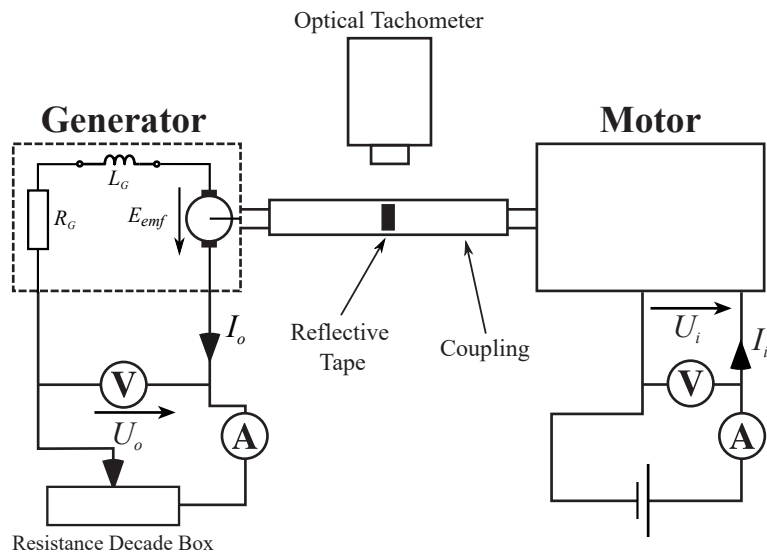


Figure 3.2: Modeling of the characterization assembly of the generator

The objective of the characterization assembly, presented here, is to characterize the generator by measuring the electromechanical coupling coefficient relating the rotation speed to electromotive force known as the EMF-constant  $K_E$  and the torque constant  $K_T$ , relating the generated current to the applied torque.

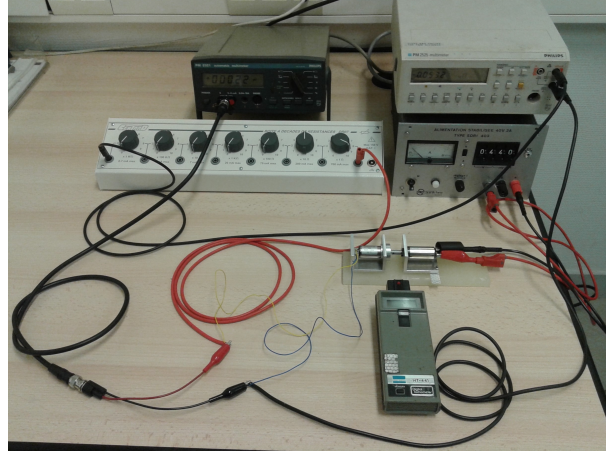


Figure 3.3: Experimental setup of the characterization assembly of the generator

The proposed characterization assembly of the generator is modeled by the following differential equation derived using the Kirchhoff's voltage law (mesh rule):

$$(R + R_G)I_o + L_G \frac{dI_o}{dt} - E_{emf} = 0 \quad (3.1)$$

where  $R$  is the value of the variable load resistance,  $R_G$  is the internal resistance of the generator,  $I_o$  is the generated current,  $L_G$  is the generator inductance and  $E_{emf}$  is the electromotive force of the generator.

The proposed generator is a permanent magnet DC motor, it is rotating at constant speed thanks to the drive motor fed at constant voltage  $U_i$ . As a result, the electrical current flowing through the electrical circuit of the generator  $I_o$  is constant (Figure 3.2). The Equation (3.1) becomes

$$(R + R_G)I_o - E_{emf} = 0 \quad (3.2)$$

We use the Ohm's law across the resistance load  $R$ , where the output voltage is  $U_o$ , that is

$$U_o = R I_o \quad (3.3)$$

Therefor, Equation (3.2) becomes

$$(R + R_G) \frac{U_o}{R} - E_{emf} = 0 \quad (3.4)$$

The electromotive force of the generator is deduced by

$$E_{emf} = \left(1 + \frac{R_G}{R}\right) U_o \quad (3.5)$$

On the other hand we adopt the classical electromechanical coupling equations for permanent magnet DC motors [104] given by

$$E_{emf} = K_E \omega_m \quad (3.6)$$

$$T_m = K_T I_o \quad (3.7)$$

where the rotation speed  $\omega_m$  and the torque  $T_m$  are both transmitted by the drive motor.  $K_E$  is the EMF-constant and  $K_T$  is the torque constant. Therefore, we deduce from Equation 3.4 that

$$K_E = \left(1 + \frac{R_G}{R}\right) \frac{U_o}{\omega_m} = \left(1 + \frac{R_G}{R}\right) K_\omega \quad (3.8)$$

where  $K_\omega = \frac{U_o}{\omega_m}$  is a constant ratio factor if the resistance load  $R$  is fixed. It will be identified latter in the experimental characterization of the generator.

The input power for the generator is  $P_{in} = T_m \omega_m$ , while the generated power is  $P = U_o I_o$ , which is the power dissipated in the resistance load. Therefore the electrical efficiency  $\eta$  of the generator can be defined by letting

$$P = \eta P_{in} \quad (3.9)$$

If we consider Equations (3.3), (3.7) and (3.9), we can estimate the torque constant by

$$K_T = \frac{K_\omega}{\eta} \quad (3.10)$$

As a result, we deduce the torque as a function of the rotation speed as follows:

$$T_m = K_T I_o = K_\omega \frac{U_o}{\eta R} = \frac{K_\omega^2}{\eta R} \omega_m \quad (3.11)$$

The torque developed at the generator's shaft is proportional to the rotation speed of the shaft. Also we can calculate the proportionality between the generated electrical power and rotation speed since this later will be induced by the pendulum in motion. Using the same equations we deduce that

$$P = \eta P_{in} = \eta T_m \omega_m = \frac{K_\omega^2}{R} \omega_m^2 \quad (3.12)$$

The generated power is proportional to the square of the rotation speed. This result will be confirmed in the following characterization section.

### 3.2.3 EXPERIMENTAL CHARACTERIZATION RESULTS

The generator is supposed to transduce mechanical energy to electrical power under certain working conditions. In this work, without loosing the generality of the approach, we are supposing that the load circuit can be modeled as purely resistive. However, the efficiency of the transduction is highly dependent on the impedance matching between the mechanical and electrical domains of the generator. For this reason we will try first to determine the optimal resistance load  $R_{opt}$  that allow maximum conversion of the mechanical work into electrical power. Is is worth noting here that the internal resistance of the generator was measured at  $R_G = 63.4\Omega$ .

For a fixed rotation speed  $\omega_m$ , we measure  $U_o$  and  $I_o$  for different values of the load resistance  $R$ , then we calculate the generated electrical power by assuming that it is equal to the electrical power dissipated into the resistance load.

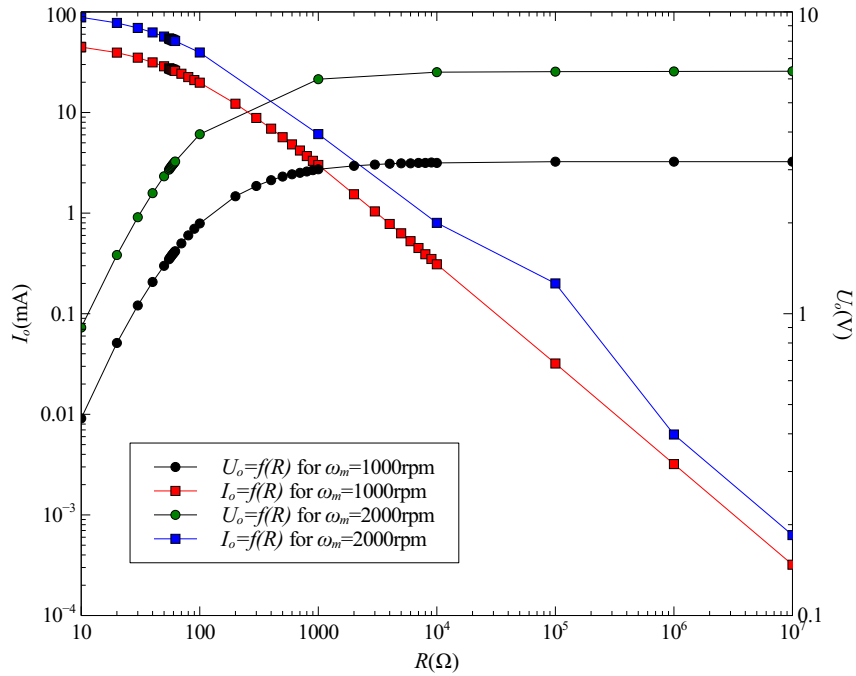


Figure 3.4: Variation of  $U_o$ ,  $I_o$  as a function of  $R$  for different rotation speeds

In the Figure 3.4, we plot the curves of  $I_o$  and  $U_o$  for a load resistance  $R$  varying from  $10$  to  $10^7\Omega$ , for  $\omega_m = 1000\text{rpm}$  and  $\omega_m = 2000\text{rpm}$ . We notice that  $I_o$  decreases when  $R$  increases. In the other hand,  $U_o$  increases when  $R$  increases until it reaches a saturation level. The same shapes are observed for different rotation speeds.

Plotting the curve of the transduced power  $P$  as  $R$  is varied in the Figure 3.5 for different rotation speeds, we notice that  $P$  reaches its optimum value for the same value

of  $R$ . Therefore, we conclude that the optimum load resistance for the proposed generator is  $R_{opt}=59\Omega$ .

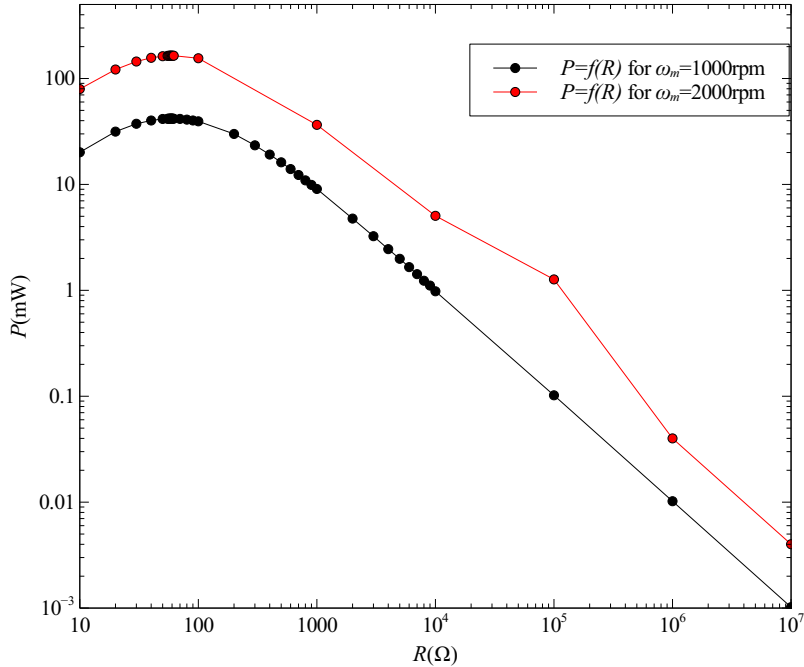


Figure 3.5: Variation of  $P$  as a function of  $R$  for different rotation speeds

At optimal load resistance, we plot in Figure 3.6 the output voltage  $U_o$ , and current  $I_o$  versus the rotation speed  $\omega_m$ . We notice that  $U_o$  has a linear variation with the rotation speed  $\omega_m$ . We deduce that the slope in Figure 3.6 can be identified with the ratio factor  $K_\omega = \frac{U_o}{\omega_m} = 1.576 \times 10^{-3} \text{ V/rpm} = 14.99 \text{ mV}\times\text{s}$ .

The relation relating the applied torque by the drive motor and the rotation speed, given by Equation (3.11) is used to derive the equation of motion of the pendulum. It states that the torque at the generator is proportional to the rotation speed which appear as a damping term in the pendulum equation of motion as used in the previous chapter.

The generated electrical power  $P$  and the torque developed at the generator's shaft  $T_m$  are measured as we increase the rotation speed of the drive motor when optimal resistance is used. The plot shown in Figure 3.7 shows a net increase of the power as the rotation speed increases. The output power is fitted to the function  $f(\omega_m) = 4.16 \times 10^{-5} \omega_m^2$  in Figure 3.7. This result confirms the one deduced in Equation 3.12 that the generated power is proportional to the square of the rotation speed.

Furthermore, the plot shows that the torque is proportional to the rotation speed as demonstrated in Equation 3.11.

## EXPERIMENTAL SETUP AND RESULTS

---

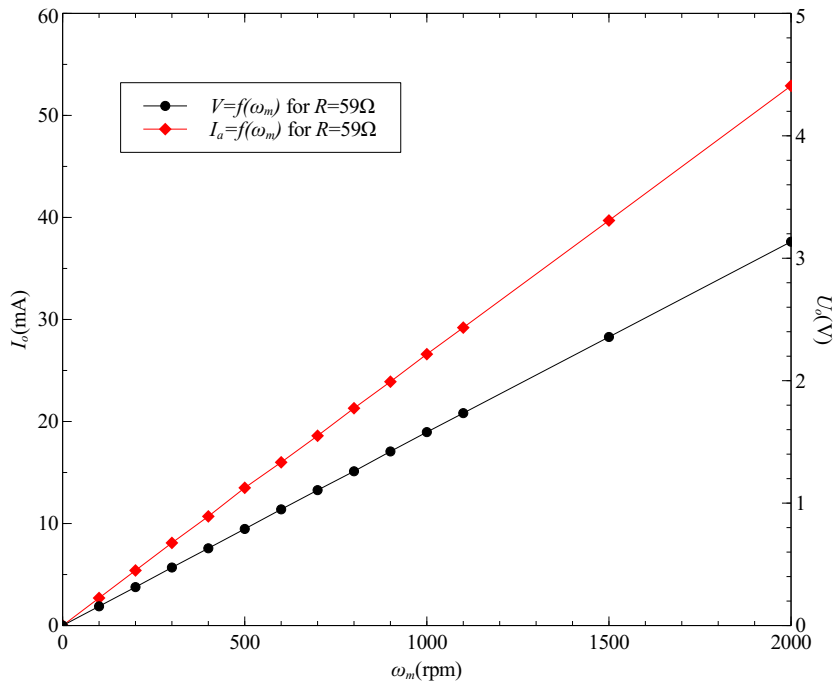


Figure 3.6: Variation of  $U_o$  and  $I_o$  as a function of  $\omega_m$  at  $R_{opt} = 59\Omega$

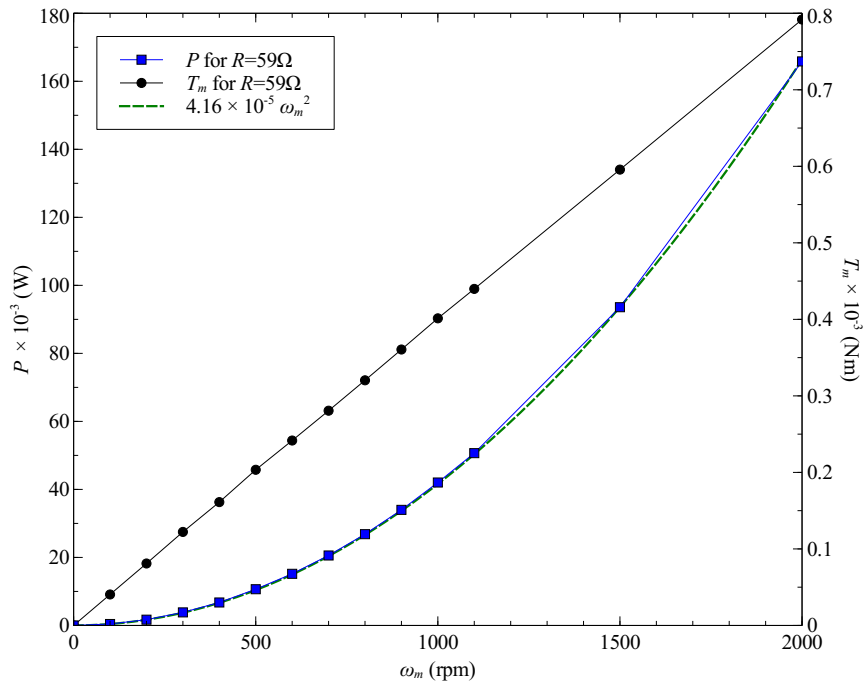


Figure 3.7: Variation of  $P$  and  $T_m$  as a function of  $\omega_m$  at  $R_{opt} = 59\Omega$

### 3.3 CHARACTERIZATION OF PENDULUMS

#### 3.3.1 PRESENTATION OF PENDULUMS

In this section, we will characterize three types of pendulums selected to be used in this thesis: the simple pendulum, the double pendulum and the Rott's pendulum. The non-parallel axis pendulum is dropped for fabrication difficulty reasons. The choice of the dimensions of the pendulums is related to the availability of fabrication facilities in FEMTO-ST applied mechanics department. Nevertheless, we tried to minimize the dimensions of the pendulum, in general, to be consistent with their field of application in the TPMS context. Steel was chosen as a material for the fabrication of all pendulums.

#### 3.3.2 SETUP OF THE STUDIED PENDULUMS

The three pendulums are fabricated using classical fabrication techniques such as milling and turning. The revolute joint are realized using deep groove double ball-bearings used as open bearings (without seals or shields) in order to reduce damping.

The pendulums are mounted into an aluminum support (Figure 3.8), where a double roll bearing is mounted to link the different pendulums to be tested with the generator.

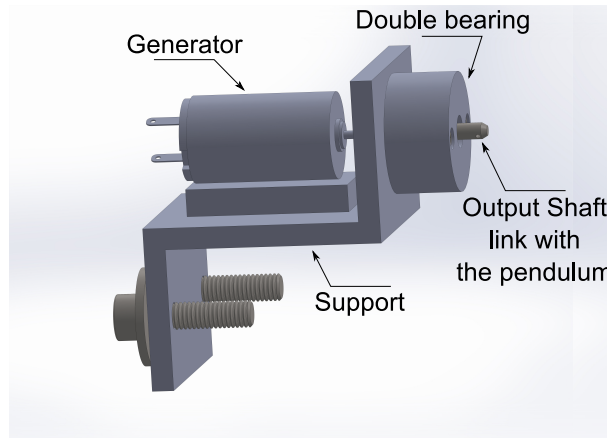


Figure 3.8: Setup of the studied pendulums

To measure the natural frequencies of each pendulum, we use a laser vibrometer Polytec PDV100 directed toward the movable parts that needs to be characterized. The natural frequencies will also depend on the inertial characteristics of the generator and the electrical load attached to it. Thus, resonance frequencies of the pendulum were measured

for two cases: first when we put the electrical load resistance at  $R_{opt}$ , and the second when we don't take any load resistance into consideration, i.e. at open circuit conditions.

### 3.3.2.1 SIMPLE PENDULUM

For the simple pendulum it is made of a steel rod with rectangular cross-section and total dimensions  $47 \times 13 \times 4$ mm. The rod is mounted on the output shaft linked to the generator, see Figure 3.9.

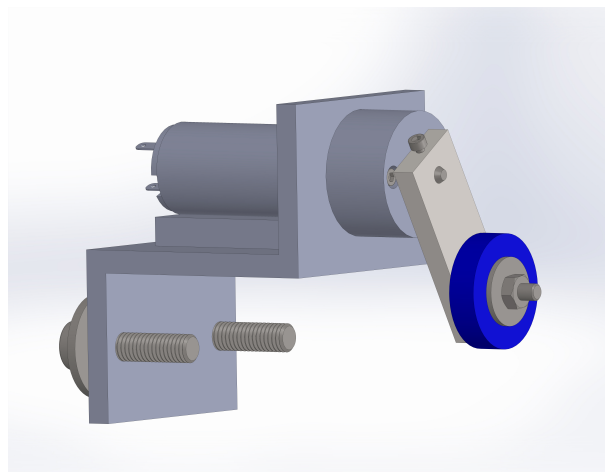


Figure 3.9: Setup of the SP

To measure the natural frequency of the single pendulum, we made a free release of the rod with initial position, then we measured its oscillation frequency using a laser vibrometer oriented to the rod tip.

In the ideal case, the added tip mass do not changes the resonance frequency if its moment of inertia is negligible. However, in our case, the mass is distributed and due to the relatively small dimensions of the system, linking an additional mass to the rod changes the natural frequency of the pendulum. So we consider three cases: first, when no mass is attached to the rod, second when two different masses are attached to the rod.

The Table 3.2 presents the resonance frequencies of the simple pendulum with different values of the tip mass. The generator is connected in all cases to the optimal electrical resistance load. As seen in Table 3.2, the natural frequency of the simple pendulum is reduced by increasing the value of the tip mass.

Table 3.2: Simple pendulum measured resonance frequencies

	Frequency (Hz)
without mass	2.57
with mass 1 (6.577g)	2.50
with mass 2 (12.440g)	2.49

### 3.3.2.2 DOUBLE PENDULUM

The double pendulum considered in this case of study, is composed of two rods of the same length (Figure 3.10). Each rod is also equal in length to the one used in the simple pendulum case. The rods are linked through a pivot joint bearings that ensure the rotation function. In this case the double pendulum is a 2 DOF system with two natural frequencies.

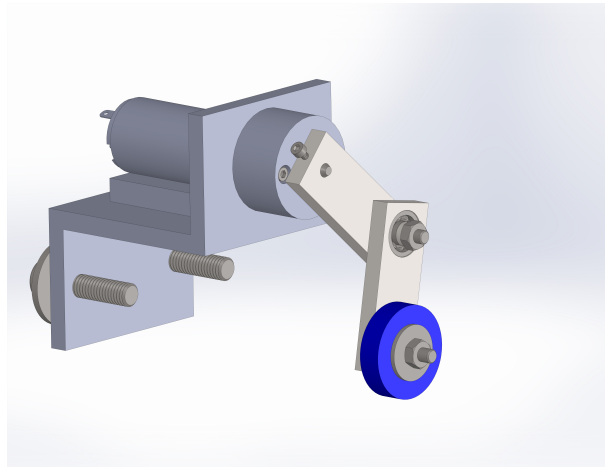


Figure 3.10: Setup of the DP

It turns out that the resonance frequency of the rod mounted on the shaft of the generator will be the same as the simple pendulum presented in Table 3.2. Yet, we have to measure the resonance frequency of the second rod which is attached to the first one. The values of the natural frequency is measured using a laser vibrometer. They are given in Table 3.3 where different tip masses are attached to the second rod. In this case an electrical optimal load resistance have been used. As denoted in the case of the simple pendulum, the natural frequency decreases as the value of the tip mass increase.

Table 3.3: Measured second rod double pendulum natural frequency

	Frequency (Hz)
Without mass	2.93
With mass 1 (6.577g)	2.7
With mass 2 (12.440g)	2.69

### 3.3.2.3 ROTT'S PENDULUM

As specified in the previous chapter, a Rott's pendulum is a 2 DOF pendulum in which the natural frequency ratio between each of its DOF is equals to 2. This particular frequency ratio induce a two-to-one internal resonance with a principal parametric resonance [96]. The design is inspired by the one proposed by Rott in 1970 [93].

Particularly in the proposed design we tried to be consistent with the previous cases. As demonstrated in the preceding sections, the designed small scale system is very sensitive to the geometry of the pendulum. Several attempts were required to finally get the right masses to be used in order to get the right frequency ratio.

Assuming that Rod 1 is the L-rod mounted to the shaft of the generator and Rod 2 is the one mounted into Rod 1. According to Rott [93], the frequencies that should have a ratio equal to 2 are those related to the natural frequency of Rod 2 and the other one should be the natural frequency of Rod 1 in which the total mass of Rod 2 is linked to the second pivot location as a concentrated mass. The proposed design of the Rott pendulum is shown in Figure 3.11.

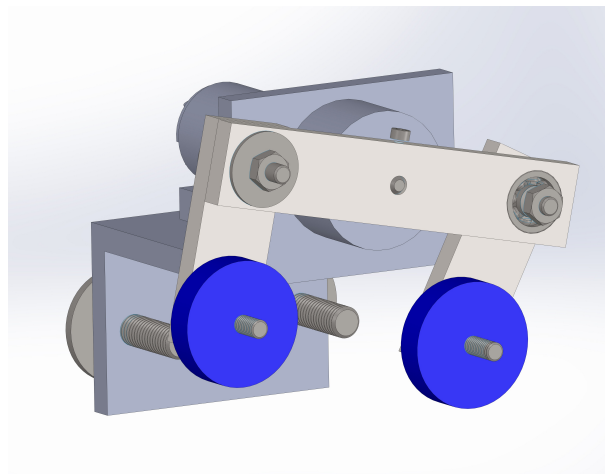


Figure 3.11: Setup of the RP

We measured the resonance frequency of Rod 1 and Rod 2 apart. In fact, we first

measured the natural frequency of Rod 1 by attaching a circular mass at the pivot location (see Figure 3.12). A laser vibrometer is used to detect the natural frequency of Rod 1.

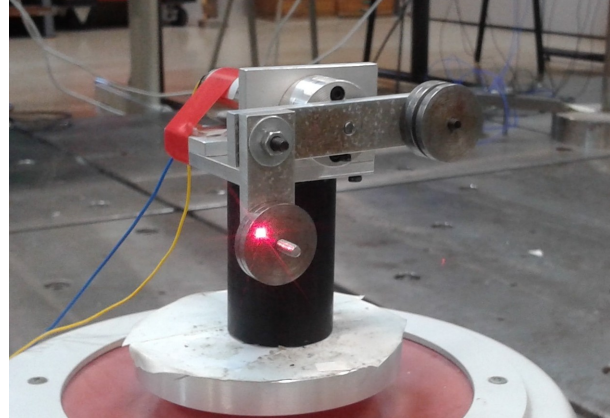


Figure 3.12: Measuring the Resonance Frequency of Rod 1

For Rod 2, we hold Rod 1 fixed to the base and initiate a free motion of Rod 2. The natural frequency is also measured here using a laser vibrometer (see Figure 3.13). In the table 3.4, we put the natural frequencies the Rott's pendulum for the optimal load resistance.

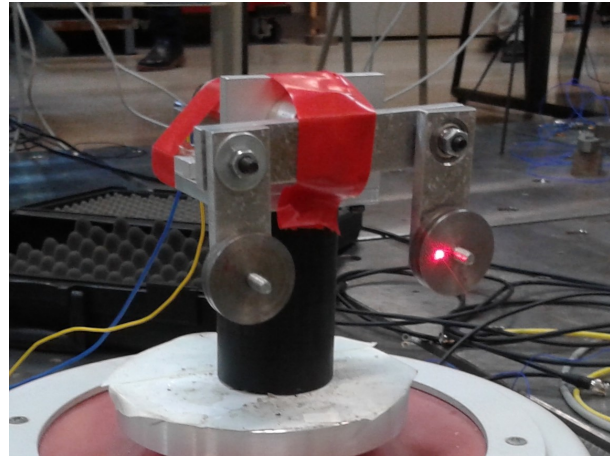


Figure 3.13: Measuring the Resonance Frequency of Rod 2

Table 3.4: Rott's pendulum measured resonance frequencies with  $R_{opt}$

Frequency (Hz)	
Rod 1	1.48
Rod 2	2.94

### 3.4 TEST BENCH

In this section, we expose the proposed design of the test bench that emulate the behavior of the wheel in order to put the pendulum in conditions that are similar to real case wheel's car. The main idea behind this design is to simulate the rotation of the car's wheel and more specifically its rim, in which our pendulums are attached.

Most of the commercial personal vehicles are equipped with 15" (381mm) or 16" (406mm) rims. In our work, we put into rotation a disk which is assimilated to a rim, presented in Figure 3.14. The disk made of Polyoxymethylene (POM), is characterized by its high strength and light weight. It is equipped with large grooves allowing to mount the generator in several positions and radii.

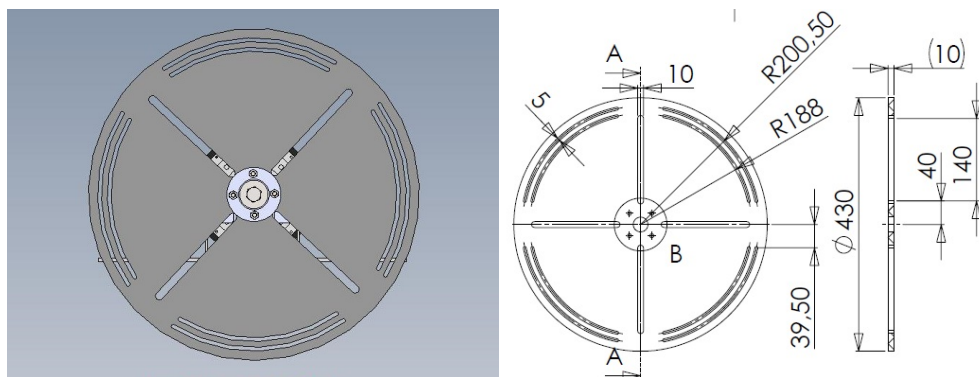


Figure 3.14: Rotating disk of Test Bench

Several rotation speeds and rotation regimes (accelerations and decelerations) needs to be tested. Therefore, a total control of the speed is offered in the proposed design. Also, since the main objective of this work is to estimate the electrical energy that can be harvested by the proposed systems, we also need to measure the generated voltage at the rotating pendulum. A slip ring brush system is used to connect the rotating wires to the acquisition unit.

The whole test bench is presented in Figure 3.15. The nomenclature of the test bench is presented hereafter: 1-Electric motor, 2-Rotating shaft, 3-Plain bearings, 4-Mount for two slip ring brush holders, 5-Hub, 6-Universal joints, 7-Spacer ring, 8-Slip ring (HBM SK5), 9-Disk.

The speed variation of the motor is ensured by a variable speed drive (Leroy Somer Digidrive SK) which is controlled by PC via a DAS (Data Acquisition System, DSP siglab 20-42). The DAS offers several input functions to be interpreted by the variable speed

drive as variable speed instruction. Several functions were used in our case to simulate different scenarii. The entire set up is shown in Figures 3.16 and 3.17.

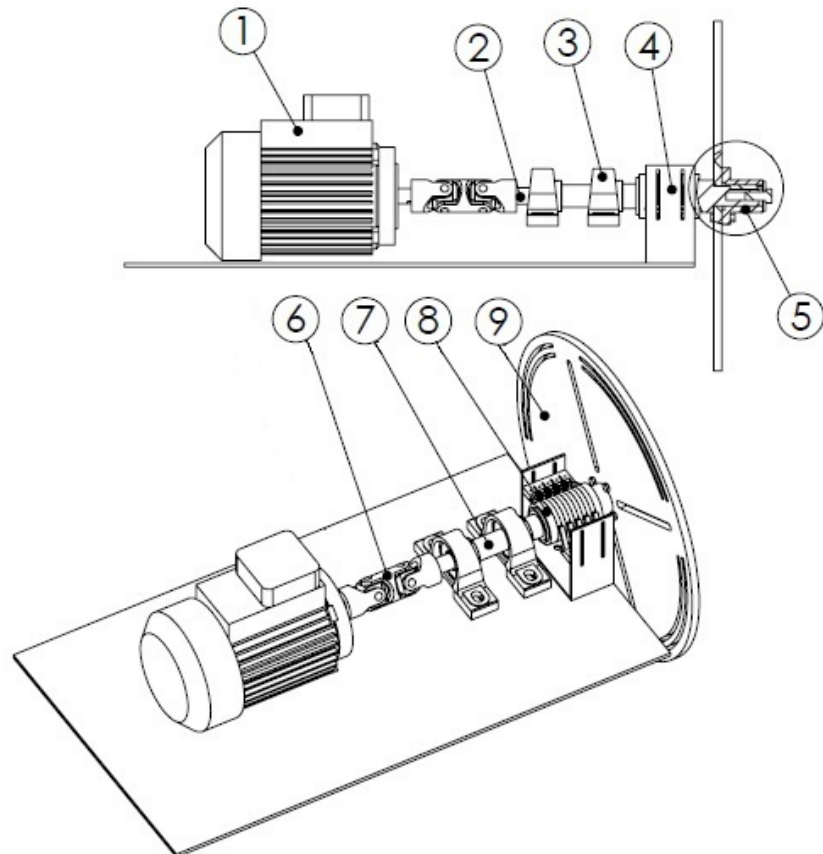


Figure 3.15: Layout of the Test Bench

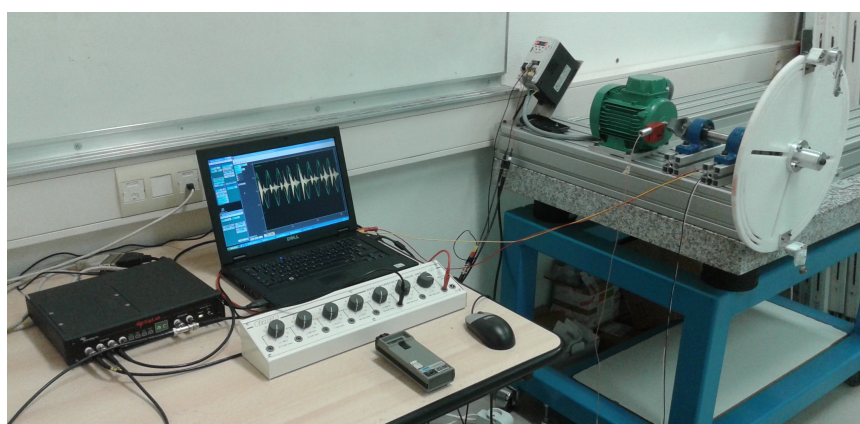


Figure 3.16: Test Bench Realized and DAS

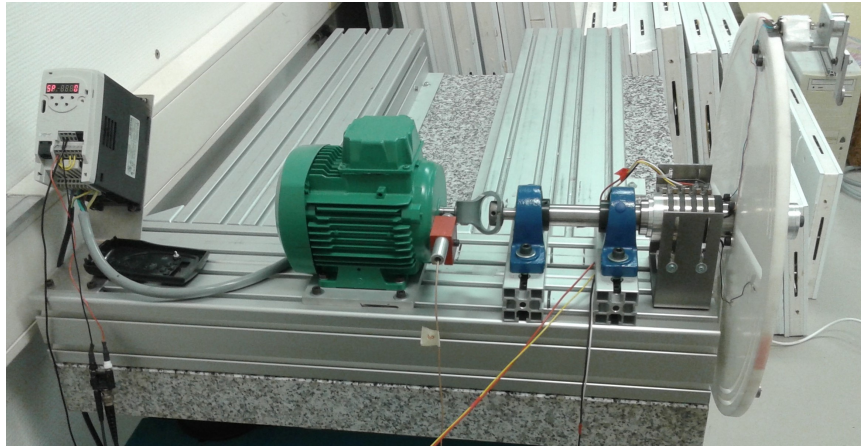


Figure 3.17: Details of the control system of the rotating disk

### 3.5 EXPERIMENTAL RESULTS AND VALIDATION

In this section we will put into experience, the three different pendulums studied in the previous chapters and verify experimentally their performances. Each pendulum is mounted to the support and linked to the generator. The support is fixed to the rotating disk which is actuated by the test bench.

Two approaches can be treated here: the transient and the steady state regimes. In fact, energy can be harvested in both regimes, depending on the kind of vehicle intended to be equipped, one or the other can be dominant. Practically, for the case at hand in the test bench, the analyzed regime is depending on the chosen input function at the DAS level to rotate the disk, one of these regimes will be treated. For example, for constant functions, the response of the disk will be a constant speed rotation and a steady state response is quickly achieved, especially for the simple pendulum. On the other hand, if a periodic function is assumed to be the input, the transient behavior of the pendulum will be dominant.

In all cases, the generator is connected to the DAS, through the slip ring, to measure the electrical response generated by each type of pendulum.

The car wheel taken in our case of study has dimensions 195/65 R15. The external diameter of the tire is 620mm. As presented in chapter 3, we consider that the vehicle reaches a speed equals to 50km/h, this means that the angular velocity is equal to 418rpm. Thus in our test bench, the speed variation will be taken from 0 to 418rpm. The electrical resistance load is fixed at its optimal value  $R=R_{opt}=59\Omega$ .

### 3.5.1 TEST AT CONSTANT ANGULAR ROTATION OF THE RIM

In this section we will plot the solution of the steady-state behavior, generated at constant angular velocity for different rotation speeds, of each studied pendulum. The voltage  $V_{in}$  given by the variable speed drive is transformed to an angular velocity  $\omega$ . For each pendulum, we measure the maximum and minimum peaks generated voltage  $V_{out(max)}$  and the minimum generated voltage  $V_{out(min)}$ . The amplitude of the generated voltage is  $\Delta V_{out} = V_{out(max)} - V_{out(min)}$ .

Depending on the value of the rotation speed  $\omega$ , several observations concerning the behavior of the pendulum can be made. If the pendulum is oscillating around the vertical axis (gravity axis), meaning that the weight force is dominant over the inertial forces. This situation is marked by *SV*. If  $\omega$  is high enough, the centrifugal forces dominate the gravity forces and the pendulum is now oscillating around the radial axis of the rotating disk. This situation is marked by *SR*. Between these two responses a transition behavior is observed where the pendulum is swinging between the *SV* and *SR* solutions. As a result, for the steady state behavior, the response is aperiodic. This situation is marked by *AP*.

#### 3.5.1.1 SIMPLE PENDULUM

In this section, we put into experiment a simple pendulum fixed on the generator with a mass equals to 5.8g mounted at the free tip of the rotating rod.

In Table 3.5 we show measurements loaded for different rotation speeds of the disk. We notice that, for  $\omega$  less than 69.5rpm, the behavior is observed to be at the *SV* type and the amplitude of maximum voltage is proportional to  $\omega$ . For a rotation speed 69.5rpm, the amplitude of generated voltage rises to reach a maximum value equals to 0.64V. The corresponding time depend output voltage is shown in Figure 3.18. For  $\omega$  higher than 70rpm, the simple pendulum oscillates around the radial axis and  $\Delta V_{out}$  falls and continue to decrease when  $\omega$  increases. The behavior is observed to be at the *SR* regime as confirmed by Figure 3.19.

---

## EXPERIMENTAL SETUP AND RESULTS

---

Table 3.5: Generated voltage from simple pendulum for different rotation speeds

$V_{in}$ [V]	0.5	0.75	1	2	3	4	5
$\omega$ [rpm]	30	69.5	105.5	243	366	498	629
$V_{out(max)}$ [V]	0.05	0.36	0.12	5.80E-03	4.45E-03	7.80E-03	7.90E-03
$V_{out(min)}$ [V]	-0.03	-0.28	-0.09	-3.76E-03	-1.36E-03	-1.66E-03	-1.67E-03
$\Delta V_{out}$ [V]	0.08	0.64	0.21	0.00956	0.00581	0.00946	0.00957
Regime type	SV	SV	SR	SR	SR	SR	SR

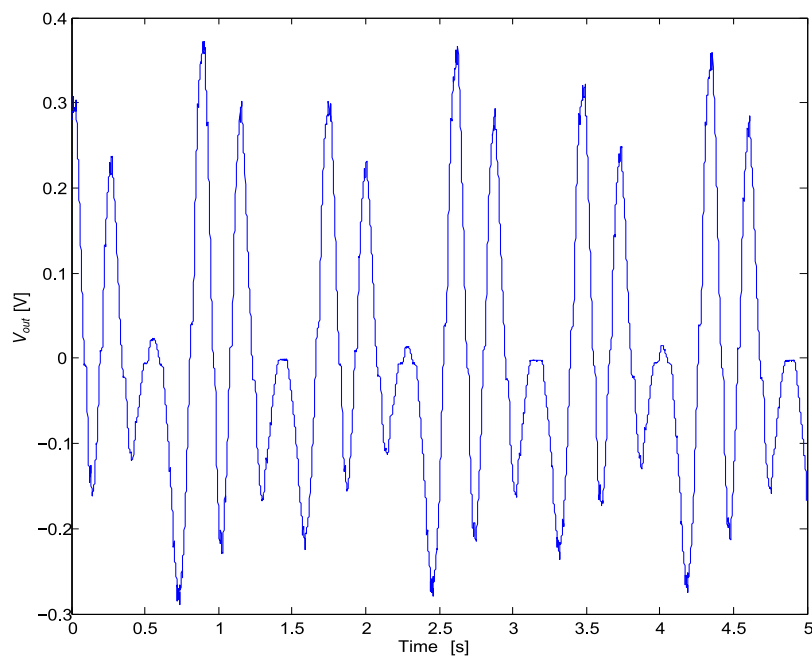


Figure 3.18: Generated voltage from simple pendulum for  $\omega=69.5$ rpm (SV)

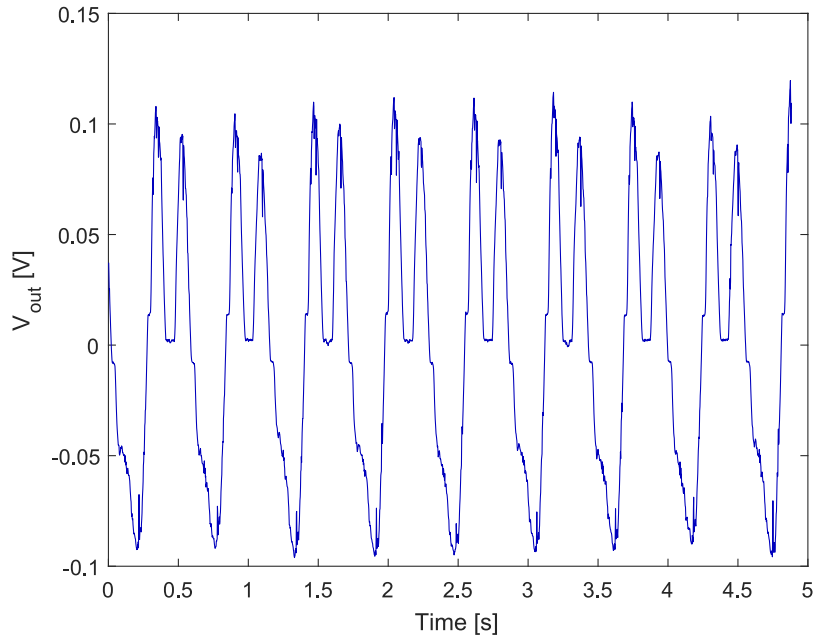


Figure 3.19: Generated voltage from simple pendulum for  $\omega=105.5\text{rpm}$  (SR)

### 3.5.1.2 DOUBLE PENDULUM

For the double pendulum, we put into experiment the device shown in Figure 3.10 with a mass equals to 5.8g mounted on the tip of the free rod. In Table 3.6 we show measurements loaded for different rotation speeds of the disk.

We notice, in Table 3.6, that for  $\omega$  less than 58.5rpm, the double pendulum oscillates around the vertical axis (SV regime) and the amplitude of maximum voltage is proportional to  $\omega$ . For the SV regime, an example is given in Figure 3.20 when  $\omega=54\text{rpm}$ . For a rotation speed going from 58.5rpm to 96rpm, the pendulum is observed to have aperiodic behavior with the AP regime. It is also observed that  $\Delta V_{out}$  increases when  $\omega$  increases to reach a peak equals to 1.5V when  $\omega$  is about 80rpm. An example is given in Figure 3.21 when  $\omega=89.5\text{rpm}$ . When  $\omega$  goes higher than 96rpm, the double pendulum oscillates around the radial axis (SR regime) and  $\Delta V_{out}$  falls and continue to decrease when  $\omega$  increases. An example is given in Figure 3.22 when  $\omega=96\text{rpm}$ .

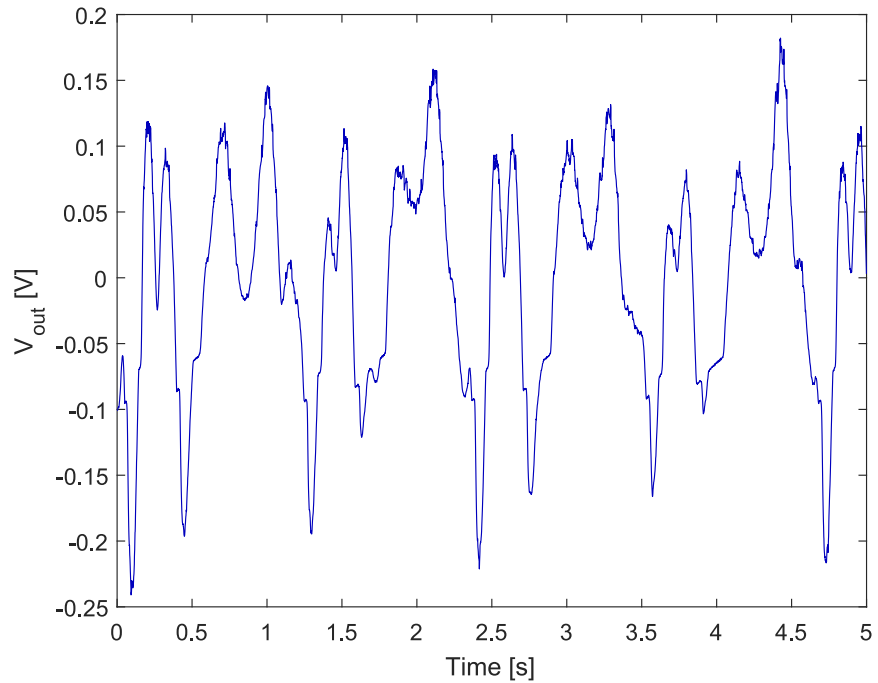
---

EXPERIMENTAL SETUP AND RESULTS

---

Table 3.6: Generated voltage from double pendulum for different rotation speeds

$V_{in}$ [V]	0.5	0.6	0.65	0.66	0.7	0.75	0.8	0.85
$\omega$ [rpm]	29	46	53	54	58.5	67	75.5	84
$V_{out(max)}$ [V]	0.04	0.14	0.17	0.18	6.50E-01	0.74	0.75	0.75
$V_{out(min)}$ [V]	-0.02	-0.2	-0.21	-0.24	-6.40E-01	-0.67	-0.74	-0.75
$\Delta V_{out}$ [V]	0.06	0.34	0.38	0.42	1.29	1.41	1.49	1.5
Regime type	SV	SV	SV	SV	AP	AP	AP	AP
$V_{in}$ [V]	0.9	0.95	1	1.5	2	2.5	3.4	
$\omega$ [rpm]	89.5	96	103.5	171	240	304	418	
$V_{out(max)}$ [V]	0.75	0.32	0.32	0.2	0.1	7.45E-03	3.40E-03	
$V_{out(min)}$ [V]	-0.75	-0.43	-0.4	-0.19	-0.1	-4.45E-03	3.70E-04	
$\Delta V_{out}$ [V]	1.5	0.75	0.72	0.39	0.2	0.012	0.003	
Regime type	AP	SR	SR	SR	SR	SR	SR	


Figure 3.20: Generated voltage from double pendulum for  $\omega=54$  rpm (SV)

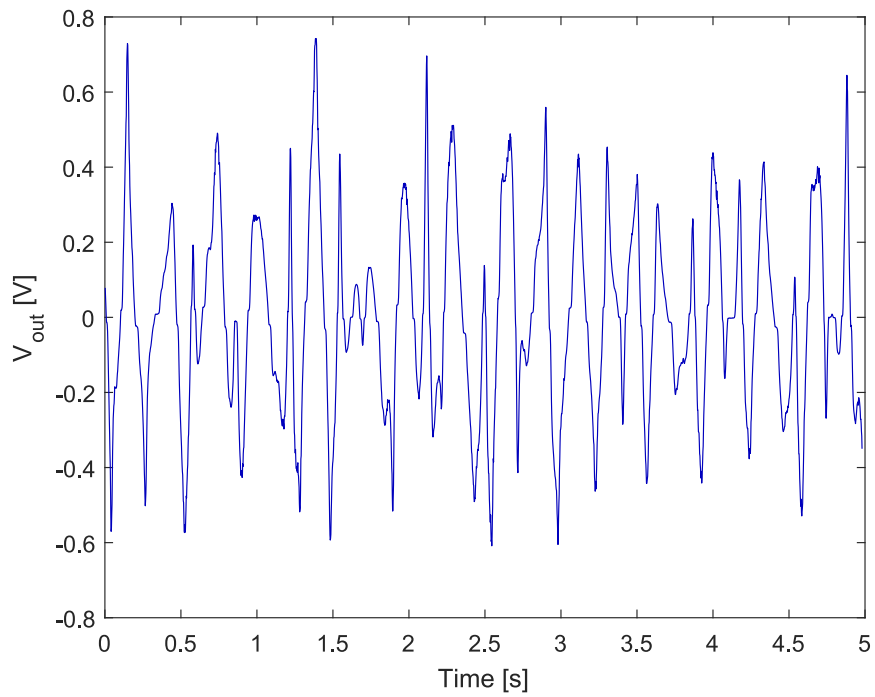


Figure 3.21: Generated voltage from double pendulum for  $\omega=89.5\text{rpm}$  (AP)

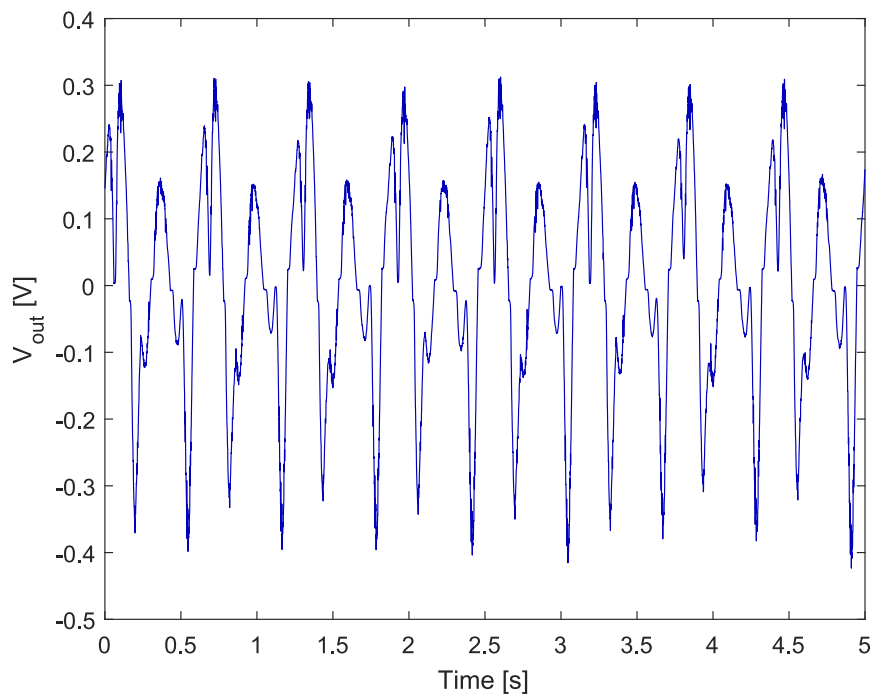


Figure 3.22: Generated voltage from double pendulum for  $\omega=96\text{rpm}$  (SR)

### 3.5.1.3 ROTT'S PENDULUM

For the third proposed experiment, we use the Rott's pendulum presented in Figure 3.11. The results summarized in Table 3.7 shows measurements of the output voltage loaded for different rotation speeds. We notice that, for  $\omega$  equals to 25rpm, the Rott's pendulum oscillates around the vertical axis where the generated voltage is very small. The detailed time dependent response is shown in Figure 3.23. For a rotation speed going from 46rpm to 90rpm, oscillations behavior changes to be in the AP regime,  $\Delta V_{out}$  increases when  $\omega$  increases to reach a peak equals to 1.05V when  $\omega$  is about 85rpm. The corresponding time response is reported in Figure 3.24. From  $\omega$  equals to 90rpm, the Rott's pendulum oscillates around the radial axis and  $\Delta V_{out}$  falls and continue to decrease when  $\omega$  increases. The time response for  $\omega=90$ rpm is shown in Figure 3.25.

Table 3.7: Generated voltage from Rott's pendulum for different rotation speeds

Vin [V]	0.5	0.6	0.65	0.7	0.75	0.8	0.85	0.9
$\omega$ [rpm]	25	46	53	59	68	77	85	90
$V_{out(max)}$ [V]	0.02	0.21	0.38	0.44	0.5	0.5	0.48	0.28
$V_{out(min)}$ [V]	-0.01	-0.2	-0.37	-0.42	-0.44	-0.45	-0.57	-0.15
$\Delta V_{out}$ [V]	0.03	0.41	0.75	0.86	0.94	0.95	1.05	0.430
Observation	SV	AP	AP	AP	AP	AP	AP	SR

Vin [V]	0.95	1	1.5	2	2.5	3	3.4
$\omega$ [rpm]	97	104	172	240	303	367	418
$V_{out(max)}$ [V]	0.26	0.22	0.1	0.06	0.04	5.13E-03	4.30E-03
$V_{out(min)}$ [V]	-0.14	-0.13	-0.07	-0.04	-0.03	-1.51E-03	-8.63E-04
$\Delta V_{out}$ [V]	0.4	0.35	0.17	0.1	0.07	0.00664	0.00516
Observation	SR	SR	SR	SR	SR	SR	SR

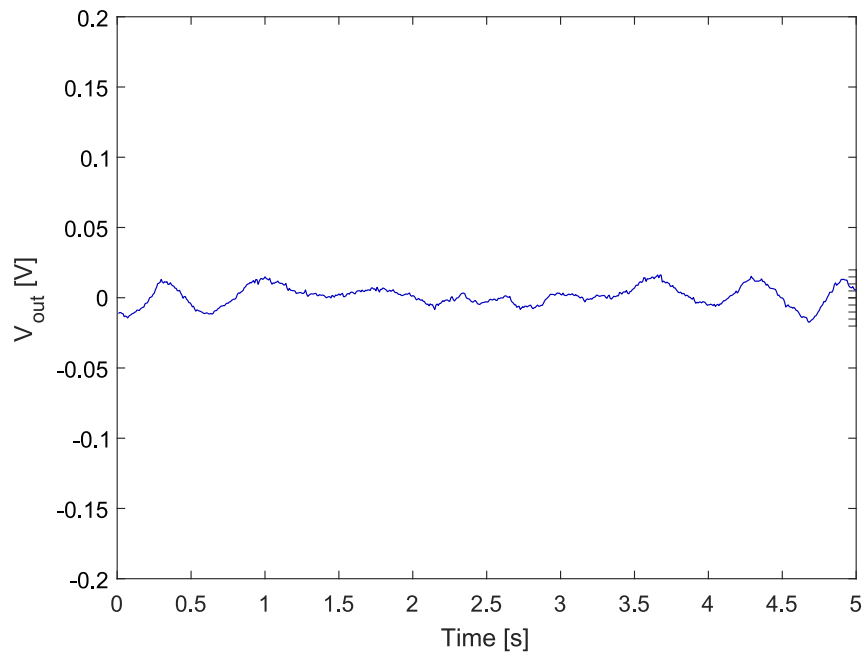


Figure 3.23: Generated voltage from Rott's pendulum for  $\omega=25\text{rpm}$  (SV)

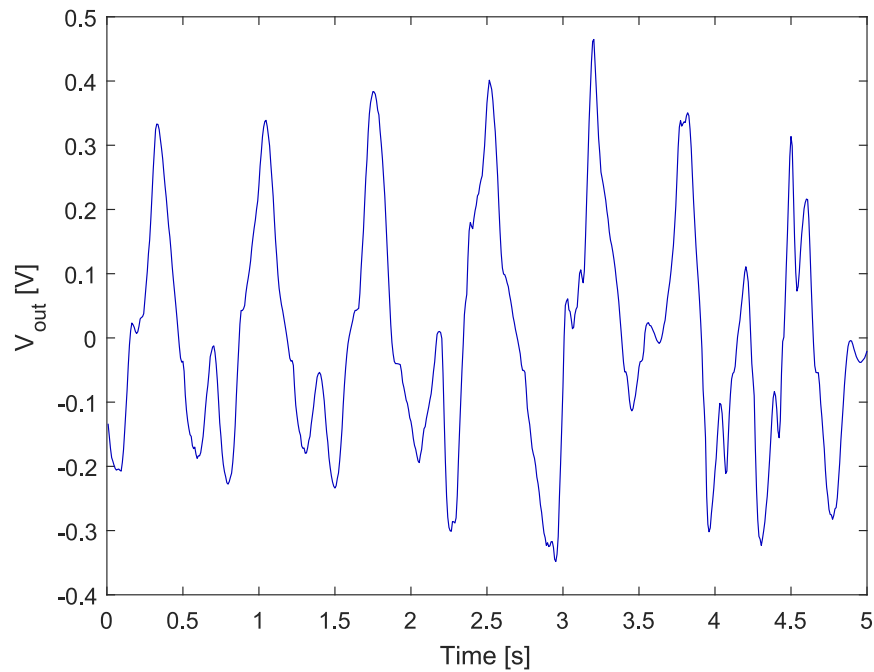
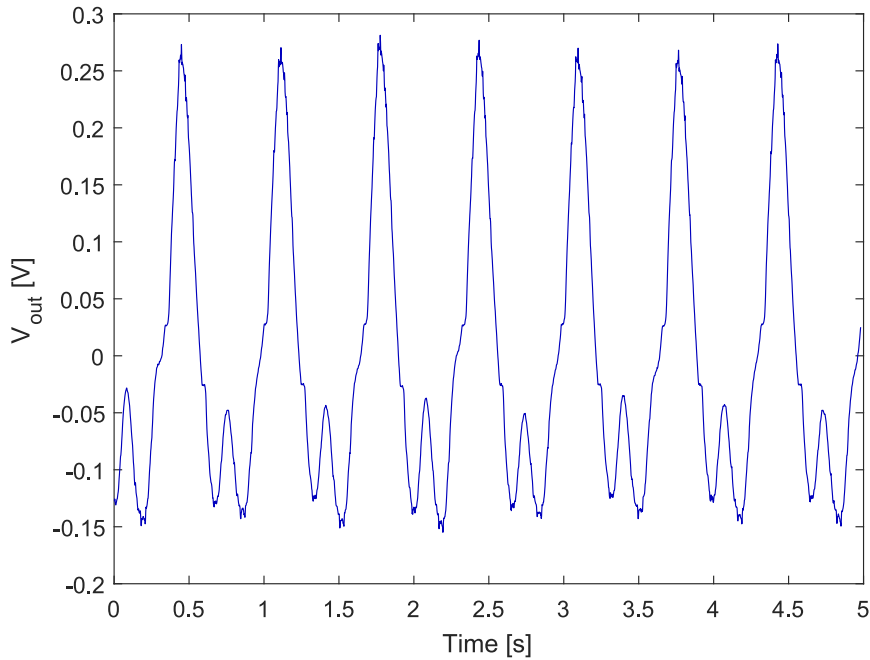


Figure 3.24: Generated voltage from Rott's pendulum for  $\omega=85\text{rpm}$  (AP)


 Figure 3.25: Generated voltage from Rott's pendulum for  $\omega=90\text{rpm}$  (SR)

### 3.5.1.4 COMPARISON BETWEEN DIFFERENT PENDULUMS BEHAVIORS

From the previously accomplished tests concerned with the three types of pendulums, we plot in Figure 3.26 the variation of  $\Delta V_{out}$  as the rotation speed is increased. We note that there are similar behaviors between the three pendulums. In fact,  $\Delta V_{out}$  increases when the behavior is in the SV regime. This is due to the fact that, at this regime, the rotation speed of the pendulum about the disk is equal to the rotation speed of the disc about its base. As a result the generator is almost driven by the rotation of the disk because the gravity forces are dominant.

As the rotation speed is increased the behavior switches to the AP regime and  $\Delta V_{out}$  jumps to higher values thanks to large displacements of the pendulum. The output voltage amplitude continues to increase as the rotation speed of the disk is increased as shown in Figure 3.26. It is in this regime that the device is generating the maximum output power. In fact, at the AP regime, the pendulum is switching between the vertical and radial positions because the weight force and centrifugal force are comparable. The amplitude of the motion is expected to be large. In addition, when the rotation speed of the disk is increased the speed at which this switching is observed is accelerated and the output voltage is increased consequently.

As the rotation speed is further increased, the behavior of the pendulum changes to oscillating around the radial axis (SR). As a result,  $\Delta V_{out}$  is reduced and continues to

decrease during SR regime. This is due to the increase of the centrifugal acceleration which is proportional to the square of the rotational speed of the disk. The switching between the AP and SR regimes is abrupt and highly reduces the output voltage as observed in Figure 3.26.

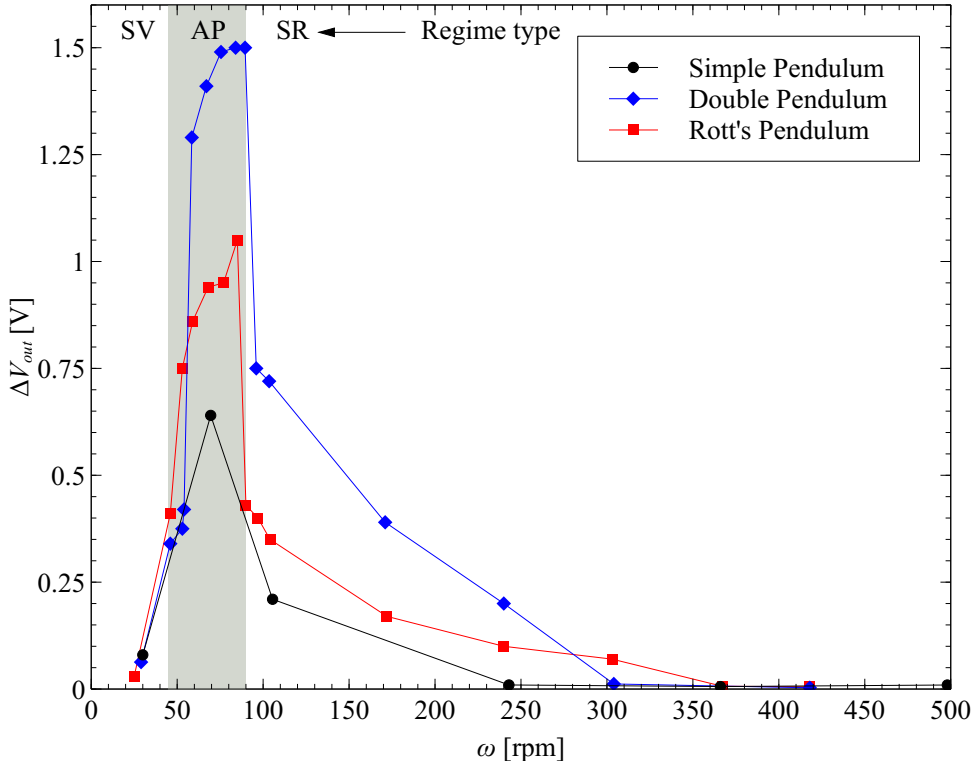


Figure 3.26: Variation of  $\Delta V_{out}$  for different rotation speeds of the disk

It is important to note here that the behavior described above is valid essentially for the double pendulum and the Rott's pendulum. Concerning the simple pendulum, the transition between the SV and SR regimes is very small. We observed that the AP regime is unavailable for the simple pendulum. In fact, in this case the total mass of the pendulum is small compared to the other two cases and the inertial forces can quickly take over the weight force, which eliminates the AP regime for the simple pendulum.

Also the results described in Figure 3.26 are consistent with those given in Chapter 2 and obtained analytically with punctual masses pendulums. In fact, for the transient response regime, we demonstrated that the double pendulum is better than the Rott's pendulum when they are compared regarding the RMS value of the generated voltage.

Concerning the steady state solution, we observed that the double pendulum is still better than the Rott's pendulum for rotation speeds lower than 300 rpm. For higher values,

the Rott's pendulum seems to generate more voltage. This results should be confirmed by analytical analysis tackled in the next chapter. In fact, the two-to-one internal resonance that should improve the Rott's pendulum results is difficult to realize when the device is mounted in the rotating disk because the natural frequencies are affected by the applied centrifugal acceleration which perturb the frequency ratio designed previously.

### 3.5.2 TEST UNDER PERIODIC VARIATION OF THE ANGULAR ROTATION OF THE DISK

Using a variable input function, we record the transient output voltage generated for different initial positions of the disk. In fact, as demonstrated in chapter 2, the initial value describing the position of pendulum is highly correlated to the generated voltage for transient analysis. For this reason we varied the initial position of the disk before sending the input function to initiate the rotation.

The input function is described in Figure 3.27. The function can be described by a half sine signal varying between the rest position and a maximum rotation speed of the disk. The acceleration and deceleration phases, from 0 to 418rpm take 10 seconds, than a rest phase of 10 seconds is applied (Figure 3.27).

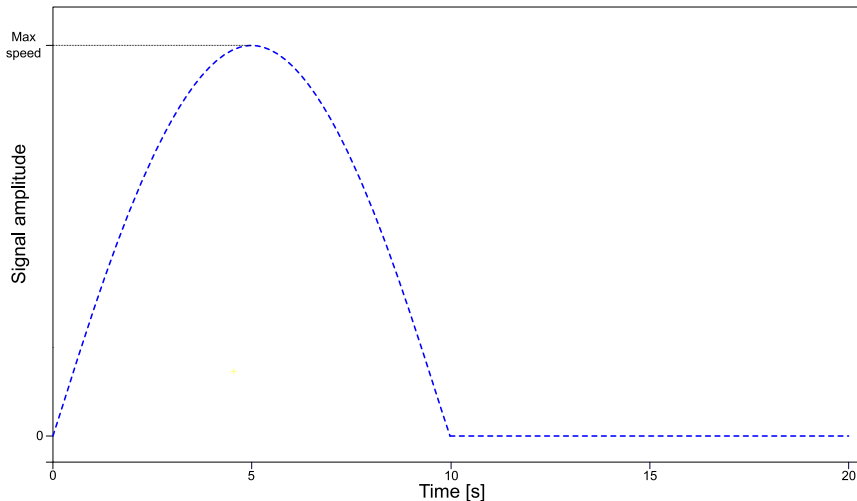


Figure 3.27: Applied input function to actuate the rotating disk.

The initial angular position of the disk, denoted here by the angle  $\theta$  (presented in Figure 2.3 and Figure 2.5), is set to four specific values:  $0$ ,  $\pi/2$ ,  $\pi$  and  $3\pi/2$ . At each one of these initial conditions the input function is applied and the RMS value of the output voltage  $\Delta V_{out}$  is calculated. The experiments were conducted on the double pendulum and Rott's pendulum alone since they are the design that are of interesting in this research work.

### 3.5.2.1 DOUBLE PENDULUM

For the double pendulum design, the output voltage of the generator across the optimal resistance load  $R_{opt}=59\Omega$  are shown in Table 3.8. We confirm here that as demonstrated in the analytical analysis in Chapter 2 that the initial conditions are a very important factor concerning the output voltage. It is found that the measured voltage amplitude  $\Delta V_{out}$  and RMS value of the voltage  $V_{out}^{RMS}$  are maximum when  $\theta = \pi$ . More than 50% drop is observed for these values if the initial condition is set to  $\theta = 0$ . The time response, shown in Figure 3.28, for the case  $\theta = \pi$  and the rotation speed following the input signal in Figure 3.27, depicts the response of the double pendulum design in terms of generated voltage.

Table 3.8: Generated voltage from double pendulum for variable speed for different initial positions

$\theta$ [rad]	0	$\pi/2$	$\pi$	$3\pi/2$
$V_{out(max)}$ [V]	0.68	0.46	0.57	0.26
$V_{out(min)}$ [V]	-0.47	-0.7	-0.84	-0.29
$\Delta V_{out}$ [V]	1.15	1.16	1.41	0.55
$V_{out}^{RMS}$ [V]	0.0846	0.1093	0.127	0.065

The pendulum response shown in Figure 3.28 shows that the transient behavior observed during the acceleration phase of the disk generates higher voltages. When the disk is close to its maximum speed, the pendulum behavior is switched to the SR type where the centrifugal force is dominant and the amplitude of motion is small. Once the deceleration phase is started the amplitude of the motion starts increasing because the steady state motion due to the presence of the centrifugal force is perturbed. When the disk is stopped, a free vibration motion is observed at the end of the half sine signal.

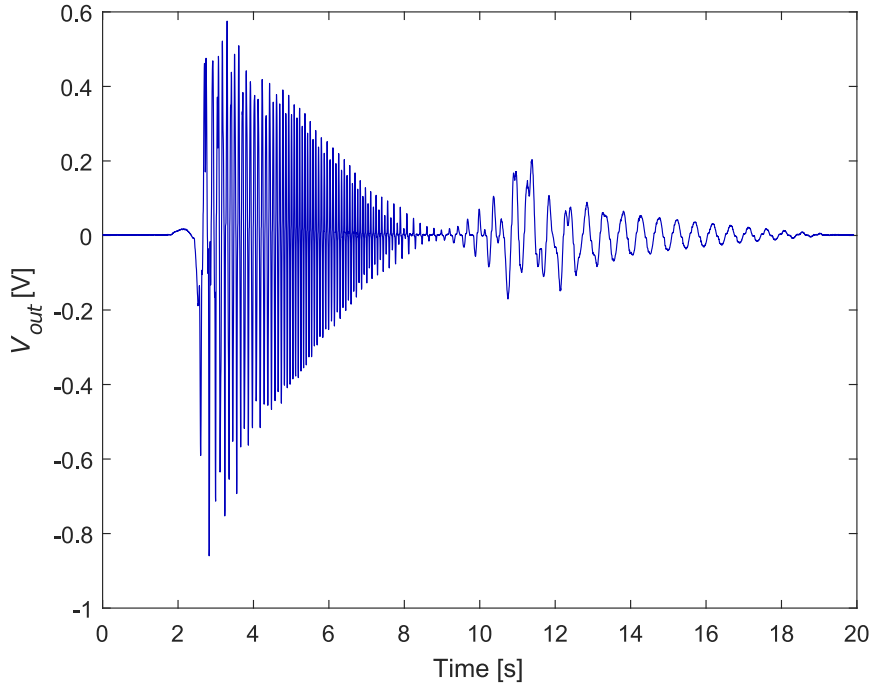


Figure 3.28: Generated voltage from double pendulum for variable speed for initial position  $\theta=\pi$

### 3.5.2.2 ROTT'S PENDULUM

The Rott's pendulum design is treated similarly to the double pendulum design with the input signal in Figure 3.27. The results of the output voltage of the Rott's pendulum design are shown in Table 3.9. Again we observe that the initial condition corresponding to  $\theta = \pi$  gives the maximum output amplitude voltage and RMS value. Also an important drop of these values is noticed for other initial conditions. The time response corresponding to the output voltage for  $\theta = \pi$  is shown in Figure 3.29. Here the time response is similar to the one observed in the previous case.

Table 3.9: Generated voltage from Rott's pendulum for variable speed for different initial positions

$\theta$ [rad]	0	$\pi/2$	$\pi$	$3\pi/2$
$V_{out(max)}$ [V]	0.23	0.41	0.69	0.39
$V_{out(min)}$ [V]	-0.23	-0.42	-0.55	-0.34
$\Delta V_{out}$ [V]	0.46	0.83	1.24	0.73
$V_{out}^{RMS}$ [V]	0.0513	0.0821	0.1035	0.0704

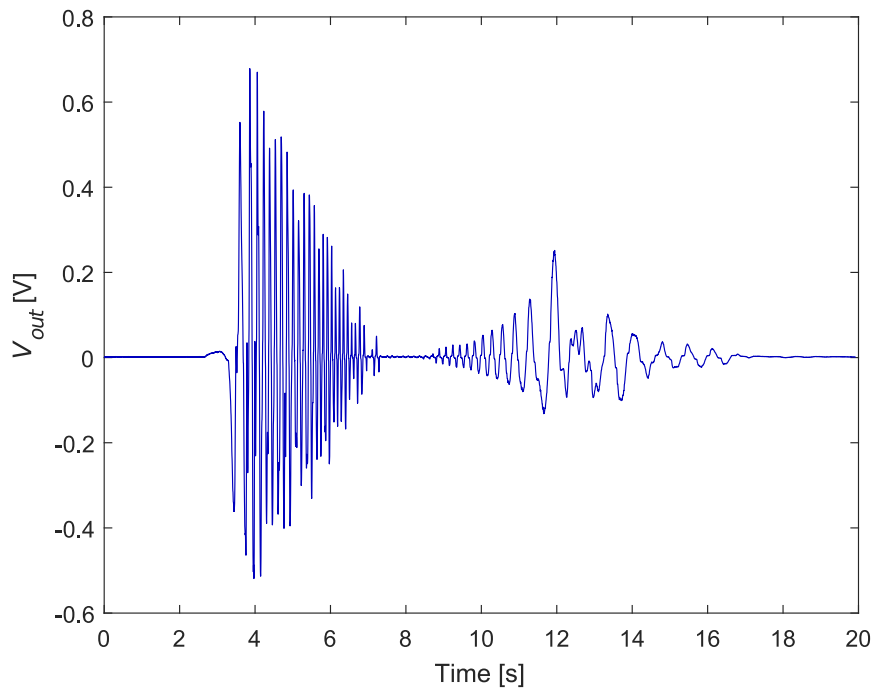


Figure 3.29: Generated voltage from Rott's pendulum for variable speed for initial position  $\theta=\pi$

### 3.5.2.3 COMPARISON BETWEEN DIFFERENT PENDULUMS BEHAVIORS

Figure 3.30 shows all RMS values calculated for the double pendulum and the Rott's pendulum for several initial positions of the disk. For all cases the input signal, shown in Figure 3.27, is applied. We remark that the double pendulum depicts better RMS values of the output voltage than the Rott's pendulum. The general variation tendency is also conserved between the two designs.

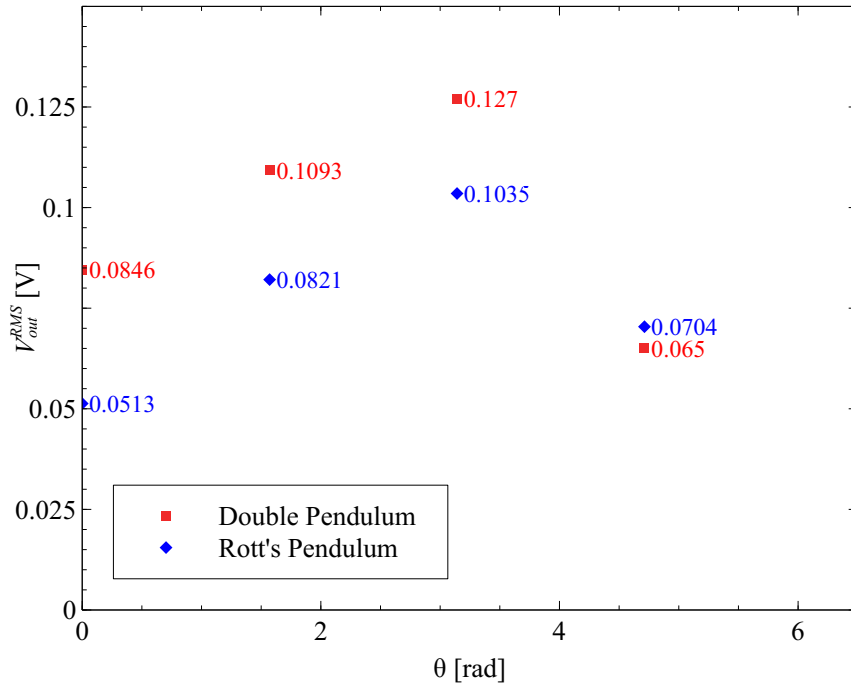


Figure 3.30: RMS values of  $\Delta V_{out}$  for each initial position for double and Rott's pendulum designs.

### 3.6 CONCLUSION

In this chapter, we putted into experiment three pendulum designs: simple pendulum, double pendulum and Rott's pendulum. The electromagnetic generator in which pendulums were mounted was characterized independently. The torque developed at the generator's shaft and the generated power were estimated using a direct driving method. We found that the generated torque is proportional to the rotation speed of the shaft. This proportionality was also validated experimentally.

The optimum load resistance for power output of the generator was measured equal to 59 Ohms. The resonance frequency of each pendulum was also measured by the mean of laser vibrometer.

The test bench which simulates the behavior of a car rim was designed and fabricated. The solution for the steady-state behavior of each pendulum, generated at angular velocity for different rotation speeds, was experimentally tested. We noticed that three different regimes are present: oscillations around the vertical axis, aperiodic oscillations and oscillations around the radial axis. The aperiodic regime gives better output voltage for each pendulum and the double pendulum gives the better generated energy.

Then, a half-sine input function was used to record the transient output voltage generated for different initial positions of the disk for each pendulum. The RMS value was calculated. For each pendulum, a better RMS values were measured when  $\theta = \pi$ . Also in this case of study, the double pendulum gives better results for a majority of the tested initial conditions.



# 4

## NONLINEAR STEADY STATE BEHAVIOR OF THE ROTT'S PENDULUM

For this chapter, an analytical approach is proposed to analyze the behavior of the Rott's pendulum design when it is linked to a rotating wheel, under the steady-state regime. The perturbation technique is used to solve the nonlinear governing equations, in order to clarify the contribution of the different geometrical and physical parameters on the steady-state response of the pendulum under constant rotation speed of the wheel.

### 4.1 PROBLEM STATEMENT

Rott described two requirements for his pendulum to be driven by parametric resonance with a two-to-one internal resonance [93, 96]:

- The line joining the two pivot should be horizontal at equilibrium,
- The natural frequency ratio between the two degree of freedom of the pendulum should be equal to 2.

Rott's pendulum can be decomposed into two pendulums  $P_1$  and  $P_2$  (Figure 4.1). The pendulum  $P_1$  has a mass  $m_1$ , a moment of inertia  $I_1$  about the axis  $(G_1, \vec{z}_0)$ , where  $G_1$  is its center of gravity. Its rotation about the axis  $(A, \vec{z}_0)$  is parameterized by the angle  $\alpha$ . The pendulum  $P_2$  has a mass  $m_2$ , a moment of inertia  $I_2$  about the axis  $(G_2, \vec{z}_0)$ , where  $G_2$  is its center of gravity. Its rotation about the axis  $(B, \vec{z}_0)$  is parameterized by the angle  $\beta$ .

In order to satisfy the first requirement for the design of the Rott's pendulum it is imposed that the center of gravity of the whole system at equilibrium, denoted by  $G$ , should be located along the axis  $(A, \vec{x}_1)$ .

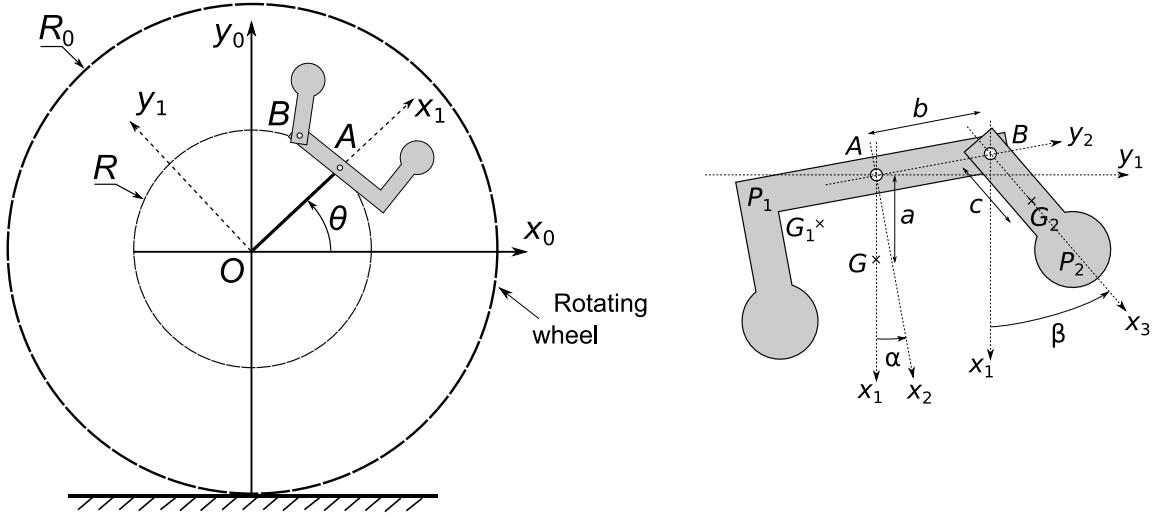


Figure 4.1: Rott's pendulum into a rotating wheel.

The positions of the different centers of gravity are given as follows:

$$\overrightarrow{AG}_1 = a_{G1}\vec{x}_2 - b_{G1}\vec{y}_2 \quad (4.1)$$

$$\overrightarrow{BG}_2 = c\vec{x}_3 \quad (4.2)$$

It is expected that starting from a certain rotation speeds, a radial equilibrium position can be reached and steady state oscillations can be observed around this radial position. The equilibrium position is reached when  $\alpha = 0$  and  $\beta = 0$ . At this configuration, we define the inertial properties of the pendulum.

For simplification, and following Rott [93], we define an hypothetical pendulum, denoted by  $P_1^*$ , composed by  $P_1$  in addition to the mass of  $P_2$  concentrated in  $B$ . The center of mass of this pendulum at equilibrium belongs to axis  $(A, \vec{x}_1)$  at a distance  $a$ . Therefore, using the barycentric properties of center of mass  $G$  of  $P_1^*$ , given by

$$(m_1 + m_2)\overrightarrow{AG} = m_1\overrightarrow{AG}_1 + m_2\overrightarrow{AB}$$

Therefore,

$$a_{G1} = \frac{m_1 + m_2}{m_1}a \quad (4.3)$$

$$b_{G1} = \frac{m_2}{m_1}b \quad (4.4)$$

For the steady state behavior we are assuming that the wheel is rotating at a constant speed corresponding to the cruise speed  $V_0$ . As a result, the rotation speed of the wheel is  $\dot{\theta}(t) = \frac{V_0}{R_0}$  where  $R_0$  is the external radius of the wheel.

## 4.2 EQUATIONS OF MOTION OF THE ROTATING ROTT'S PENDULUM

The kinetic energy of the rotating Rott's pendulum is obtained by calculating the kinetic energy of the pendulums  $P_1$  and  $P_2$  with respect to the reference Galilean frame  $\mathcal{R}_0(O, \vec{x}_0, \vec{y}_0, \vec{z}_0)$ . They are given by

$$K(P_1/\mathcal{R}_0) = \frac{1}{2}m_1 \vec{V}_{G_1/\mathcal{R}_0}^2 + \frac{1}{2}I_1(\dot{\alpha} + \dot{\theta})^2 \quad (4.5)$$

$$K(P_2/\mathcal{R}_0) = \frac{1}{2}m_2 \vec{V}_{G_2/\mathcal{R}_0}^2 + \frac{1}{2}I_2(\dot{\beta} + \dot{\theta})^2 \quad (4.6)$$

where  $\vec{V}_{G_1/\mathcal{R}_0} = \frac{d\overrightarrow{OG_1}}{dt}_{/\mathcal{R}_0}$ ,  $\vec{V}_{G_2/\mathcal{R}_0} = \frac{d\overrightarrow{OG_2}}{dt}_{/\mathcal{R}_0}$  and

$$\overrightarrow{OG_1} = R\vec{x}_1 + a_{G1}\vec{x}_2 - b_{G1}\vec{y}_2 \quad (4.7)$$

$$\overrightarrow{OG_2} = R\vec{x}_1 + b\vec{y}_2 + c\vec{x}_3 \quad (4.8)$$

The potential energy of the system is described by

$$\Pi = -m_1 \vec{g} \cdot \overrightarrow{OG_1} - m_2 \vec{g} \cdot \overrightarrow{OG_2} \quad (4.9)$$

where  $\vec{g} = -g\vec{y}_0$ .

The governing equations are obtained by using the Lagrange equations where the Lagrangian is  $\mathcal{L} = K(P_1/\mathcal{R}_0) + K(P_2/\mathcal{R}_0) - \Pi$ , en end up with

$$\frac{d}{dt} \frac{\partial \mathcal{L}}{\partial \dot{\alpha}} - \frac{\partial \mathcal{L}}{\partial \alpha} = -(c_1 + c_{em})\dot{\alpha} \quad (4.10)$$

$$\frac{d}{dt} \frac{\partial \mathcal{L}}{\partial \dot{\beta}} - \frac{\partial \mathcal{L}}{\partial \beta} = -c_2\dot{\beta} \quad (4.11)$$

where  $c_1$  and  $c_2$  are viscous damping coefficients and  $c_{em} = \frac{K_\omega^2}{\eta R_{opt}}$  is electromagnetic damping due to the generator at optimum resistance load calculated from Equation 3.11. From Chapter 4 we found that  $R_{opt} = 59\Omega$ ,  $K_\omega = 14.99\text{mV/s}$  and  $\eta = 0.81$ .

Therefore, the equations of motion are given as follows:

$$I_A \ddot{\alpha} - bcm_2 \sin(\alpha - \beta)\ddot{\beta} + (c_1 + c_{em})\dot{\alpha} + bcm_2 \cos(\alpha - \beta) (\dot{\beta} + \dot{\theta})^2 \quad (4.12)$$

$$+ a(m_1 + m_2)R\dot{\theta}^2 \sin \alpha + ag(m_1 + m_2) \cos(\alpha + \theta) = 0$$

$$I_B \ddot{\beta} - bcm_2 \sin(\alpha - \beta)\ddot{\alpha} + c_2\dot{\beta} - bcm_2 \cos(\alpha - \beta) (\dot{\alpha} + \dot{\theta})^2 \quad (4.13)$$

$$+ cm_2R\dot{\theta}^2 \sin \beta + cg m_2 \cos(\beta + \theta) = 0$$

where

$$I_A = I_1 + m_1(a_{G1}^2 + b_{G1}^2) + m_2b^2$$

$$I_B = I_2 + m_2c^2$$

For small oscillations around the equilibrium positions, we assume that the rotation angles  $\alpha$  and  $\beta$  can be written as a sum of a equilibrium angle and a small oscillation position, that is

$$\alpha = \alpha_0 + \eta_1 \quad (4.14)$$

$$\beta = \beta_0 + \eta_2 \quad (4.15)$$

where  $\alpha_0$  and  $\beta_0$  are the equilibrium positions that will be determined.

To determine the equilibrium position, we ignore the gravity effect in Equation 4.12 and 4.13 and also suppose that a steady state is reached, that is  $\eta_1 = 0$  and  $\eta_2 = 0$ . We end up with the following relations that define the equilibrium angles of the pendulums  $P_1$  and  $P_2$ .

$$bcm_2 \cos(\alpha_0 - \beta_0) + a(m_1 + m_2)R \sin \alpha_0 = 0 \quad (4.16)$$

$$- b \cos(\alpha_0 - \beta_0) + R \sin \beta_0 = 0 \quad (4.17)$$

It is worth noting here that these angles are independent of the rotation speed, they only depend on the geometry, this is due to radial form of the inertial force field.

We expand the equations of motion in Equation 4.12 and 4.13 using Taylor series around  $\alpha_0$  and  $\beta_0$ . In addition, for a constant rotation speed of the wheel, i.e.  $\theta = \dot{\theta}t$ , we end up with

$$\begin{aligned} I_A \ddot{\eta}_1 - bcm_2(s_{\alpha\beta} + c_{\alpha\beta}(\eta_1 - \eta_2)) \ddot{\eta}_2 + (c_1 + c_{em})\dot{\eta}_1 \\ + bcm_2(c_{\alpha\beta} - s_{\alpha\beta}(\eta_1 - \eta_2)) (\dot{\eta}_2 + \dot{\theta})^2 + a(m_1 + m_2)R\dot{\theta}^2(s_\alpha + c_\alpha\eta_1) \\ + ag(m_1 + m_2) (\cos(\dot{\theta}t + \alpha_0) - \eta_1 \sin(\dot{\theta}t + \alpha_0)) = 0 \end{aligned} \quad (4.18)$$

$$\begin{aligned} I_B \ddot{\eta}_2 - bcm_2(s_{\alpha\beta} + c_{\alpha\beta}(\eta_1 - \eta_2)) \ddot{\eta}_1 + c_2\dot{\eta}_2 + cm_2R\dot{\theta}^2(s_\beta + c_\beta\eta_2) \\ - bcm_2(c_{\alpha\beta} - s_{\alpha\beta}(\eta_1 - \eta_2)) (\dot{\eta}_1 + \dot{\theta})^2 \\ + cm_2g (\cos(\dot{\theta}t + \beta_0) - \eta_2 \sin(\dot{\theta}t + \beta_0)) = 0 \end{aligned} \quad (4.19)$$

where

$$s_{\alpha\beta} = \sin(\alpha_0 - \beta_0), \quad c_{\alpha\beta} = \cos(\alpha_0 - \beta_0),$$

$$s_\alpha = \sin \alpha_0, \quad c_\alpha = \cos \alpha_0, \quad s_\beta = \sin \beta_0 \text{ and } c_\beta = \cos \beta_0$$

Introducing the following parameters:

$$\begin{aligned}\omega_1^2 &= \frac{\dot{\theta}^2}{I_A} (a(m_1 + m_2)c_\alpha R - bcm_2 s_{\alpha\beta}), \quad \omega_2^2 = \frac{cm_2 \dot{\theta}^2}{I_B} (Rc_\beta - bs_{\alpha\beta}) \\ \Gamma_1 &= \frac{bcm_2}{I_A}, \quad \Gamma_2 = \frac{bcm_2}{I_B}, \quad \omega_{01}^2 = \frac{a(m_1 + m_2)g}{I_A}, \quad \omega_{02}^2 = \frac{cm_2 g}{I_B} \\ 2\mu_1 &= \frac{c_1 + c_{em}}{I_A}, \quad 2\mu_2 = \frac{c_2}{I_B}\end{aligned}\quad (4.20)$$

We finally obtain the following equations:

$$\begin{aligned}\ddot{\eta}_1 + \left( \omega_1^2 - \omega_{01}^2 \sin(\dot{\theta}t + \alpha_0) \right) \eta_1 + 2\mu_1 \dot{\eta}_1 \\ + \Gamma_1 c_{\alpha\beta} \left( \dot{\eta}_2 (\dot{\eta}_2 + 2\dot{\theta}) - \ddot{\eta}_2 (\eta_1 - \eta_2) \right) \\ + \Gamma_1 s_{\alpha\beta} \left( \eta_2 (\dot{\eta}_2 + \dot{\theta})^2 + \eta_1 \dot{\eta}_2 (\dot{\eta}_2 - 2\dot{\theta}) - \ddot{\eta}_2 \right) = -\omega_{01}^2 \cos \dot{\theta}t\end{aligned}\quad (4.21)$$

$$\begin{aligned}\ddot{\eta}_2 + \left( \omega_2^2 - \omega_{02}^2 \sin(\dot{\theta}t + \beta_0) \right) \eta_2 + 2\mu_2 \dot{\eta}_2 \\ + \Gamma_2 c_{\alpha\beta} \left( -\dot{\eta}_1 (\dot{\eta}_1 - 2\dot{\theta}) - \ddot{\eta}_1 (\eta_1 - \eta_2) \right) \\ + \Gamma_2 s_{\alpha\beta} \left( \eta_1 (\dot{\eta}_1 + \dot{\theta})^2 - \eta_2 \dot{\eta}_1 (\dot{\eta}_1 - 2\dot{\theta}) - \ddot{\eta}_1 \right) = -\omega_{02}^2 \cos \dot{\theta}t\end{aligned}\quad (4.22)$$

Equations 4.21 and 4.22 are consistent with those derived by Nayfeh [96] when the rotation of the wheel is stopped ( $\dot{\theta} = 0$ ) at position  $\theta = -\frac{\pi}{2}$  and  $\alpha_0 = \beta_0 = 0$ . They depict a quadratic nonlinearity terms with a possibly principal parametric excitations around both modes. Since the natural frequencies of the pendulum in this configuration are both proportional to  $\dot{\theta}$  (Equation 4.20), the variation of the speed of the wheel will not affect the resonance condition, whether is it principal or parametric.

Regarding the last Rott's condition for the two-to-one internal resonance, its obtained for the case at hand when the ratio  $\frac{\omega_2}{\omega_1} = 2$ , using their expressions in Equation 4.20, we end up with

$$\frac{\omega_2^2}{\omega_1^2} = \frac{I_B (a(m_1 + m_2)c_\alpha R - bcm_2 s_{\alpha\beta})}{cm_2 I_A (Rc_\beta - bs_{\alpha\beta})} = 4 \quad (4.23)$$

### 4.3 NONLINEAR SOLUTION USING A PERTURBATION ANALYSIS

To solve Equations 4.21 and 4.22 for the nonlinear response, we use the method of multiple scales. Introducing a small dimensionless parameter  $\epsilon$  to the equations. We rewrite the

equations of motion as follows:

$$\begin{aligned} \ddot{\eta}_1 + \omega_1^2 \eta_1 + \epsilon \left[ 2\mu_1 \dot{\eta}_1 - \omega_{01}^2 \sin(\dot{\theta}t + \alpha_0) \eta_1 + \omega_{01}^2 \cos \dot{\theta}t \right. \\ \left. + \Gamma_1 c_{\alpha\beta} (\dot{\eta}_2 (\dot{\eta}_2 + 2\dot{\theta}) - \ddot{\eta}_2 (\eta_1 - \eta_2)) \right. \\ \left. + \Gamma_1 s_{\alpha\beta} \left( \eta_2 (\dot{\eta}_2 + \dot{\theta})^2 + \eta_1 \dot{\eta}_2 (\dot{\eta}_2 - 2\dot{\theta}) - \ddot{\eta}_2 \right) \right] = 0 \end{aligned} \quad (4.24)$$

$$\begin{aligned} \ddot{\eta}_2 + \omega_2^2 \eta_2 + \epsilon \left[ 2\mu_2 \dot{\eta}_2 - \omega_{02}^2 \sin(\dot{\theta}t + \beta_0) \eta_2 + \omega_{02}^2 \cos \dot{\theta}t \right. \\ \left. + \Gamma_2 c_{\alpha\beta} (-\dot{\eta}_1 (\dot{\eta}_1 - 2\dot{\theta}) - \ddot{\eta}_1 (\eta_1 - \eta_2)) \right. \\ \left. + \Gamma_2 s_{\alpha\beta} \left( \eta_1 (\dot{\eta}_1 + \dot{\theta})^2 - \eta_2 \dot{\eta}_1 (\dot{\eta}_1 - 2\dot{\theta}) - \ddot{\eta}_1 \right) \right] = 0 \end{aligned} \quad (4.25)$$

Using a first order expansion of the solution, we let

$$\eta_1(t, \epsilon) = \eta_{10}(T_0, T_1) + \epsilon \eta_{11}(T_0, T_1) + \dots \quad (4.26)$$

$$\eta_2(t, \epsilon) = \eta_{20}(T_0, T_1) + \epsilon \eta_{21}(T_0, T_1) + \dots \quad (4.27)$$

where  $T_0 = t$  and  $T_1 = \epsilon t$ .

The time derivative are transformed accordingly to

$$\frac{d}{dt} = D_0 + \epsilon D_1 + \dots \quad (4.28)$$

$$\frac{d^2}{dt^2} = D_0^2 + 2\epsilon D_0 D_1 + \dots \quad (4.29)$$

where  $D_i = \frac{\partial}{\partial T_i}$ .

Applying the transformations in Equations 4.26 to 4.29 and equating like powers of  $\epsilon$ , we obtain:

to the order  $\epsilon^0$

$$D_0^2 \eta_{10} + \omega_1^2 \eta_{10} = 0 \quad (4.30)$$

$$D_0^2 \eta_{20} + \omega_2^2 \eta_{20} = 0 \quad (4.31)$$

The solution of Equations 4.30 and 4.31 are given by

$$\eta_{10} = A_1(T_1) e^{i\omega_1 T_0} + \bar{A}_1(T_1) e^{-i\omega_1 T_0} \quad (4.32)$$

$$\eta_{20} = A_2(T_1) e^{i\omega_2 T_0} + \bar{A}_2(T_1) e^{-i\omega_2 T_0} \quad (4.33)$$

to the order  $\epsilon^1$

$$\begin{aligned} D_0^2\eta_{11} + \omega_1^2\eta_{11} = & -2D_0D_1\eta_{10} - 2\mu_1D_0\eta_{10} + \omega_{01}^2\eta_{10}\sin(\dot{\theta}T_0 + \alpha_0) - \omega_{01}^2\cos(\dot{\theta}T_0) \\ & + c_{\alpha\beta}\Gamma_1\left(\eta_{10}D_0^2\eta_{20} - (D_0\eta_{20})^2 - 2\dot{\theta}D_0\eta_{20} - \eta_{20}D_0^2\eta_{20}\right) \\ & + s_{\alpha\beta}\Gamma_1\left(-\dot{\theta}^2\eta_{20} + 2\dot{\theta}\eta_{10}D_0\eta_{20} - 2\dot{\theta}\eta_{20}D_0\eta_{20} - \eta_{10}(D_0\eta_{20})^2\right. \\ & \left.- \eta_{20}(D_0\eta_{20})^2 + D_0^2\eta_{20}\right) \end{aligned} \quad (4.34)$$

$$\begin{aligned} D_0^2\eta_{21} + \omega_2^2\eta_{21} = & -2D_0D_1\eta_{20} - 2\mu_2D_0\eta_{20} + \omega_{02}^2\eta_{20}\sin(\dot{\theta}T_0 + \beta_0) - \omega_{02}^2\cos(\dot{\theta}T_0) \\ & + c_{\alpha\beta}\Gamma_2\left(-\eta_{20}D_0^2\eta_{10} + (D_0\eta_{10})^2 - 2\dot{\theta}D_0\eta_{10} + \eta_{10}D_0^2\eta_{10}\right) \\ & + s_{\alpha\beta}\Gamma_2\left(-\dot{\theta}^2\eta_{10} - 2\dot{\theta}\eta_{10}D_0\eta_{10} - 2\dot{\theta}\eta_{20}D_0\eta_{10} - \eta_{10}(D_0\eta_{10})^2\right. \\ & \left.+ \eta_{20}(D_0\eta_{10})^2 + D_0^2\eta_{10}\right) \end{aligned} \quad (4.35)$$

Substituting Equations 4.32 and 4.33 into Equations 4.34 and 4.35 we obtain

$$\begin{aligned} D_0^2\eta_{11} + \omega_1^2\eta_{11} = & -\frac{1}{2}\omega_{01}^2e^{i\dot{\theta}T_0} - 2(i\omega_1(A'_1 + \mu_1A_1) + s_{\alpha\beta}\Gamma_1\omega_2^2A_1A_2\bar{A}_2)e^{i\omega_1T_0} \\ & - \frac{1}{2}ie^{i\alpha_0}\omega_{01}^2\bar{A}_1e^{i(\dot{\theta}-\omega_1)T_0} + \left(2is_{\alpha\beta}\dot{\theta}\omega_2 - c_{\alpha\beta}\omega_2^2\right)\Gamma_1\bar{A}_1A_2e^{i(\omega_2-\omega_1)T_0} \\ & + NST + cc \end{aligned} \quad (4.36)$$

$$\begin{aligned} D_0^2\eta_{21} + \omega_2^2\eta_{21} = & -\frac{1}{2}\omega_{02}^2e^{i\dot{\theta}T_0} - 2(i\omega_2(A'_2 + \mu_2A_2) + s_{\alpha\beta}\Gamma_2\omega_1^2A_2A_1\bar{A}_1)e^{i\omega_2T_0} \\ & - \frac{1}{2}ie^{i\beta_0}\omega_{02}^2\bar{A}_2e^{i(\dot{\theta}-\omega_2)T_0} + \left(-2is_{\alpha\beta}\dot{\theta}\omega_1 - 2c_{\alpha\beta}\omega_1^2\right)\Gamma_2A_1^2e^{i2\omega_1T_0} \\ & + NST + cc \end{aligned} \quad (4.37)$$

where the primes denote derivative with respect to  $T_1$ ,  $NST$  are the nonsecular terms and  $cc$  stands for the complex conjugate terms. The case where the resonant condition requires that  $\omega_1 > \omega_2$  have been considered as non secular because of the nature of the device.

The particular solutions of Equations 4.36 and 4.37 contains secular terms according to the following first order resonant conditions:

- $\dot{\theta} \approx \omega_1$  with a principal resonance of the first mode,
- $\dot{\theta} \approx \omega_2$  with a principal resonance of the second mode,
- $\omega_2 \approx 2\omega_1$  with a two-to-one internal resonance,
- $\dot{\theta} \approx 2\omega_1$  with a principal parametric resonance of the first mode,
- $\dot{\theta} \approx 2\omega_2$  with a principal parametric resonance of the second mode.

In this chapter we are interested in analyzing the case where the rotation of the wheel initiate a parametric resonance of the second mode meaning that the rotation speed is close to the first natural frequency  $\omega_1$ . The analysis include the case where a two-to-one internal resonance is considered.

## 4.4 PRINCIPAL PARAMETRIC RESONANCE OF THE SECOND MODE WITH 2:1 INTERNAL RESONANCE

### 4.4.1 MODULATION EQUATIONS

Using  $\sigma_1$  and  $\sigma_2$  as detuning parameters, we assume that the frequencies  $\omega_2$  and  $\dot{\theta}$  can be written as

$$\omega_2 = 2\omega_1 + \epsilon\sigma_1 \text{ and } \dot{\theta} = 2\omega_2 + \epsilon\sigma_2 \quad (4.38)$$

Replacing Equation 4.38 into Equations 4.36 and 4.37 and keeping in mind that

$$\omega_2 T_0 = 2\omega_1 T_0 + \sigma_1 T_1 \text{ and } \dot{\theta} T_0 = 2\omega_2 T_0 + \sigma_2 T_1$$

We aim at eliminating quantities that generate secular terms and small divisor terms depending on the resonant conditions, for the solution of Equations 4.36 and 4.37. Therefore, the solvability conditions for these equations are given by:

$$-i(A'_1 + \mu_1 A_1) - \delta_1 A_1 A_2 \bar{A}_2 - (\delta_2 - i\delta_3) \bar{A}_1 A_2 e^{i\sigma_1 T_1} = 0 \quad (4.39)$$

$$-i(A'_2 + \mu_2 A_2) + \delta_4 A_1 \bar{A}_1 A_2 - (\delta_5 + i\delta_6) A_1^2 e^{-i\sigma_1 T_1} + (\delta_7 - i\delta_8) \bar{A}_2 e^{i\sigma_2 T_1} = 0 \quad (4.40)$$

where  $\delta_i$  are real constants defined by

$$\begin{aligned} \delta_1 &= \frac{\Gamma_1 s_{\alpha\beta} \omega_2^2}{\omega_1}, \quad \delta_2 = \frac{\Gamma_1 c_{\alpha\beta} \omega_2^2}{2\omega_1}, \quad \delta_3 = \frac{\Gamma_1 s_{\alpha\beta} \dot{\theta} \omega_2}{\omega_1} \\ \delta_4 &= \frac{\Gamma_2 s_{\alpha\beta} \omega_1^2}{\omega_2}, \quad \delta_5 = \frac{\Gamma_2 c_{\alpha\beta} \omega_1^2}{\omega_2}, \quad \delta_6 = \frac{\Gamma_2 s_{\alpha\beta} \dot{\theta} \omega_1}{\omega_2}, \quad \delta_7 = \frac{1}{4} \frac{\omega_{02}^2}{\omega_2} s_\beta, \quad \delta_8 = \frac{1}{4} \frac{\omega_{02}^2}{\omega_2} c_\beta \end{aligned} \quad (4.41)$$

Next we rewrite the time dependent coefficients  $A_1$  and  $A_2$  in polar complex form as follows

$$A_1(T_1) = a_1(T_1) e^{ib_1(T_1)} \text{ and } A_2(T_1) = a_2(T_1) e^{ib_2(T_1)} \quad (4.42)$$

where  $a_1$ ,  $a_2$ ,  $b_1$  and  $b_2$  are real functions.

Using the amplitude defined in Equation 4.42 into Equations 4.39 and 4.40, equating real and imaginary parts, we end up with the modulation equations given by:

$$a_1 b'_1 - \delta_1 a_1 a_2^2 - \delta_2 a_1 a_2 \cos \gamma_1 - \delta_3 a_1 a_2 \sin \gamma_1 = 0 \quad (4.43)$$

$$a'_1 + \mu_1 a_1 - \delta_3 a_1 a_2 \cos \gamma_1 + \delta_2 a_1 a_2 \sin \gamma_1 = 0 \quad (4.44)$$

$$a_2 b'_2 + \delta_4 a_1^2 a_2 - \delta_5 a_1^2 \cos \gamma_1 - \delta_6 a_1^2 \sin \gamma_1 + \delta_7 a_2 \cos \gamma_2 + \delta_8 a_2 \sin \gamma_2 = 0 \quad (4.45)$$

$$a'_2 + \mu_2 a_2 + \delta_6 a_1^2 \cos \gamma_1 - \delta_5 a_1^2 \sin \gamma_1 - \delta_7 a_2 \sin \gamma_2 + \delta_8 a_2 \cos \gamma_2 = 0 \quad (4.46)$$

where

$$\gamma_1 = b_2 - 2b_1 + \sigma_1 T_1 \text{ and } \gamma_2 = -2b_2 + \sigma_2 T_1 \quad (4.47)$$

From Equation 4.47 we deduce the following:

$$b_1 = \frac{1}{2} \left( \sigma_1 + \frac{1}{2} \sigma_2 \right) T_1 - \frac{1}{2} \left( \gamma_1 + \frac{1}{2} \gamma_2 \right) \text{ and } b_2 = \frac{1}{2} \sigma_2 T_1 - \frac{1}{2} \gamma_2 \quad (4.48)$$

As a result, the first order approximation of the solution is rewritten as

$$\eta_{10} = a_1 e^{i(\omega_1 T_0 + b_1)} + a_1 e^{-i(\omega_1 T_0 + b_1)} \quad (4.49)$$

$$= a_1 \cos(\omega_1 T_0 + b_1)$$

$$\eta_{20} = a_2 e^{i(\omega_2 T_0 + b_2)} + a_2 e^{-i(\omega_2 T_0 + b_2)} \quad (4.50)$$

$$= a_2 \cos(\omega_2 T_0 + b_2)$$

#### 4.4.2 PERIODIC SOLUTIONS AND THEIR STABILITY

Steady state periodic solutions can be obtained for the response described by Equations 4.49 and 4.50. It corresponds to the case where  $a'_1 = a'_2 = \gamma'_1 = \gamma'_2 = 0$ . Under these conditions the periodic response is the fixed points of Equations 4.43 to 4.46.

##### 4.4.2.1 GENERAL CASE FOR SMALL AND LARGE RADIAL POSITIONS OF THE PENDULUM

From Equation 4.48 we deduce that  $b'_1 = \frac{1}{2} (\sigma_1 + \frac{1}{2} \sigma_2)$  and  $b'_2 = \frac{1}{2} \sigma_2$ . Consequently, the fixed points are solutions of

$$\frac{1}{2} \left( \sigma_1 + \frac{1}{2} \sigma_2 \right) - \delta_1 a_2^2 - \delta_2 a_2 \cos \gamma_1 - \delta_3 a_2 \sin \gamma_1 = 0 \quad (4.51)$$

$$\mu_1 - \delta_3 a_2 \cos \gamma_1 + \delta_2 a_2 \sin \gamma_1 = 0 \quad (4.52)$$

$$\frac{1}{2} a_2 \sigma_2 + \delta_4 a_1^2 a_2 - \delta_5 a_1^2 \cos \gamma_1 - \delta_6 a_1^2 \sin \gamma_1 + \delta_7 a_2 \cos \gamma_2 + \delta_8 a_2 \sin \gamma_2 = 0 \quad (4.53)$$

$$\mu_2 a_2 + \delta_6 a_1^2 \cos \gamma_1 - \delta_5 a_1^2 \sin \gamma_1 - \delta_7 a_2 \sin \gamma_2 + \delta_8 a_2 \cos \gamma_2 = 0 \quad (4.54)$$

The solutions of Equations 4.51 to 4.54 are either trivial ( $a_1 = 0$  and  $a_2 = 0$ ), or one can use a continuation technique [105] to obtain the solutions.

#### 4.4.2.2 LARGE RADIAL POSITIONS OF THE PENDULUM

A special case of these equations can be treated analytically if the equilibrium positions are small compared to the angular amplitude ( $\alpha_0 \approx 0$  and  $\beta_0 \approx 0$ ). This is possible if the radius  $R$  at which the pendulum is mounted is large enough. At these conditions, the constant sine and cosine terms are replaced by 0 and 1 respectively. We end up with the following reduced modulation equations:

$$\frac{1}{2} \left( \sigma_1 + \frac{1}{2} \sigma_2 \right) - \bar{\delta}_2 a_2 \cos \gamma_1 = 0 \quad (4.55)$$

$$\mu_1 + \bar{\delta}_2 a_2 \sin \gamma_1 = 0 \quad (4.56)$$

$$\frac{1}{2} a_2 \sigma_2 - \bar{\delta}_5 a_1^2 \cos \gamma_1 + \bar{\delta}_8 a_2 \sin \gamma_2 = 0 \quad (4.57)$$

$$\mu_2 a_2 - \bar{\delta}_5 a_1^2 \sin \gamma_1 + \bar{\delta}_8 a_2 \cos \gamma_2 = 0 \quad (4.58)$$

where

$$\bar{\delta}_2 = \frac{\Gamma_1 \omega_2^2}{2\omega_1}, \bar{\delta}_5 = \frac{\Gamma_2 \omega_1^2}{\omega_2}, \bar{\delta}_8 = \frac{1}{4} \frac{\omega_{02}^2}{\omega_2}$$

The solution is obtained by eliminating the trigonometric terms, we obtain

$$a_2 = \pm \frac{1}{\bar{\delta}_2} \sqrt{\mu_1^2 + \frac{1}{4} (\sigma_1 + \frac{1}{2} \sigma_2)^2} \quad (4.59)$$

One can remark that  $a_2$  is always real and that its value is increased by increasing the detuning parameters  $\sigma_1$  and  $\sigma_2$ .

Also from Equations 4.57 and 4.58 we obtain that

$$\begin{aligned} a_1^2 &= \frac{-\mu_1 \mu_2 + \frac{1}{4} \sigma_2 (\sigma_1 + \frac{1}{2} \sigma_2)}{\bar{\delta}_2 \bar{\delta}_5} \\ &\pm \frac{\bar{\delta}_8}{\bar{\delta}_2 \bar{\delta}_5} \sqrt{\left( \mu_1^2 + \frac{1}{4} (\sigma_1 + \frac{1}{2} \sigma_2)^2 \right) - \frac{(\mu_1 \sigma_2 + \mu_2 (\sigma_1 + \frac{1}{2} \sigma_2))^2}{4 \bar{\delta}_8^2}} \end{aligned} \quad (4.60)$$

The steady state amplitude  $a_2$  is real if the following conditions are satisfied:

$$\sigma_2 (\sigma_1 + \frac{1}{2} \sigma_2) + 4 \mu_1 \mu_2 > 0 \text{ and } \frac{1}{4} \sigma_2^2 + \mu_2^2 - \Lambda_3^2 > 0 \quad (4.61)$$

And the first order approximation of the solution is rewritten again as

$$\alpha \approx a_1(\dot{\theta}) \cos \left( \frac{1}{4} \dot{\theta} t - \frac{1}{2} \gamma_1 - \frac{1}{4} \gamma_2 \right) + \frac{\Gamma_1}{\bar{\omega}_1^2} \quad (4.62)$$

$$\beta \approx a_2(\dot{\theta}) \cos \left( \frac{1}{2} \dot{\theta} t - \frac{1}{2} \gamma_2 \right) + \frac{\Gamma_2}{\bar{\omega}_2^2} \quad (4.63)$$

#### 4.4.2.3 STABILITY ANALYSIS OF THE SOLUTION

The stability of these solutions can be ascertained using the Routh–Hurwitz stability criterion [106]. For this, we start by letting

$$A_1 = (p_1 - iq_1)e^{ib'_1 T_1} \text{ and } A_2 = (p_2 - iq_2)e^{ib'_2 T_1} \quad (4.64)$$

Using Equation 4.39 and 4.40 and separating real and imaginary parts, we end up with

$$p'_1 + \mu_1 p_1 + b'_1 q_1 - \delta_1 q_1(p_2^2 + q_2^2) + \delta_2(p_2 q_1 - p_1 q_2) - \delta_3(p_1 p_2 + q_1 q_2) = 0 \quad (4.65)$$

$$q'_1 + \mu_1 q_1 - b'_1 p_1 + \delta_1 p_1(p_2^2 + q_2^2) + \delta_2(p_1 p_2 + q_1 q_2) + \delta_3(p_2 q_1 - p_1 q_2) = 0 \quad (4.66)$$

$$p'_2 + \mu_2 p_2 + b'_2 q_2 + \delta_4 q_2(p_1^2 + q_1^2) - 2\delta_5 p_1 q_1 + \delta_6(p_1^2 - q_1^2) + \delta_8 p_2 - \delta_7 q_2 = 0 \quad (4.67)$$

$$q'_2 + \mu_2 q_2 - b'_2 p_2 - \delta_4 p_2(p_1^2 + q_1^2) + 2\delta_6 p_1 q_1 + \delta_5(p_1^2 - q_1^2) - \delta_8 q_2 - \delta_7 p_2 = 0 \quad (4.68)$$

Following Nayfeh [96], we linearize Equations 4.65 to 4.68 around the fixed points  $p_i^*$  and  $q_i^*$  ( $i = 1, 2$ ) by assuming a small perturbation proportional to  $e^{\lambda T_1}$ , where  $\lambda$  is a complex number. That is

$$p_i = p_i^* + P_i e^{\lambda T_1} \text{ and } q_i = q_i^* + Q_i e^{\lambda T_1} \quad (4.69)$$

We end up with

$$\begin{bmatrix} \lambda + \mu_1 - \delta_2 q_2^* - \delta_3 p_2^* & b'_1 + \delta_2 p_2^* - \delta_3 q_2^* & \delta_2 q_1^* - \delta_3 p_1^* & -\delta_2 p_1^* - \delta_3 q_1^* \\ -b'_1 + \delta_2 p_2^* - \delta_3 q_2^* & \lambda + \mu_1 + \delta_2 q_2^* + \delta_3 p_2^* & \delta_2 p_1^* + \delta_3 q_1^* & \delta_2 q_1^* - \delta_3 p_1^* \\ 2\delta_6 p_1^* - 2\delta_5 q_1^* & -2\delta_5 p_1^* - 2\delta_6 q_1^* & \lambda + \mu_2 + \delta_8 & b'_2 - \delta_7 \\ 2\delta_5 p_1^* + 2\delta_6 q_1^* & 2\delta_6 p_1^* - 2\delta_5 q_1^* & -b'_2 + \delta_7 & \lambda + \mu_2 - \delta_8 \end{bmatrix} \cdot \begin{pmatrix} P_1 \\ Q_1 \\ P_2 \\ Q_2 \end{pmatrix} = \begin{pmatrix} 0 \\ 0 \\ 0 \\ 0 \end{pmatrix} \quad (4.70)$$

The solutions of the associated characteristic equation defines the stability of the fixed points.

For the non trivial solution we calculate the determinant of the matrix in Equation 4.64, it is given by

$$\lambda^4 + r_1 \lambda^3 + r_2 \lambda^2 + r_3 \lambda + r_4 = 0 \quad (4.71)$$

Using Equation 4.48, and considering only real solutions, we deduce that

$$p_1 = a_1 \cos \left( \frac{1}{2} \left( \gamma_1 + \frac{1}{2} \gamma_2 \right) \right) \quad (4.72)$$

$$q_1 = a_1 \sin \left( \frac{1}{2} \left( \gamma_1 + \frac{1}{2} \gamma_2 \right) \right) \quad (4.73)$$

$$p_2 = a_2 \cos \left( \frac{1}{2} \gamma_2 \right) \quad (4.74)$$

$$q_2 = a_2 \sin \left( \frac{1}{2} \gamma_2 \right) \quad (4.75)$$

Using the Routh-Hurwitz criterion, one can write the necessary and sufficient conditions so that the roots of Equation 4.67 have negative real parts. They are given by

$$\begin{cases} r_1 r_2 - r_3 > 0 \\ r_3(r_1 r_2 - r_3) - r_1^2 r_4 > 0 \\ r_4 > 0 \end{cases} \quad (4.76)$$

## 4.5 PRINCIPAL PARAMETRIC RESONANCE OF THE FIRST MODE WITH 2:1 INTERNAL RESONANCE

### 4.5.1 MODULATION EQUATIONS

For a parametric resonance around the first mode, the detuning parameters  $\sigma_1$  and  $\sigma_2$  are now defined as follows

$$\omega_2 = 2\omega_1 + \epsilon\sigma_1 \text{ and } \dot{\theta} = 2\omega_1 + \epsilon\sigma_2 \quad (4.77)$$

Replacing Equation 4.77 into Equations 4.36 and 4.37, the solvability conditions are given by

$$-i(A'_1 + \mu_1 A_1) - \delta_1 A_1 A_2 \bar{A}_2 - (\delta_2 - i\delta_3) \bar{A}_1 A_2 e^{i\sigma_1 T_1} + (\delta_9 - i\delta_{10}) \bar{A}_1 e^{i\sigma_2 T_1} = 0 \quad (4.78)$$

$$-i(A'_2 + \mu_2 A_2) + \delta_4 A_1 \bar{A}_1 A_2 - (\delta_5 + i\delta_6) A_1^2 e^{-i\sigma_1 T_1} = 0 \quad (4.79)$$

where

$$\delta_9 = \frac{1}{4} \frac{\omega_{01}^2}{\omega_1} s_\alpha, \delta_{10} = \frac{1}{4} \frac{\omega_{01}^2}{\omega_1} c_\alpha \quad (4.80)$$

Using the amplitude defined in Equation 4.42, we calculate the modulation equations given by:

$$a_1 b'_1 - \delta_1 a_1 a_2^2 - \delta_2 a_1 a_2 \cos \gamma_1 - \delta_3 a_1 a_2 \sin \gamma_1 + \delta_9 a_1 \cos \gamma_3 + \delta_{10} a_1 \sin \gamma_3 = 0 \quad (4.81)$$

$$a'_1 + \mu_1 a_1 - \delta_3 a_1 a_2 \cos \gamma_1 + \delta_2 a_1 a_2 \sin \gamma_1 - \delta_9 a_1 \sin \gamma_3 + \delta_{10} a_1 \cos \gamma_3 = 0 \quad (4.82)$$

$$a_2 b'_2 + \delta_4 a_1^2 a_2 - \delta_5 a_1^2 \cos \gamma_1 - \delta_6 a_1^2 \sin \gamma_1 = 0 \quad (4.83)$$

$$a'_2 + \mu_2 a_2 + \delta_6 a_1^2 \cos \gamma_1 - \delta_5 a_1^2 \sin \gamma_1 = 0 \quad (4.84)$$

where

$$\gamma_1 = b_2 - 2b_1 + \sigma_1 T_1 \text{ and } \gamma_3 = -2b_1 + \sigma_2 T_1 \quad (4.85)$$

Therefore,

$$b_1 = \frac{1}{2}\sigma_2 T_1 - \frac{1}{2}\gamma_2 \text{ and } b_2 = (\sigma_2 - \sigma_1)T_1 + \gamma_1 - \gamma_2 \quad (4.86)$$

#### 4.5.2 PERIODIC SOLUTIONS AND THEIR STABILITY

Steady state periodic solutions corresponds to the case where  $a'_1 = a'_2 = \gamma'_1 = \gamma'_3 = 0$ . The fixed points of Equations 4.76 to 4.79 are obtained by letting  $b'_1 = \frac{1}{2}\sigma_3$  and  $b'_2 = \sigma_3 - \sigma_1$ . Consequently, the fixed points are solutions of

$$\frac{1}{2}\sigma_2 - \delta_1 a_2^2 - \delta_2 a_2 \cos \gamma_1 - \delta_3 a_2 \sin \gamma_1 + \delta_9 \cos \gamma_2 + \delta_{10} \sin \gamma_2 = 0 \quad (4.87)$$

$$\mu_1 - \delta_3 a_2 \cos \gamma_1 + \delta_2 a_2 \sin \gamma_1 - \delta_9 \sin \gamma_2 + \delta_{10} \cos \gamma_2 = 0 \quad (4.88)$$

$$a_2(\sigma_2 - \sigma_1) + \delta_4 a_1^2 a_2 - \delta_5 a_1^2 \cos \gamma_1 - \delta_6 a_1^2 \sin \gamma_1 = 0 \quad (4.89)$$

$$\mu_2 a_2 + \delta_6 a_1^2 \cos \gamma_1 - \delta_5 a_1^2 \sin \gamma_1 = 0 \quad (4.90)$$

The solutions of Equations 4.87 to 4.90 are obtained using a continuation technique and the stability is obtained using the same approach described in the previous section.

## 4.6 RESULTS AND DISCUSSION

Assuming the Geometrical and inertial parameters given in Table 4.1, we adopt two different specific designs that satisfy the Rott's conditions, namely the 2:1 internal resonance and the parametric resonance of the second mode.

Table 4.1: Geometrical and inertial parameters of the Rott's pendulum

	Design 1			Design 2	
Pendulum $P_1$	$a_{G1}$	0.06 mm	Pendulum $P_1$	$a_{G1}$	0.89 mm
	$b_{G1}$	-0.86 mm		$b_{G1}$	-2.33 mm
	$b$	6 mm		$b$	11.33 mm
	$m_1$	103 g		$m_1$	190 g
	$I_1$	$10955 \text{ g.mm}^2$		$I_1$	$60804 \text{ g.mm}^2$
Pendulum $P_2$	$c$	5.7 mm	Pendulum $P_2$	$c$	4.35 mm
	$m_2$	14.7 g		$m_2$	39.14 g
	$I_2$	$2888 \text{ g.mm}^2$		$I_2$	$160.13 \text{ g.mm}^2$
Radius	$R$	112.57 mm	Radius	$R$	17.6 mm
Equilibrium	$\alpha_0 = -\beta_0$	$-3.04^\circ$	Equilibrium	$\alpha_0 = -\beta_0$	$-24.73^\circ$
Damping	$c_1$	$10^{-6}$	Damping	$c_1$	$10^{-6}$
	$c_2$	$10^{-6}$		$c_2$	$10^{-6}$
	$c_{em}$	$4.7 \times 10^{-6}$		$c_{em}$	$4.7 \times 10^{-6}$
Gravity	$g$	$9.81 \text{ m.s}^{-2}$	Gravity	$g$	$9.81 \text{ m.s}^{-2}$

The resonance conditions are independent on the rotation speed  $\dot{\theta}$  of the wheel, as demonstrated in Equations 4.20 and 4.23. We start by calculating the response of the pendulum while the rotation speed is varied.

#### 4.6.1 INFLUENCE OF THE ROTATION SPEED: FORCE RESPONSE OF THE DEVICE

The rotation speed is directly proportional to the natural frequencies of the Rott's pendulum as shown in Equation 4.20. As a result, the parametric resonance condition  $\dot{\theta} = 2\omega_2$  is obtained directly by design as it is independent on the choice of the value of  $\dot{\theta}$ . As a result, the rotation speed can be freely varied without compromising the parametric resonance condition and the internal resonance.

The variation of  $\dot{\theta}$  is tested for both designs proposed in Table 4.1. The response shown in the following subsections section is similar to a force-response analysis indirectly controlled by the rotation speed. It is estimated here that radial steady state solutions cannot exist for rotation speeds of the wheel lower than 40 rad/s.

### 4.6.1.1 DESIGN 1

The first proposed design corresponds to the large radial positions of the Rott's pendulum. For this design the specific position is chosen so that the parametric resonance and the internal resonance conditions are both systematically satisfied. Different values of the detuning parameters  $\sigma_1$  and  $\sigma_2$  are tested here.

In Figure 4.2, the response amplitudes  $a_1$  and  $a_2$  are plotted versus the rotation speed for the case  $\sigma_1 = 0$  and different values of  $\sigma_2$ . As shown, the solution is dominated by the amplitude  $a_2$  corresponding to the motion of pendulum  $P_2$ . The motion of pendulum  $P_1$  is of interest in our case because it is directly related to the energy generation. Figure 4.2 shows that for certain values of the rotation speed the energy of the system is completely transferred to the pendulum  $P_2$ , which is not suitable to our application. In this figure dashed curves indicate unstable solutions, while solid curves indicate stable ones.

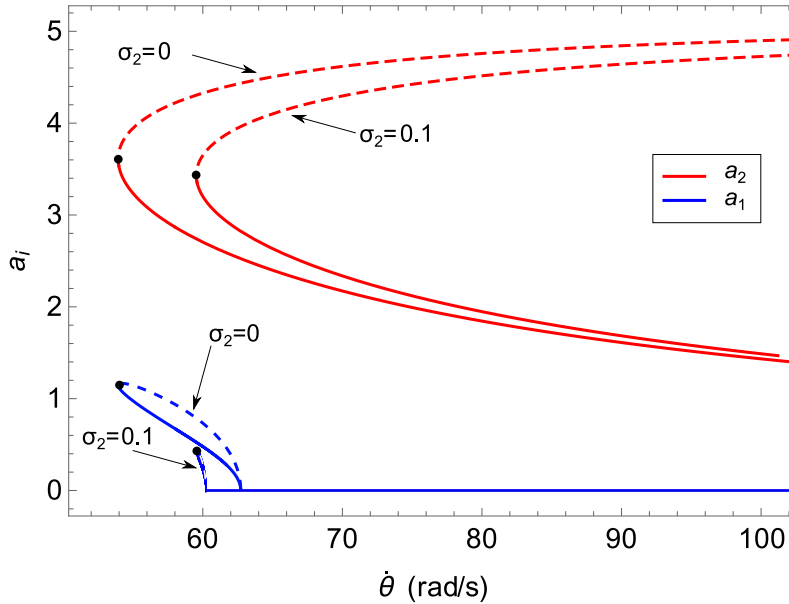


Figure 4.2: Wheel rotation speed effect on the solutions  $a_1$  and  $a_2$  of pendulums  $P_1$  and  $P_2$ , for  $\sigma_1 = 0$ .

As we vary the value of  $\sigma_1$  to  $-0.1$ , the amplitudes are increased as shown in Figure 4.3.  $a_1$  is particularly increased, however, the critical value of the rotation at which the amplitude goes to zero is the same as the previous case.

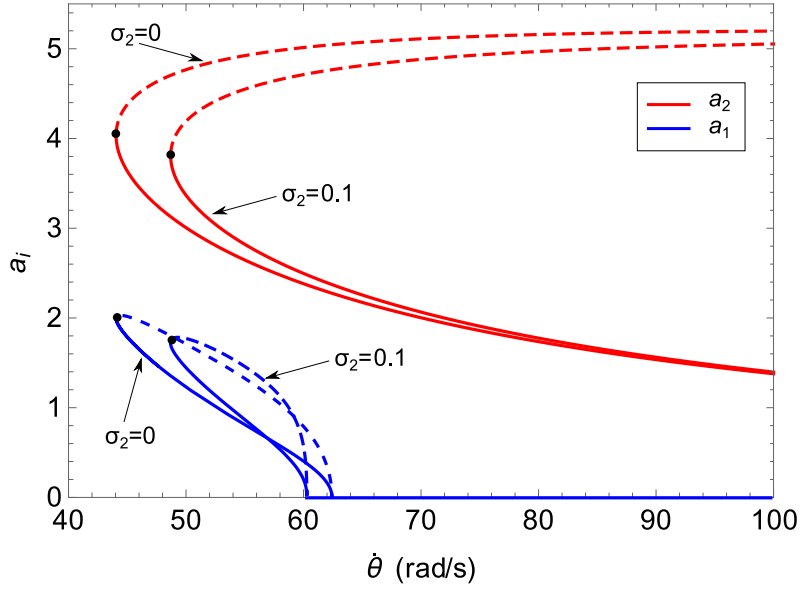


Figure 4.3: Wheel rotation speed effect on the solutions  $a_1$  and  $a_2$  of pendulums  $P_1$  and  $P_2$ , for  $\sigma_1 = -0.1$ .

A further variation of the value of  $\sigma_1$  to  $-1$  qualitatively change the shape of the curves as depicted by Figure 4.4. It is also observed an additional increase of the amplitudes  $a_1$  and  $a_2$ . The critical rotation speed is kept unchanged regarding the zero amplitude response of  $P_2$ .

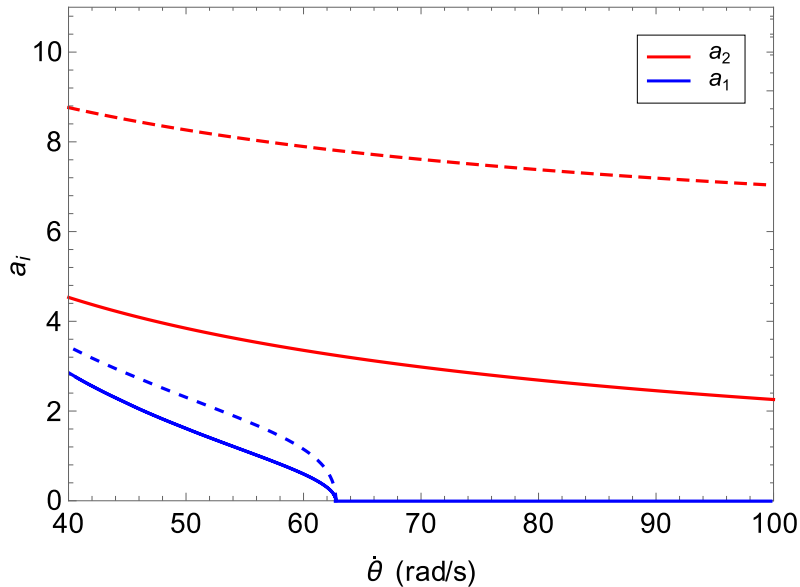


Figure 4.4: Wheel rotation speed effect on the solutions  $a_1$  and  $a_2$  of pendulums  $P_1$  and  $P_2$ , for  $\sigma_1 = -1$  and  $\sigma_2 = 0$ .

### 4.6.1.2 DESIGN 2

For the second design, presented in Table 4.1, where large small radial position of the pendulum is required to obtain the parametric resonance condition, the influence of the rotation speed of the wheel are shown in Figures 4.5 and 4.6 for  $\sigma_2 = 0$  and  $\sigma_2 = 2$ , respectively.

For  $\sigma_1 = 1$  and  $\sigma_2 = 0$ , Figure 4.5 depicts the influence of the rotation speed on the amplitudes  $a_1$  and  $a_2$ . As shown all the obtained solution are unstable for a large range of rotation speeds.

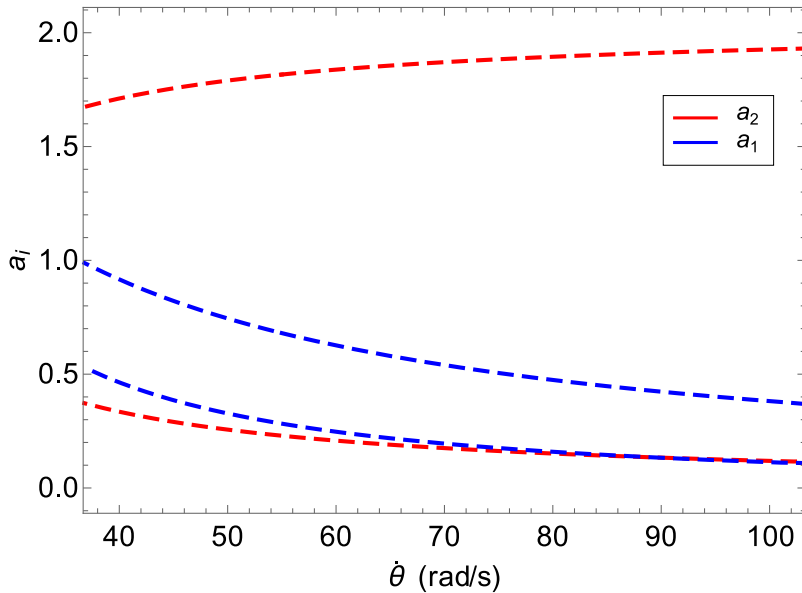


Figure 4.5: Wheel rotation speed effect on the solutions  $a_1$  and  $a_2$  of pendulums  $P_1$  and  $P_2$ , for  $\sigma_1 = 1$  and  $\sigma_2 = 0$ .

For  $\sigma_1 = 1$  and  $\sigma_2 = 2$ , Figure 4.6 shows that a new set of branches are visible for the amplitude  $a_1$ . At high rotation speeds, one of these branches provides a set of stable solutions.

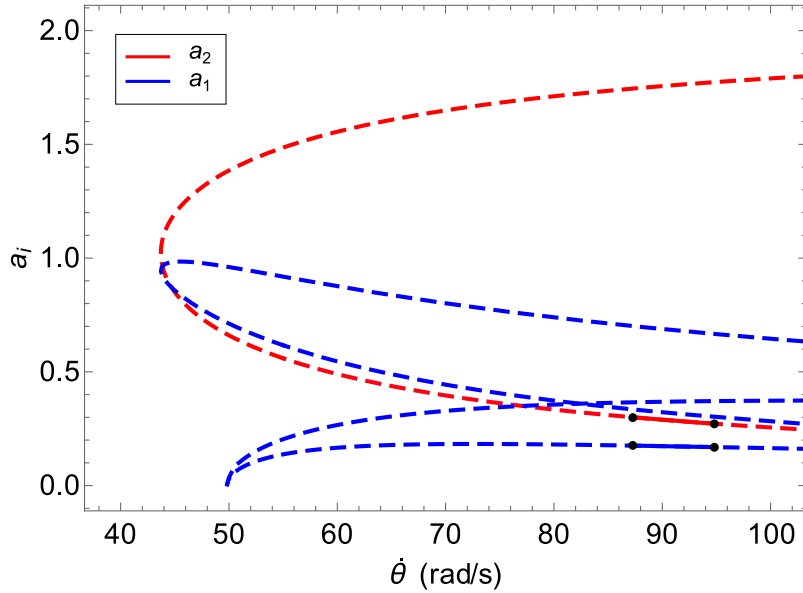


Figure 4.6: Wheel rotation speed effect on the solutions  $a_1$  and  $a_2$  of pendulums  $P_1$  and  $P_2$ , for  $\sigma_1 = 1$  and  $\sigma_2 = 2$ .

#### 4.6.2 FREQUENCY RESPONSE OF THE DEVICE

The frequency response curves can be obtained by varying the detuning parameters  $\sigma_1$  and  $\sigma_2$  independently for both designs. As stated in the previous section, we seek large amplitude  $a_1$  of the pendulum  $P_1$ . The stability of the solution is also shown in the following figures.

##### 4.6.2.1 DESIGN 1

For Design 1, described in Table 4.1, we test the influence of the detuning parameters  $\sigma_1$  and  $\sigma_2$  respectively in Figures 4.7 and 4.8.

In Figure 4.7 it is shown that the amplitude  $a_1$  is only nonzero for small values of  $\sigma_2$ . Here,  $\sigma_1 = -1$  and  $\dot{\theta} = 55$  rad/s. One can conclude that the major part of the energy is transferred to the amplitude  $a_2$ .

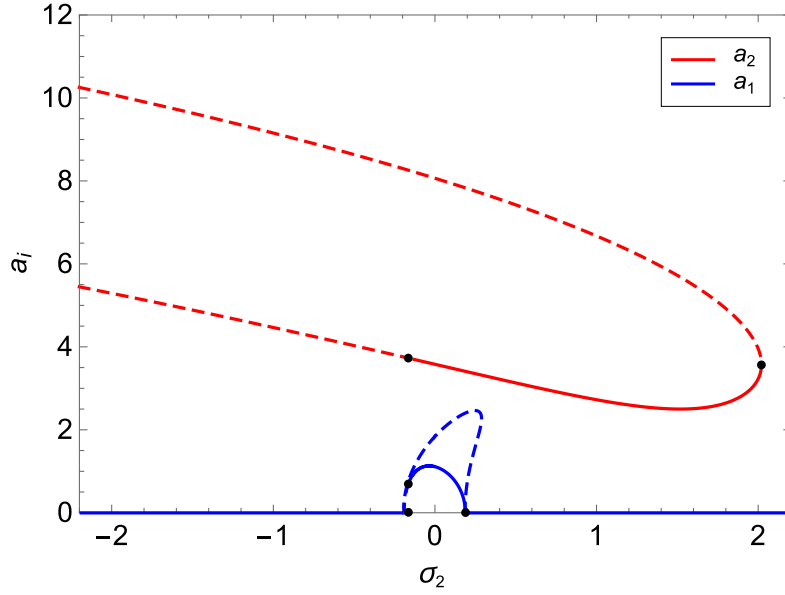


Figure 4.7: Influence of the detuning parameter  $\sigma_2$  on the solutions  $a_1$  and  $a_2$  of pendulums  $P_1$  and  $P_2$ , for  $\sigma_1 = -1$  and  $\dot{\theta} = 55$  rad/s.

When the influence of the detuning parameter  $\sigma_1$  is of interest, the response is shown to be increased, in Figure 4.8, if  $\sigma_1$  has negative values. A stable branch is also obtained for all negative values of  $\sigma_1$ .

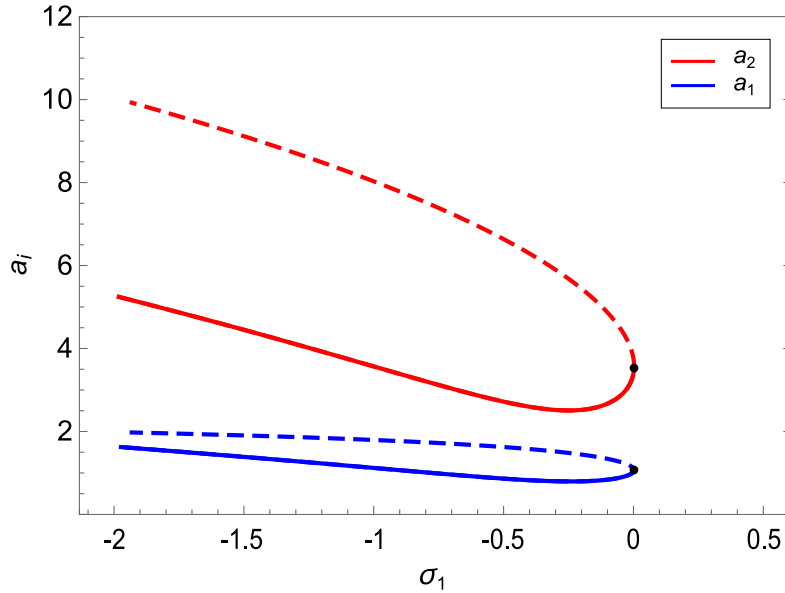


Figure 4.8: Influence of the detuning parameter  $\sigma_1$  on the solutions  $a_1$  and  $a_2$  of pendulums  $P_1$  and  $P_2$ , for  $\sigma_2 = 0$  and  $\dot{\theta} = 55$  rad/s.

#### 4.6.2.2 DESIGN 2

For the second design, the detuning parameters are also varied so that their influence is determined over the amplitude of the responses. In Figure 4.9,  $\sigma_2$  is varied when  $\sigma_1 = 0.1$  and  $\dot{\theta} = 55 \text{ rad/s}$ . The figure depicts clearly that for negative values of  $\sigma_2$  smaller than  $-2$ , a set of stable solution exist where the amplitude  $a_1$  is higher than  $a_2$ . This is not the case of Design 1 where the amplitude  $a_2$  is always higher.

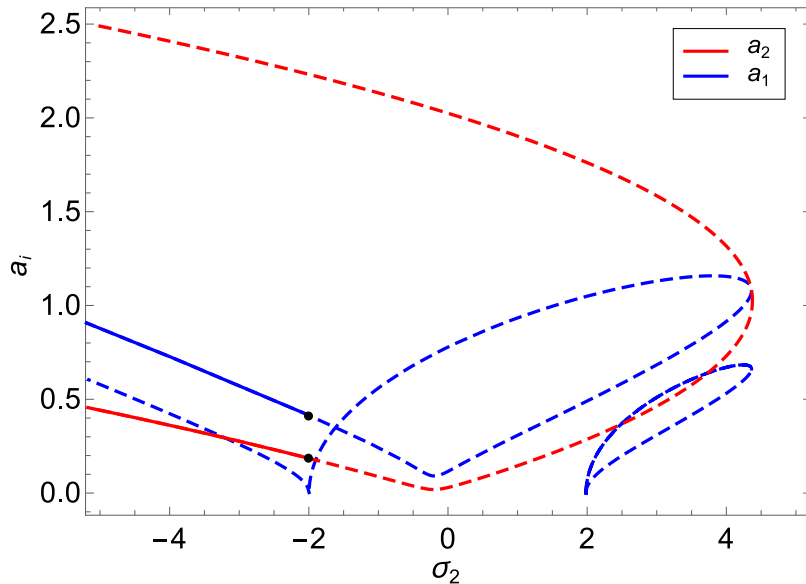


Figure 4.9: Influence of the detuning parameter  $\sigma_2$  on the solutions  $a_1$  and  $a_2$  of pendulums  $P_1$  and  $P_2$ , for  $\sigma_1 = 0.1$  and  $\dot{\theta} = 55 \text{ rad/s}$ .

In Figure 4.10, we try to increase the value of  $\sigma_1$  and keep the same rotation speed. As shown, the stable set of solution is still visible for negative values of  $\sigma_2$ . Also in this case the amplitude  $a_1$  is higher than  $a_2$ , even if its value is lowered compared to the previous case.

Concerning the variation of  $\sigma_1$ , two different case are simulated here: first when  $\sigma_1 = 1$  and  $\dot{\theta} = 55 \text{ rad/s}$ , shown in Figure 4.11, and second when  $\sigma_1 = -3$  and  $\dot{\theta} = 55 \text{ rad/s}$ , shown in Figure 4.12. For Figure 4.11 all solutions are unstable despite the large variation of  $\sigma_1$ . On the other hand in Figure 4.12, large stable branches are visible for positive as well as negative values of  $\sigma_1$ . Also in these cases, generally, the obtained amplitudes are lower than those obtained in Design 1.

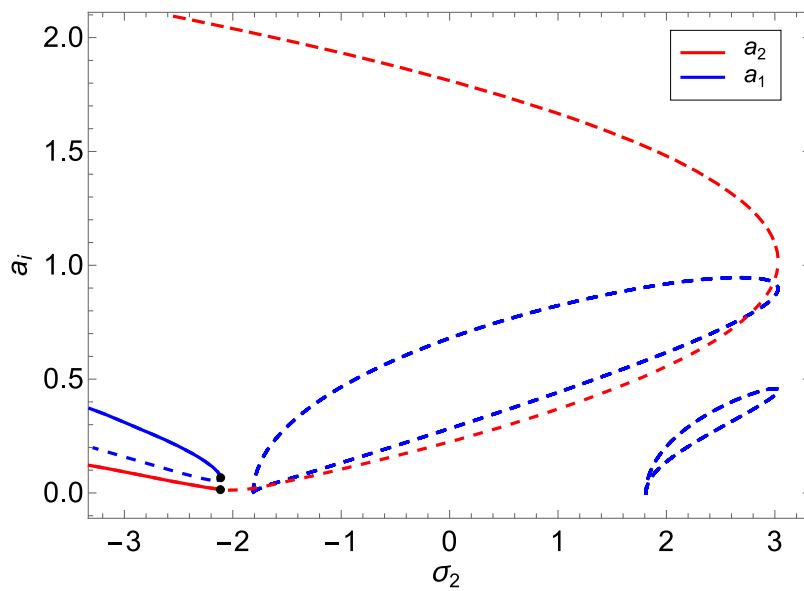


Figure 4.10: Influence of the detuning parameter  $\sigma_2$  on the solutions  $a_1$  and  $a_2$  of pendulums  $P_1$  and  $P_2$ , for  $\sigma_1 = 1$  and  $\dot{\theta} = 55$  rad/s.

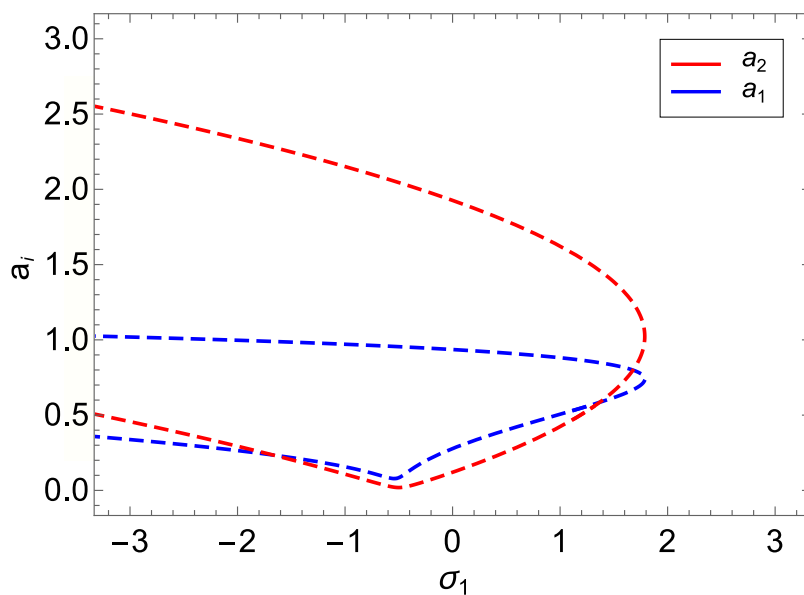


Figure 4.11: Influence of the detuning parameter  $\sigma_1$  on the solutions  $a_1$  and  $a_2$  of pendulums  $P_1$  and  $P_2$ , for  $\sigma_2 = 1$  and  $\dot{\theta} = 55$  rad/s.

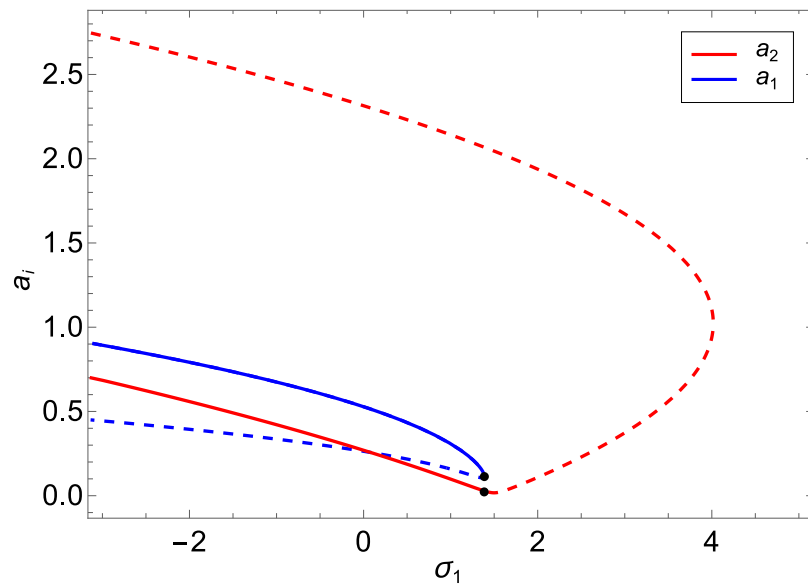


Figure 4.12: Influence of the detuning parameter  $\sigma_1$  on the solutions  $a_1$  and  $a_2$  of pendulums  $P_1$  and  $P_2$ , for  $\sigma_2 = -3$  and  $\dot{\theta} = 55$  rad/s.

# GENERAL CONCLUSION AND FUTURE WORKS

## GENERAL CONCLUSION

In this thesis, we had to design and model a pendulum-based energy harvesting system. The pendulum, considered to be an exciter for an electric DC generator (electromagnetic transducer), is used as an energy harvester for Tire Pressure Monitoring Systems, using the kinetic energy due to the rotation of the wheel as input energy.

Thus, for a pendulum mounted inside a tire, important centrifugal forces induced due to the rotation of the rim, constrains the pendulum to a radial fixed position, making it useless for energy harvesting applications. The challenge was to find the appropriate design and configuration for such system to be still useful at large broadband rotation speeds.

We started by presenting and analyzing four pendulum designs: simple pendulum, double pendulums, simple pendulum with nonparallel axis and Rott's pendulum, while they are mounted in a rotating wheel. The equation of motion of each design are derived and solved numerically. The transient behavior were deduced and the harvested energy estimated and compared to each other. The time response of the angular position and angular velocity were calculated for different damping coefficients and initial conditions. The RMS value of the angular velocity is used to estimate the harvested energy. We had noticed that the RMS value depends on the initial conditions and it reaches its highest value for a simple pendulum with parallel axis when the initial condition is the farthest from the steady state position.

As a second step, we designed, fabricated and putted into experiment three pendulum designs: simple pendulum, double pendulum and Rott's pendulum. The electromagnetic generator in which pendulums were mounted was characterized independently. The torque developed at the generator's shaft and the generated power were estimated using a direct driving method. We found that the generated torque is proportional to the rotation speed of the shaft. This proportionality was also validated experimentally. The optimum load resistance for power output of the generator was measured equal to 59 Ohms. The

resonance frequency of each pendulum was also measured by the mean of laser vibrometer in order to characterize it.

The test bench which simulates the behavior of a car rim was designed and fabricated. The solution for the steady-state behavior of each pendulum, generated at angular velocity for different rotation speeds, was experimentally tested. We noticed that three different regimes are present: oscillations around the vertical axis, aperiodic oscillations and oscillations around the radial axis. The aperiodic regime gives better output voltage for each pendulum and the double pendulum gives the better generated energy.

Then, a half-sine input function was used to record the transient output voltage generated for different initial positions of the disk for each pendulum. The RMS value was calculated. For each pendulum, a better RMS values were measured when  $\theta = \pi$ . Also in this case of study, the double pendulum gives better results for a majority of the tested initial conditions.

Finally, an analytical analysis is proposed to analyze the steady state response under constant rotation speeds, because it represents a non negligible part of the regime of motion of the wheels. The method of multiple scales is applied for the equations of motion governing the motion of the Rott's pendulum when small oscillations are assumed around the radial positions. We deduced that, for the two proposed sets of geometrical dimensions, parametric resonance of the first and second modes while two to one internal resonance is satisfied can be achieved. in both cases, the analytically derived resonance conditions, showed that large amplitude of motions can be achieved if a critical value of the rotation speed is reached. However, if the speed is further increase the amplitude is again highly reduced. In fact, the treated case is specific to the TPMS case because the rotation speed in this case is at the same time the frequency excitation force and the amplitude of the stabilizing force represented here by the centrifugal force.

## FUTURE WORKS

This dissertation proposed several issues related to energy harvesting in TPMS using pendulums. It was also shown that key questions remain to be answered:

- Since it was demonstrated that transient response of the pendulum can represent the larger part of the harvested energy from rotating wheels. This issue should be investigated for wheels under real utilization conditions in order to understand the impact of randomly varying rotation on the performance of the harvester.

- For steady state behavior a lot of investigation needs to be done to overcome the influence of the centrifugal force that drastically reduces the amount of the harvested energy. A good idea is may be to consider rotating solutions that can be realized at lower speeds and that the solution can survive high rotation speeds under frequency-locking phenomena.
- Other type of pendulums should be investigated where elastic elements can be integrated to reinforce the transient response amplitude and increase the harvested energy.
- Some amelioration can be done to the way the rotation of the pendulum is transmitted to the generator. For example, a gear train can be used to increase the output rotation speed from the pendulum. Also, a freewheel mechanism can be added to the rotation to store elastic energy into an helical spring. A releasr mechsnism is activated once the spring is completely compressed. It was proved that such a mechanism reduces energy leakage through damping.



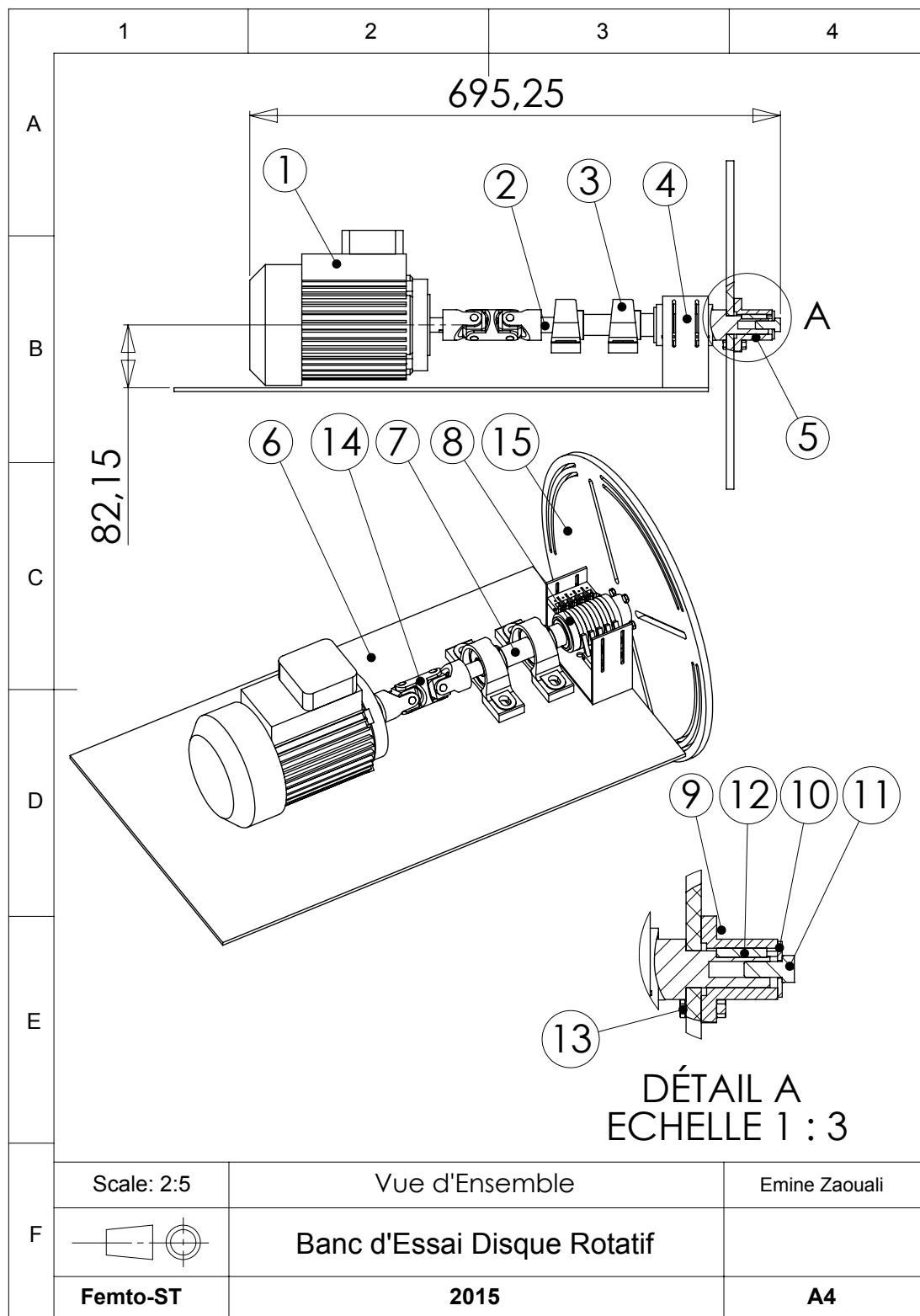
# Appendices

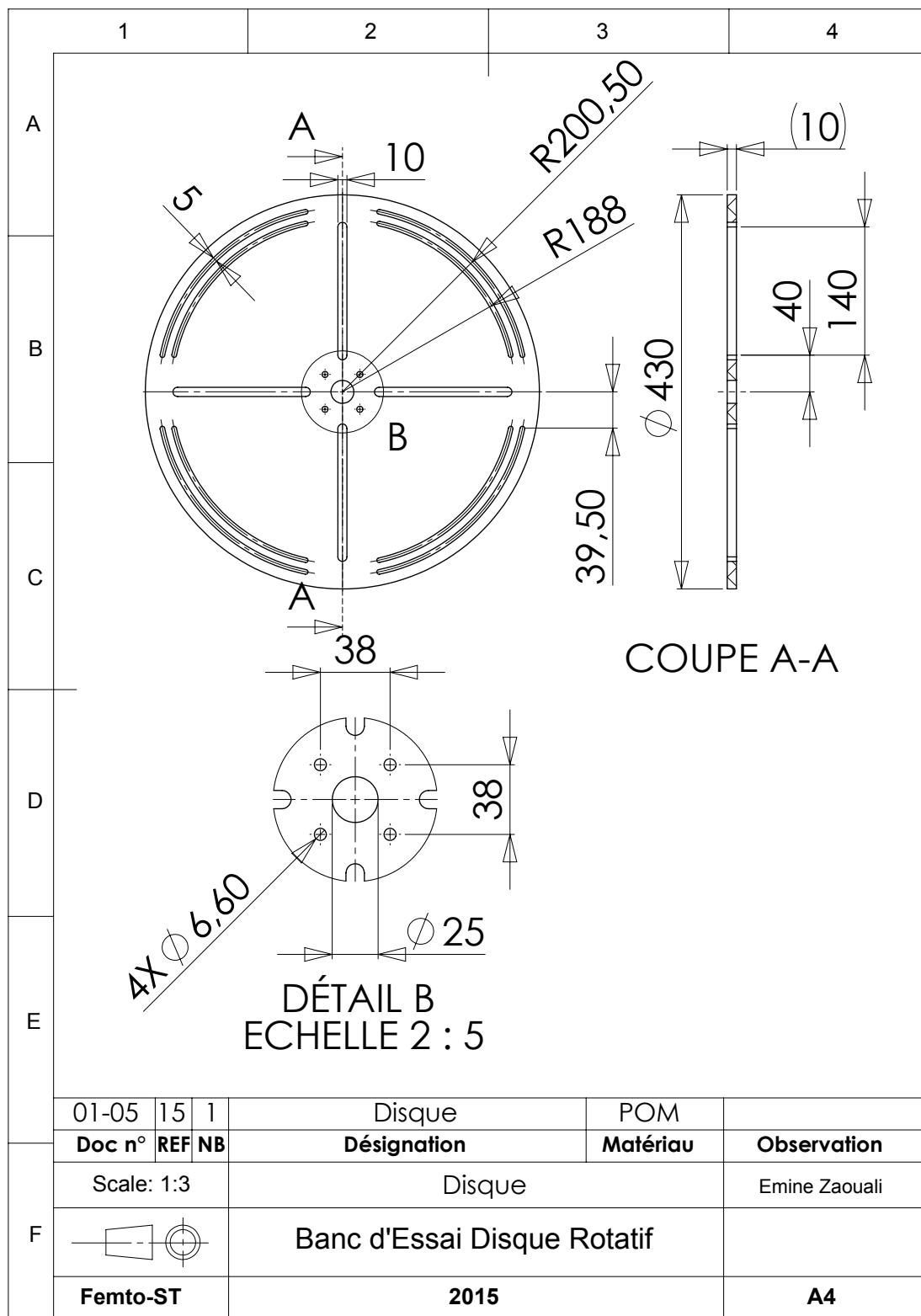


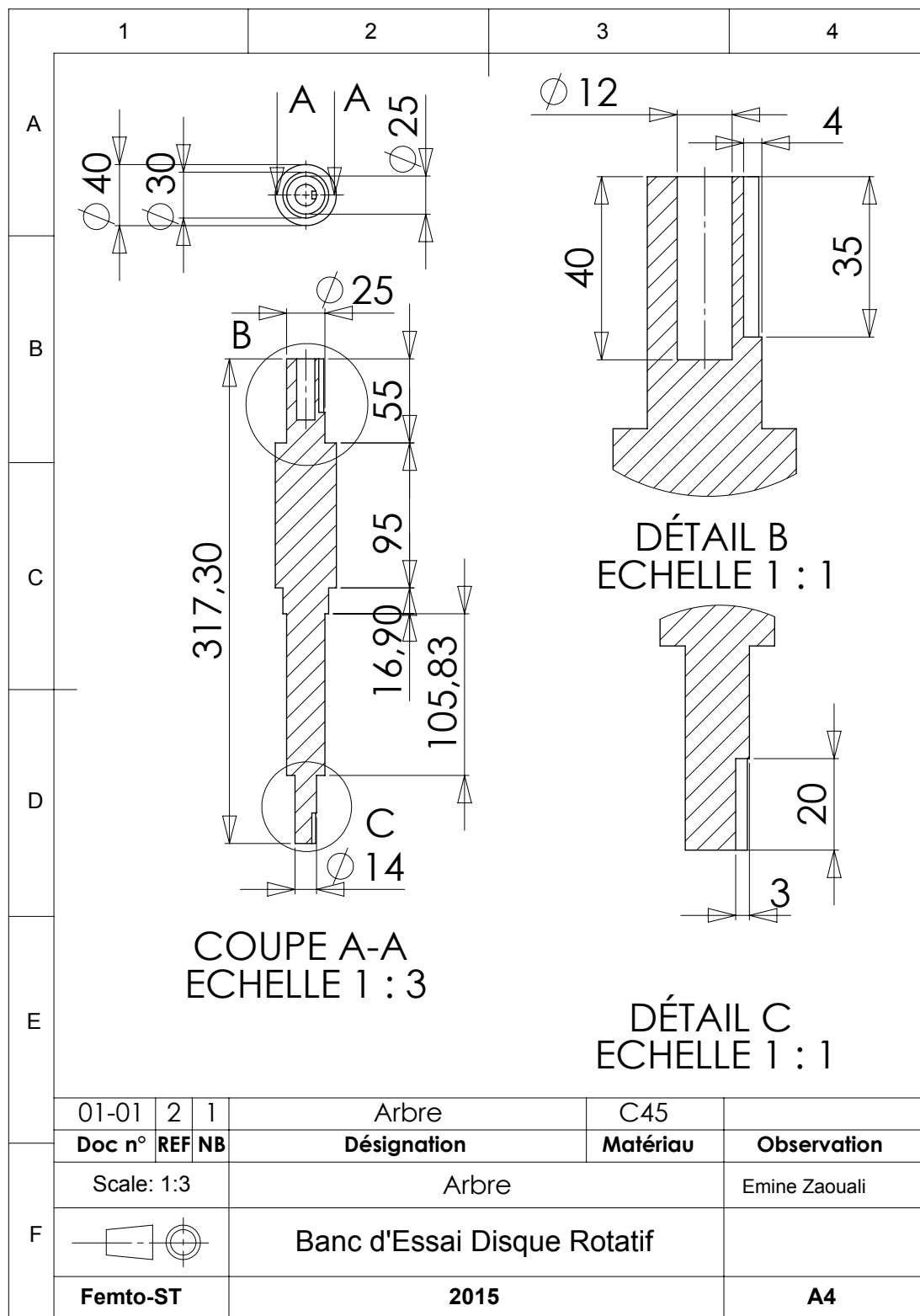
# A

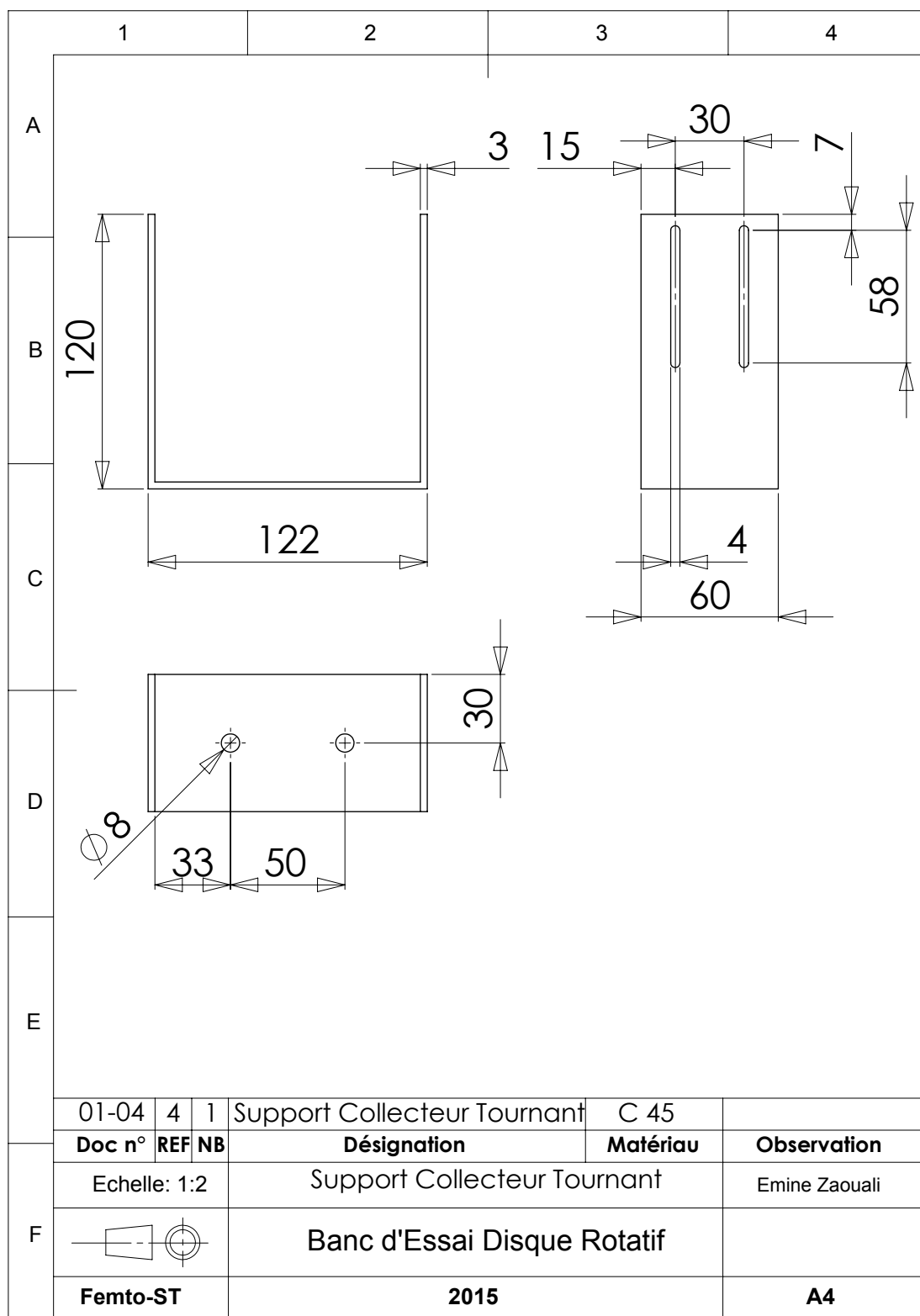
## LAYOUTS OF THE TEST BENCH

LAYOUTS OF THE TEST BENCH

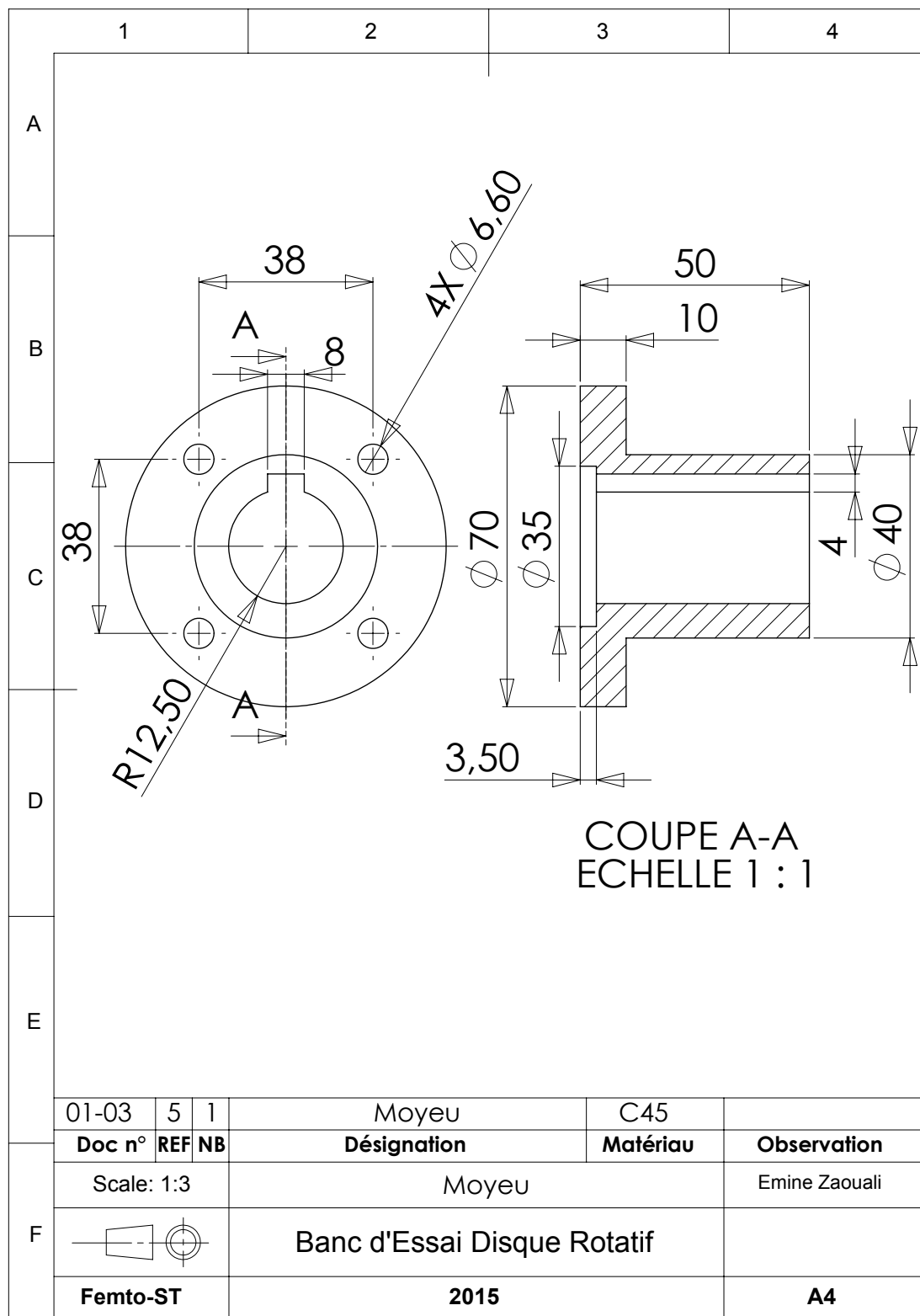


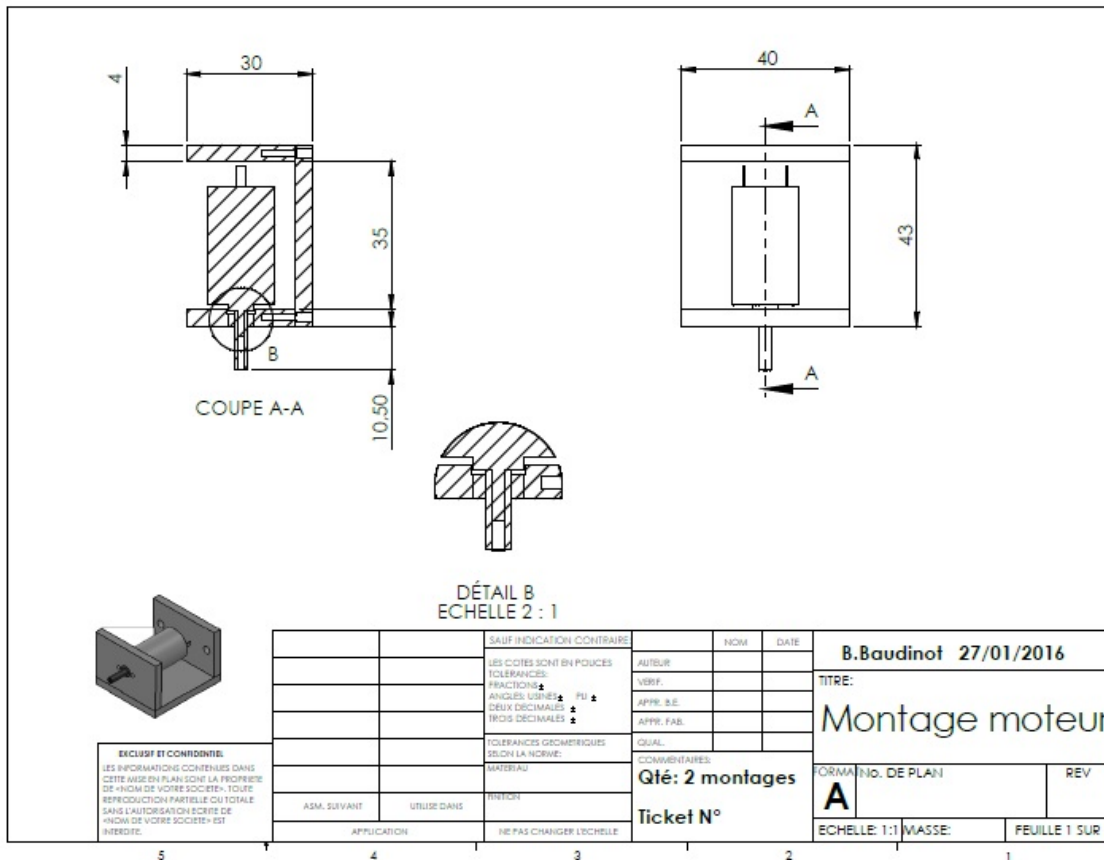






LAYOUTS OF THE TEST BENCH







## BIBLIOGRAPHY

- [1] CFR. Federal motor vehicle safety standards; tire pressure monitoring systems; controls and displays; final rule, 2002. Accessed: 2018-06-06.
- [2] European Conference of Ministers of Transport and International Energy Agency. *Making cars more fuel efficient: technology for real improvements on the road*. OECD, 2005.
- [3] Ockert van Schoor, Johannes L van Niekerk, and B Grobbelaar. Mechanical failures as a contributing cause to motor vehicle accidents—south africa. *Accident Analysis & Prevention*, 33(6):713–721, 2001.
- [4] James W Mcdonnell. Tire pressure indicating system, December 8 1936. US Patent 2,063,452.
- [5] Günter Leister. Tire pressure monitoring systems. In *Passenger Car Tires and Wheels*, pages 243–254. Springer, 2018.
- [6] Victor Underberg, Thomas Roscher, Frank Jenne, Predrag Pucar, and Jörg Sturmhoebel. Tire pressure monitoring systems. *Encyclopedia of Automotive Engineering*, 2014.
- [7] Frost and Sullivan. www.frost.com, 2016. Accessed: 2016-04-27.
- [8] National Highway Traffic Safety Administration. Transportation recall enhancement, accountability, and documentation, 2002. Accessed: 2018-06-06.
- [9] European Environment Agency European Parliament. Approval requirements for the general safety of motor vehicles, 2009. Accessed: 2018-06-06.
- [10] Tom J Kazmierski and Steve Beeby. *Energy harvesting systems*. Springer, 2014.
- [11] Olivier Hersistent, David Boswarthick, and Omar Elloumi. *The internet of things: Key applications and protocols*. John Wiley & Sons, 2011.

## BIBLIOGRAPHY

---

- [12] Hongwen Sun, Minqi Yin, Wangtong Wei, Jiacheng Li, Haibin Wang, and Xin Jin. Mems based energy harvesting for the internet of things: a survey. *Microsystem Technologies*, pages 1–17, 2018.
- [13] Milica Pejanović Đurišić, Zhilbert Tafa, Goran Dimić, and Veljko Milutinović. A survey of military applications of wireless sensor networks. In *Embedded Computing (MECO), 2012 Mediterranean Conference on*, pages 196–199. IEEE, 2012.
- [14] Ian F Akyildiz and Mehmet Can Vuran. *Wireless sensor networks*, volume 4. John Wiley & Sons, 2010.
- [15] Waltenegus Dargie and Christian Poellabauer. *Fundamentals of wireless sensor networks: theory and practice*. John Wiley & Sons, 2010.
- [16] Delphine Christin, Andreas Reinhardt, Parag S Mogre, Ralf Steinmetz, et al. Wireless sensor networks and the internet of things: selected challenges. *Proceedings of the 8th GI/ITG KuVS Fachgespräch Drahtlose sensornetze*, pages 31–34, 2009.
- [17] Marco Tartagni, Marc Belleville, Eugenio Cantatore, Herve Fanet, Paolo Fiorini, Pierre Nicole, Marcel Pelgrom, Christian Piguet, Robert Hahn, Chris Van Hoof, et al. Energy autonomous systems: Future trends in devices, technology, and systems. *Cluster for Application and Technology Research in Europe on Nanoelectronics (CATRENE) Report*, 2009.
- [18] CB Williams and Rob B Yates. Analysis of a micro-electric generator for microsystems. *Sensors and Actuators A: Physical*, 52(1-3):8–11, 1996.
- [19] Ahmed Jemai, Fehmi Najar, Moez Chafra, and Zoubeida Ounaies. Modeling and parametric analysis of a unimorph piezocomposite energy harvester with interdigitated electrodes. *Composite Structures*, 135:176–190, 2016.
- [20] Alper Erturk and Daniel J Inman. An experimentally validated bimorph cantilever model for piezoelectric energy harvesting from base excitations. *Smart materials and structures*, 18(2):025009, 2009.
- [21] Philippe Basset, Dimitri Galayko, Francesco Cottone, Raphaël Guillemet, Elena Blokhina, Frédéric Marty, and Tarik Bourouina. Electrostatic vibration energy

- harvester with combined effect of electrical nonlinearities and mechanical impact. *Journal of Micromechanics and Microengineering*, 24(3):035001, 2014.
- [22] Philippe Basset, Dimitri Galayko, A Mahmood Paracha, Frédéric Marty, Andrii Dudka, and Tarik Bourouina. A batch-fabricated and electret-free silicon electrostatic vibration energy harvester. *Journal of Micromechanics and Microengineering*, 19(11):115025, 2009.
  - [23] Soo Jin Adrian Koh, Christoph Keplinger, Tiefeng Li, Siegfried Bauer, and Zhigang Suo. Dielectric elastomer generators: How much energy can be converted? *IEEE/ASME Transactions on mechatronics*, 16(1):33–41, 2011.
  - [24] E Zaouali, F Najar, and K Mrabet. Dielectric elastomer as active material in membranes for vibration-based energy harvesting. In *MEDYNA 2013, 1st Euro-Mediterranean Conference on Structural Dynamics and Vibroacoustics, 23-25 Apr, Marrakech, Morocco*, 2014.
  - [25] Shashank Priya and Daniel J Inman. *Energy harvesting technologies*, volume 21. Springer, 2009.
  - [26] Issam Abed, Najib Kacem, Noureddine Bouhaddi, and Mohamed Lamjed Bouazizi. Multi-modal vibration energy harvesting approach based on nonlinear oscillator arrays under magnetic levitation. *Smart Materials and Structures*, 25(2):025018, 2016.
  - [27] CR Bowen and MH Arafa. Energy harvesting technologies for tire pressure monitoring systems. *Advanced Energy Materials*, 5(7), 2015.
  - [28] Stefano Tornincasa, Maurizio Repetto, Elvio Bonisoli, and Francesco Di Monaco. Energy harvester for vehicle tires: Nonlinear dynamics and experimental outcomes. *Journal of Intelligent Material Systems and Structures*, 23(1):3–13, 2012.
  - [29] Ali E Kubba and Kyle Jiang. A comprehensive study on technologies of tyre monitoring systems and possible energy solutions. *Sensors*, 14:10306–10345, 2014.
  - [30] Federico Mancosu, Giuseppe Matrascia, and Diego Villa. Vehicle tire and system for generating electrical energy in the tire, January 31 2006. US Patent 6,992,423.
  - [31] John David Adamson and George Phillips O'brien. System for generating electric power from a rotating tire's mechanical energy using reinforced piezoelectric materials, April 27 2004. US Patent 6,725,713.

## BIBLIOGRAPHY

---

- [32] J Lee, S Kim, J Oh, and B Choi. A self-powering system based on tire deformation during driving. *International Journal of Automotive Technology*, 13(6):963–969, 2012.
- [33] DA Van den Ende, HJ Van de Wiel, WA Groen, and S Van der Zwaag. Direct strain energy harvesting in automobile tires using piezoelectric pzt–polymer composites. *Smart materials and structures*, 21(1):015011, 2011.
- [34] Noaman Makki and Remon Pop-Iliev. Piezoelectric power generation in automotive tires. *Proceedings of the Smart Materials & Structures/NDT in Aerospace/NDT in Canada*, 2011.
- [35] Ryosuke Matsuzaki, Naoki Hiraoka, Akira Todoroki, and Yoshihiro Mizutani. Analysis of applied load estimation using strain for intelligent tires. *Journal of Solid Mechanics and Materials Engineering*, 4(10):1496–1510, 2010.
- [36] Francesco Braghin, M Brusarosco, Federico Cheli, Alfredo Cigada, S Manzoni, and F Mancosu. Measurement of contact forces and patch features by means of accelerometers fixed inside the tire to improve future car active control. *Vehicle System Dynamics*, 44:3–13, 2006.
- [37] Shad Roundy. Energy harvesting for tire pressure monitoring systems: design considerations. *Proceedings of Power MEMS+ microMEMS, Sendai, Japan*, pages 9–12, 2008.
- [38] Shad Roundy and Paul K Wright. A piezoelectric vibration based generator for wireless electronics. *Smart Materials and structures*, 13(5):1131, 2004.
- [39] Shunong Jiang, Xianfang Li, Shaohua Guo, Yuantai Hu, Jiashi Yang, and Qing Jiang. Performance of a piezoelectric bimorph for scavenging vibration energy. *Smart Materials and Structures*, 14(4):769, 2005.
- [40] Jyoti Ajitsaria, Song-Yul Choe, D Shen, and DJ Kim. Modeling and analysis of a bimorph piezoelectric cantilever beam for voltage generation. *Smart Materials and Structures*, 16(2):447, 2007.
- [41] Dongna Shen, Jung-Hyun Park, Jyoti Ajitsaria, Song-Yul Choe, Howard C Wikle III, and Dong-Joo Kim. The design, fabrication and evaluation of a mems pzt cantilever with an integrated si proof mass for vibration energy harvesting. *Journal of Micromechanics and Microengineering*, 18(5):055017, 2008.

- [42] Kanwar Bharat Singh, Vishwas Bedekar, Saied Taheri, and Shashank Priya. Piezoelectric vibration energy harvesting system with an adaptive frequency tuning mechanism for intelligent tires. *Mechatronics*, 22(7):970–988, 2012.
- [43] R Elfrink, S Matova, C De Nooijer, M Jambunathan, M Goedbloed, J Van de Molengraft, Vullers Pop, RJM Vullers, M Renaud, and R Van Schaijk. Shock induced energy harvesting with a mems harvester for automotive applications. In *Electron Devices Meeting (IEDM), 2011 IEEE International*, pages 29–5. IEEE, 2011.
- [44] Rob van Schaijk, Rene Elfrink, Valer Pop, and Ruud Vullers. Energy harvesting for self powered sensor systems. *SASIMI 2012 Proceedings*, pages 141–146, 2012.
- [45] R van Schaijk, R Elfrink, J Oudenhoven, V Pop, Z Wang, and M Renaud. A mems vibration energy harvester for automotive applications. In *Smart Sensors, Actuators, and MEMS VI*, volume 8763, page 876305. International Society for Optics and Photonics, 2013.
- [46] M Renaud, Z Wang, M Jambunathan, S Matova, R Elfrink, M Rovers, M Goedbloed, C De Nooijer, RJM Vullers, and R van Schaijk. Improved mechanical reliability of mems piezoelectric vibration energy harvesters for automotive applications. In *Micro Electro Mechanical Systems (MEMS), 2014 IEEE 27th International Conference on*, pages 568–571. IEEE, 2014.
- [47] Carmen Chicone and ZC Feng. Power harvesting from rotation?. *European Journal of Physics*, 29(5):1115–1120, 2008.
- [48] Shad Roundy, Janusz Bryzek, Curtis Ray, Michael Malaga, and David L Brown. Power generation utilizing tire pressure changes, August 28 2007. US Patent 7,260,984.
- [49] Tien-Tsai Huang. Tire pressure indicator including pressure gauges that have a self-generating power capability, January 16 2001. US Patent 6,175,302.
- [50] Kuok H Mak, Stewart McWilliam, and Atanas A Popov. Piezoelectric energy harvesting for tyre pressure measurement applications. *Proceedings of the Institution of Mechanical Engineers, Part D: Journal of Automobile Engineering*, 227(6):842–852, 2013.

## BIBLIOGRAPHY

---

- [51] Qinglong Zheng and Yong Xu. Asymmetric air-spaced cantilevers for vibration energy harvesting. *Smart materials and Structures*, 17(5):055009, 2008.
- [52] Ali E Kubba and Kyle Jiang. Efficiency enhancement of a cantilever-based vibration energy harvester. *Sensors*, 14(1):188–211, 2013.
- [53] Lei Gu and Carol Livermore. Compact passively self-tuning energy harvesting for rotating applications. *Smart materials and structures*, 21(1):015002, 2011.
- [54] Yu-Jen Wang, Chung-De Chen, and Cheng-Kuo Sung. Design of a frequency-adjusting device for harvesting energy from a rotating wheel. *Sensors and Actuators A: Physical*, 159(2):196–203, 2010.
- [55] Yu-Jen Wang, Chung-De Chen, Cheng-Kuo Sung, and Chien Li. Natural frequency self-tuning energy harvester using a circular halbach array magnetic disk. *Journal of Intelligent Material Systems and Structures*, 23(8):933–943, 2012.
- [56] Yu-Jen Wang and Hao-Yu Lin. Design of weighted type energy harvester based on analysis of a wireless tire pressure monitor system. In *Industrial Electronics Society, IECON 2014-40th Annual Conference of the IEEE*, pages 5300–5306. IEEE, 2014.
- [57] Yu-Jen Wang, Chung-De Chen, and Cheng-Kuo Sung. System design of a weighted-pendulum-type electromagnetic generator for harvesting energy from a rotating wheel. *IEEE/ASME Transactions on Mechatronics*, 18(2):754–763, 2013.
- [58] Kyoung Il Lee, Byung Jik Lim, Seong Hyun Kim, and Yongtaek Hong. Energy harvesting by rotation of wheel for tire monitoring system. In *Sensors, 2012 IEEE*, pages 1–4. IEEE, 2012.
- [59] Shad Roundy and Jeffry Tola. Energy harvester for rotating environments using offset pendulum and nonlinear dynamics. *Smart Materials and Structures*, 23(10):105004, 2014.
- [60] Tzern T Toh, Anshu Bansal, Guodong Hong, Paul D Mitcheson, Andrew S Holmes, and Eric M Yeatman. Energy harvesting from rotating structures. In *Proceeding of PowerMEMS 2007, Freiburg, Germany*, 28-29 Nov, pages 327–330, 2007.
- [61] Tzern T Toh, Paul D Mitcheson, and Eric M Yeatman. A gravitational torque micro-generator for self-powered sensing. In *Proc. Micromechanics Europe, Guimaraes, Portugal, 16-18 Sept*, pages 341–344, 2007.

- [62] Tzern T Toh, Paul D Mitcheson, Andrew S Holmes, and Eric M Yeatman. A continuously rotating energy harvester with maximum power point tracking. *Journal of Micromechanics and Microengineering*, 18(10):104008, 2008.
- [63] Tzern T Toh, Paul D Mitcheson, and Eric M Yeatman. Continuously rotating energy harvester with improved power density. In *Proceeding of PowerMEMS 2008 and microEMS2008, Sendai, Japan, Nov 9-12*, pages 221–224, 2008.
- [64] Tzern T Toh, Paul D Mitcheson, and Eric M Yeatman. Wireless sensor node using a rotational energy harvester with adaptive power conversion. In *Proceeding of PowerMEMS 2009, Washington DC, USA, December 1-4*, pages 273–276, 2009.
- [65] M Amin Karami and Daniel J Inman. Hybrid rotary-translational energy harvester for multi-axis ambient vibrations. In *ASME 2012 Conference on Smart Materials, Adaptive Structures and Intelligent Systems*, pages 739–746. American Society of Mechanical Engineers, 2012.
- [66] M Amin Karami and Daniel J Inman. Nonlinear dynamics of the hybrid rotary-translational energy harvester. In *ASME 2013 Conference on Smart Materials, Adaptive Structures and Intelligent Systems*, pages V002T07A008–V002T07A008. American Society of Mechanical Engineers, 2013.
- [67] Scott D Moss, Genevieve A Hart, Stephen K Burke, and Gregory P Carman. Hybrid rotary-translational vibration energy harvester using cycloidal motion as a mechanical amplifier. *Applied Physics Letters*, 104(3):033506, 2014.
- [68] Michael Flankl, Arda Tüysüz, and Johann W Kolar. Analysis of a watt-range contactless electromechanical energy harvester facing a moving conductive surface. In *Energy Conversion Congress and Exposition (ECCE), 2015 IEEE*, pages 414–420. IEEE, 2015.
- [69] M Febbo, SP Machado, JM Ramirez, and CD Gatti. A low frequency rotational energy harvesting system. In *Journal of Physics: Conference Series*, volume 773, page 012058. IOP Publishing, 2016.
- [70] Richard Watkins. *The Origins of Self-winding Watches 1773 - 1779*. Richard Watkins, 2013.
- [71] M Lossec, B Multon, H Ben Ahmed, C Fredy, F Le Bourhis, and S Moya. Study of a micro-kinetic generator: modelization and optimization of energy conversion.

## BIBLIOGRAPHY

---

- In *Proceeding of the Conférence Conférence Electrotechnique du Future EF 2009, UTC, Compiègne, 24-25 Septembre, 2009.*
- [72] Eric M Yeatman. Energy harvesting from motion using rotating and gyroscopic proof masses. *Proceedings of the Institution of Mechanical Engineers, Part C: Journal of Mechanical Engineering Science*, 222(1):27–36, 2008.
  - [73] CX Lu, CC Wang, CK Sung, and Paul CP Chao. Dynamic analysis of a motion transformer mimicking a hula hoop. *Journal of Vibration and Acoustics*, 133(1):014501, 2011.
  - [74] Paul C-P Chao, CI Shao, CX Lu, and CK Sung. A new energy harvest system with a hula-hoop transformer, micro-generator and interface energy-harvesting circuit. *Microsystem technologies*, 17(5-7):1025–1036, 2011.
  - [75] Lun-De Liao, Paul C-P Chao, Jian-Ting Chen, Wei-Dar Chen, Wei-Hsuan Hsu, Chi-Wei Chiu, and Chin-Teng Lin. A miniaturized electromagnetic generator with planar coils and its energy harvest circuit. *IEEE transactions on magnetics*, 45(10):4621–4627, 2009.
  - [76] Anna Najdecka. *Rotating dynamics of pendula systems for energy harvesting from ambient vibrations*. PhD thesis, University of Aberdeen, 2013.
  - [77] Daniil Yurchenko and Panagiotis Alevras. Parametric pendulum based wave energy converter. *Mechanical Systems and Signal Processing*, 99:504–515, 2018.
  - [78] Tian-Wei Ma, Hui Zhang, and Ning-Shou Xu. A novel parametrically excited non-linear energy harvester. *Mechanical Systems and Signal Processing*, 28:323–332, 2012.
  - [79] Yu Jia, Jize Yan, Kenichi Soga, and Ashwin A Seshia. Parametric resonance for vibration energy harvesting with design techniques to passively reduce the initiation threshold amplitude. *Smart Materials and Structures*, 23(6):065011, 2014.
  - [80] Xianzhi Dai. An vibration energy harvester with broadband and frequency-doubling characteristics based on rotary pendulums. *Sensors and Actuators A: Physical*, 241:161–168, 2016.
  - [81] Sean M Carroll. *From eternity to here: the quest for the ultimate theory of time*. Penguin, 2010.

- [82] R. Signore. *Histoire du pendule*. Collection "Va savoir!". Vuibert, 2011.
- [83] Gregory L Baker and James A Blackburn. *The pendulum: a case study in physics*. Oxford University Press, 2005.
- [84] Ali H Nayfeh and Dean T Mook. *Nonlinear oscillations*. John Wiley & Sons, 2008.
- [85] Richard H Rand. Lecture notes on nonlinear vibrations. In *Dept. Theoretical and Applied Mechanics*. Cornell University, 2012.
- [86] W Garira and SR Bishop. Rotating solutions of the parametrically excited pendulum. *Journal of sound and vibration*, 263(1):233–239, 2003.
- [87] Xu Xu and Marian Wiercigroch. Approximate analytical solutions for oscillatory and rotational motion of a parametric pendulum. *Nonlinear Dynamics*, 47(1-3):311–320, 2007.
- [88] RB Levien and SM Tan. Double pendulum: An experiment in chaos. *American Journal of Physics*, 61(11):1038–1044, 1993.
- [89] MZ Rafat, MS Wheatland, and TR Bedding. Dynamics of a double pendulum with distributed mass. *American Journal of Physics*, 77(3):216–223, 2009.
- [90] Jose Carlos Sartorelli and Walter Lacarbonara. Parametric resonances in a base-excited double pendulum. *Nonlinear dynamics*, 69(4):1679–1692, 2012.
- [91] AM Calvão and Thadeu JP Penna. The double pendulum: a numerical study. *European Journal of Physics*, 36(4):045018, 2015.
- [92] Soumyabrata Maiti, Jyotirmoy Roy, Asok K Mallik, and Jayanta K Bhattacharjee. Nonlinear dynamics of a rotating double pendulum. *Physics Letters A*, 380(3):408–412, 2016.
- [93] Nikolaus Rott. A multiple pendulum for the demonstration of non-linear coupling. *Zeitschrift für angewandte Mathematik und Physik ZAMP*, 21(4):570–582, 1970.
- [94] John Miles. Parametric excitation of an internally resonant double pendulum. *Zeitschrift für angewandte Mathematik und Physik ZAMP*, 36(3):337–345, 1985.
- [95] Janet Becker and John Miles. Parametric excitation of an internally resonant double pendulum, ii. *Zeitschrift für angewandte Mathematik und Physik ZAMP*, 37(5):641–650, 1986.

## BIBLIOGRAPHY

---

- [96] AH Nayfeh. Parametric excitation of two internally resonant oscillators. *Journal of Sound and Vibration*, 119(1):95–109, 1987.
- [97] MJ Clifford and SR Bishop. Rotating periodic orbits of the parametrically excited pendulum. *Physics Letters A*, 201(2-3):191–196, 1995.
- [98] Xu Xu, Marian Wiercigroch, and MP Cartmell. Rotating orbits of a parametrically-excited pendulum. *Chaos, Solitons & Fractals*, 23(5):1537–1548, 2005.
- [99] Bryan Horton, Marian Wiercigroch, and Xu Xu. Transient tumbling chaos and damping identification for parametric pendulum. *Philosophical Transactions of the Royal Society of London A: Mathematical, Physical and Engineering Sciences*, 366(1866):767–784, 2008.
- [100] B Horton, J Sieber, JMT Thompson, and M Wiercigroch. Dynamics of the nearly parametric pendulum. *International journal of non-linear mechanics*, 46(2):436–442, 2011.
- [101] V Vaziri, A Najdecka, and M Wiercigroch. Experimental control for initiating and maintaining rotation of parametric pendulum. *The European Physical Journal Special Topics*, 223(4):795–812, 2014.
- [102] A Najdecka, T Kapitaniak, and M Wiercigroch. Synchronous rotational motion of parametric pendulums. *International Journal of Non-Linear Mechanics*, 70:84–94, 2015.
- [103] Portescap. [www.portescap.com](http://www.portescap.com), 2016. Accessed: 2016-04-27.
- [104] Kay Hameyer and Ronnie JM Belmans. Permanent magnet excited brushed dc motors. *IEEE Transactions on industrial electronics*, 43(2):247–255, 1996.
- [105] Ali H Nayfeh and Balakumar Balachandran. *Applied nonlinear dynamics: analytical, computational, and experimental methods*. John Wiley & Sons, 2008.
- [106] Leonard Meirovitch. *Methods of analytical dynamics*. Courier Corporation, 2010.

## LIST OF FIGURES

1.1	Tire Pressure Monitoring System using a direct approach measurement [5]. . . . .	19
1.2	Schematic diagram of autonomous TPMS powered by an EH. . . . .	21
1.3	Wireless Sensor Networks [15] . . . . .	22
1.4	The qualitative variation of circumferential strain and radial acceleration in a typical tire rolling over a hard surface [27] . . . . .	26
1.5	Typical radial acceleration profile at different speeds of a point in the inner tire liner [28]. . . . .	26
1.6	Energy Harvester as a piezoelectric wire fixed inside the tire [30]. . . . .	27
1.7	Piezo-composite patches EH [31]. . . . .	27
1.8	Mass-spring system EH with limit stoppers [42]. . . . .	28
1.9	Schematic response of the EH during the rotation of the wheel [28]. . . . .	29
1.10	EH with asymmetric air-spaced cantilever [51]. . . . .	30
1.11	Rigid/flexible beams EH system [53]. . . . .	31
1.12	Halbach array magnetic disk proposed by Wang et al. [55]. . . . .	32
1.13	Simple pendulum energy harvester with a disturbed static position [58]. .	32
1.14	Simple pendulum energy harvester with a disturbed static position [58]. .	33
1.15	Two different version of the system proposed by Toh et al. to harvest energy from a rotating shaft [62, 64]. . . . .	34
1.16	Two beams energy harvester for rotating disk [69]. . . . .	35
1.17	18 <sup>th</sup> century pocket watch by Berthoud [70]. . . . .	36
1.18	Modern self-winding mechanism, Lossec et al. [71]. . . . .	36
1.19	Simple pendulum with a moving support. . . . .	38
1.20	Schematic stability diagram of the a system described by Equation 1.6 [86].	40
1.21	Double pendulum with a moving support. . . . .	40
1.22	Rott's pendulum. . . . .	42

## LIST OF FIGURES

---

2.1	Variation of the speed of the vehicle as function of time for a cruising speed $V_0 = 25\text{km/h}$	46
2.2	Simple pendulum design with parallel axis.	48
2.3	Double pendulum system with parallel axes.	49
2.4	Simple pendulum design with non-parallel axis.	50
2.5	Rott's pendulum with parallel axis.	51
2.6	Time response of the angular position $\alpha$ for a simple pendulum with parallel axis for different damping coefficients (Blue curve $c = 0.01$ , Red curve $c = 0.05$ , Grey curve $c = 0.2$ and Green curve $c = 0.5$ ).	54
2.7	Time response of the angular velocity $\dot{\alpha}$ for a simple pendulum with parallel axis for different damping coefficients (Blue curve $c = 0.01$ , Red curve $c = 0.05$ , Grey curve $c = 0.2$ and Green curve $c = 0.5$ ).	55
2.8	Trajectory of the mass point $M$ in the frame $(O, \vec{x}_1, \vec{y}_1, \vec{z}_0)$ for a damping coefficient $c = 0.01$ and $\alpha(0) = -\frac{\pi}{2}$ for a simple pendulum with parallel axis.	55
2.9	RMS values of the angular velocity $\dot{\alpha}_{RMS}$ for a damping coefficient $c = 0.01$ and different initial conditions $\alpha(0)$ for a simple pendulum with parallel axis.	56
2.10	Time response of the angular position $\alpha$ for a double pendulum with parallel axis with different damping coefficients (Blue curve $c_1 = 0.01$ , Red curve $c_1 = 0.05$ , Grey curve $c_1 = 0.2$ and Green curve $c_1 = 0.5$ ), $c_2 = 0.0001$ . $\alpha(0) = -\frac{\pi}{2}$ and $\beta(0) = 0$	57
2.11	Time response of the angular velocity $\dot{\alpha}$ for a double pendulum with parallel axis with different damping coefficients (Blue curve $c_1 = 0.01$ , Red curve $c_1 = 0.05$ , Grey curve $c_1 = 0.2$ and Green curve $c_1 = 0.5$ ), $c_2 = 0.0001$ . $\alpha(0) = -\frac{\pi}{2}$ and $\beta(0) = 0$	57
2.12	Trajectory of the point mass $M$ when $\alpha(0) = -\frac{\pi}{2}$ and $\beta(0) = 0$ for a double pendulum with parallel axes.	58
2.13	RMS values of the angular velocity $\dot{\alpha}_{RMS}$ for a damping coefficient $c = 0.01$ and different initial conditions $\alpha(0)$ for a double pendulum with parallel axis when $\beta(0) = 0$ .	59
2.14	RMS values of the angular velocity $\dot{\alpha}_{RMS}$ for a damping coefficient $c = 0.01$ and different initial conditions $\alpha(0)$ for a double pendulum with parallel axis when $\beta(0) = 0$ .	59

## LIST OF FIGURES

---

2.15 Time response of the angular position $\alpha$ for a simple pendulum with non-parallel axis with different damping coefficients (Blue curve $c = 0.01$ , Red curve $c = 0.05$ , Grey curve $c = 0.2$ and Green curve $c = 0.5$ ). . . . .	60
2.16 Time response of the angular velocity $\dot{\alpha}$ for a simple pendulum with non-parallel axis with different damping coefficients (Blue curve $c = 0.01$ , Red curve $c = 0.05$ , Grey curve $c = 0.2$ and Green curve $c = 0.5$ ). . . . .	61
2.17 Time response of the angular position and velocity for a simple pendulum with non-parallel axis with different damping coefficients (Blue curve $c = 0.01$ , Red curve $c = 0.05$ , Grey curve $c = 0.2$ and Green curve $c = 0.5$ ). . . . .	61
2.18 Trajectory of the point mass $M$ when $\alpha = 0$ and $\beta(0) = -\frac{\pi}{2}$ for a simple pendulum with non-parallel axes. . . . .	62
2.19 RMS values of the angular velocity $\dot{\beta}_{RMS}$ for a damping coefficient $c = 0.01$ and different initial conditions $\beta(0)$ for a simple pendulum with non-parallel axis when $\alpha = 0$ . . . . .	63
2.20 RMS values of the angular velocity $\dot{\beta}_{RMS}$ for a damping coefficient $c = 0.01$ and different initial conditions $\alpha$ for a simple pendulum with non-parallel axis when $\beta(0) = \pi/2$ . . . . .	63
2.21 3D view of the RMS values of the angular velocity $\dot{\beta}_{RMS}$ for a damping coefficient $c = 0.01$ and different initial conditions $\beta(0)$ and $\alpha$ for a simple pendulum with non-parallel axis. . . . .	64
2.22 Time response of the angular position $\alpha$ for Rott's pendulum with parallel axis with different damping coefficients (Blue curve $c_1 = 0.01$ , Red curve $c_1 = 0.05$ , Grey curve $c_1 = 0.2$ and Green curve $c_1 = 0.5$ ), $c_2 = 0.0001$ . .	65
2.23 Time response of the angular velocity $\dot{\alpha}$ for Rott's pendulum with parallel axis with different damping coefficients (Blue curve $c_1 = 0.01$ , Red curve $c_1 = 0.05$ , Grey curve $c_1 = 0.2$ and Green curve $c_1 = 0.5$ ), $c_2 = 0.0001$ . .	65
2.24 Trajectory of the point mass $M$ when $\alpha(0) = -\frac{\pi}{2}$ and $\beta(0) = 0$ for a Rott's pendulum. . . . .	66
2.25 RMS values of the angular velocity $\dot{\alpha}_{RMS}$ for a damping coefficient $c_1 = 0.01$ and different initial conditions $\alpha(0)$ for a Rott's pendulum with parallel axis when $\beta(0) = 0$ . . . . .	66
2.26 3D view of the RMS values of the angular velocity $\dot{\alpha}_{RMS}$ for a damping coefficient $c_1 = 0.01$ and different initial conditions $\alpha(0)$ and $\beta(0)$ for a Rott's pendulum with parallel axis. . . . .	67

---

## LIST OF FIGURES

---

2.27 RMS values of the angular velocity $\dot{\alpha}_{RMS}$ for a damping coefficient $c_1 = 0.01$ and different initial conditions $\beta(0)$ for a Rott's pendulum with parallel axis when $\alpha(0) = \pi$ . . . . .	67
3.1 Coupled Motors . . . . .	73
3.2 Modeling of the characterization assembly of the generator . . . . .	73
3.3 Experimental setup of the characterization assembly of the generator . . . . .	74
3.4 Variation of $U_o$ , $I_o$ as a function of $R$ for different rotation speeds . . . . .	76
3.5 Variation of $P$ as a function of $R$ for different rotation speeds . . . . .	77
3.6 Variation of $U_o$ and $I_o$ as a function of $\omega_m$ at $R_{opt} = 59\Omega$ . . . . .	78
3.7 Variation of $P$ and $T_m$ as a function of $\omega_m$ at $R_{opt} = 59\Omega$ . . . . .	78
3.8 Setup of the studied pendulums . . . . .	79
3.9 Setup of the SP . . . . .	80
3.10 Setup of the DP . . . . .	81
3.11 Setup of the RP . . . . .	82
3.12 Measuring the Resonance Frequency of Rod 1 . . . . .	83
3.13 Measuring the Resonance Frequency of Rod 2 . . . . .	83
3.14 Rotating disk of Test Bench . . . . .	84
3.15 Layout of the Test Bench . . . . .	85
3.16 Test Bench Realized and DAS . . . . .	85
3.17 Details of the control system of the rotating disk . . . . .	86
3.18 Generated voltage from simple pendulum for $\omega=69.5\text{rpm}$ (SV) . . . . .	88
3.19 Generated voltage from simple pendulum for $\omega=105.5\text{rpm}$ (SR) . . . . .	89
3.20 Generated voltage from double pendulum for $\omega=54\text{rpm}$ (SV) . . . . .	90
3.21 Generated voltage from double pendulum for $\omega=89.5\text{rpm}$ (AP) . . . . .	91
3.22 Generated voltage from double pendulum for $\omega=96\text{rpm}$ (SR) . . . . .	91
3.23 Generated voltage from Rott's pendulum for $\omega=25\text{rpm}$ (SV) . . . . .	93
3.24 Generated voltage from Rott's pendulum for $\omega=85\text{rpm}$ (AP) . . . . .	93
3.25 Generated voltage from Rott's pendulum for $\omega=90\text{rpm}$ (SR) . . . . .	94
3.26 Variation of $\Delta V_{out}$ for different rotation speeds of the disk . . . . .	95
3.27 Applied input function to actuate the rotating disk. . . . .	96
3.28 Generated voltage from double pendulum for variable speed for initial position $\theta=\pi$ . . . . .	98
3.29 Generated voltage from Rott's pendulum for variable speed for initial position $\theta=\pi$ . . . . .	99

---

## LIST OF FIGURES

---

3.30 RMS values of $\Delta V_{out}$ for each initial position for double and Rott's pendulum designs. . . . .	100
4.1 Rott's pendulum into a rotating wheel. . . . .	104
4.2 Wheel rotation speed effect on the solutions $a_1$ and $a_2$ of pendulums $P_1$ and $P_2$ , for $\sigma_1 = 0$ . . . . .	117
4.3 Wheel rotation speed effect on the solutions $a_1$ and $a_2$ of pendulums $P_1$ and $P_2$ , for $\sigma_1 = -0.1$ . . . . .	118
4.4 Wheel rotation speed effect on the solutions $a_1$ and $a_2$ of pendulums $P_1$ and $P_2$ , for $\sigma_1 = -1$ and $\sigma_2 = 0$ . . . . .	118
4.5 Wheel rotation speed effect on the solutions $a_1$ and $a_2$ of pendulums $P_1$ and $P_2$ , for $\sigma_1 = 1$ and $\sigma_2 = 0$ . . . . .	119
4.6 Wheel rotation speed effect on the solutions $a_1$ and $a_2$ of pendulums $P_1$ and $P_2$ , for $\sigma_1 = 1$ and $\sigma_2 = 2$ . . . . .	120
4.7 Influence of the detuning parameter $\sigma_2$ on the solutions $a_1$ and $a_2$ of pendulums $P_1$ and $P_2$ , for $\sigma_1 = -1$ and $\dot{\theta} = 55$ rad/s. . . . .	121
4.8 Influence of the detuning parameter $\sigma_1$ on the solutions $a_1$ and $a_2$ of pendulums $P_1$ and $P_2$ , for $\sigma_2 = 0$ and $\dot{\theta} = 55$ rad/s. . . . .	121
4.9 Influence of the detuning parameter $\sigma_2$ on the solutions $a_1$ and $a_2$ of pendulums $P_1$ and $P_2$ , for $\sigma_1 = 0.1$ and $\dot{\theta} = 55$ rad/s. . . . .	122
4.10 Influence of the detuning parameter $\sigma_2$ on the solutions $a_1$ and $a_2$ of pendulums $P_1$ and $P_2$ , for $\sigma_1 = 1$ and $\dot{\theta} = 55$ rad/s. . . . .	123
4.11 Influence of the detuning parameter $\sigma_1$ on the solutions $a_1$ and $a_2$ of pendulums $P_1$ and $P_2$ , for $\sigma_2 = 1$ and $\dot{\theta} = 55$ rad/s. . . . .	123
4.12 Influence of the detuning parameter $\sigma_1$ on the solutions $a_1$ and $a_2$ of pendulums $P_1$ and $P_2$ , for $\sigma_2 = -3$ and $\dot{\theta} = 55$ rad/s. . . . .	124

## LIST OF FIGURES

---

## LIST OF TABLES

1.1 Power density generation for available energy technologies [17]. . . . .	24
2.1 Specifications of the pendulum EH . . . . .	53
2.2 RMS values of the angular velocity for different damping coefficients and $\alpha(0) = 0$ . . . . .	54
2.3 RMS values of the angular velocity for different damping coefficients, $c_2 = 0.0001$ and $\alpha(0) = -\frac{\pi}{2}$ . . . . .	58
2.4 RMS values of the angular velocity for different damping coefficients, $\alpha = 0$	62
2.5 RMS maximum achievable values of the transducer's angular speed for the different proposed designs. . . . .	68
3.1 Characteristics of 16N78 Athlonix DC motor as given by Portescap [103].	72
3.2 Simple pendulum measured resonance frequencies . . . . .	81
3.3 Measured second rod double pendulum natural frequency . . . . .	82
3.4 Rott's pendulum measured resonance frequencies with $R_{opt}$ . . . . .	83
3.5 Generated voltage from simple pendulum for different rotation speeds .	88
3.6 Generated voltage from double pendulum for different rotation speeds .	90
3.7 Generated voltage from Rott's pendulum for different rotation speeds .	92
3.8 Generated voltage from double pendulum for variable speed for different initial positions . . . . .	97
3.9 Generated voltage from Rott's pendulum for variable speed for different initial positions . . . . .	98
4.1 Geometrical and inertial parameters of the Rott's pendulum . . . . .	116





# SPIM

■ École doctorale SPIM 1 rue Claude Goudimel F - 25030 Besançon cedex

■ tél. +33 (0)3 81 66 66 02 ■ [ed-spim@univ-fcomte.fr](mailto:ed-spim@univ-fcomte.fr) ■ [www.ed-spim.univ-fcomte.fr](http://www.ed-spim.univ-fcomte.fr)

